Role of Chirality in Electron Spin Filtering, Water Splitting, and Electron Transfer

by

Jimeng Wei

Bachelor of Science, Trinity College, 2014

Submitted to the Graduate Faculty of the

Dietrich School of Arts and Sciences in partial fulfillment

of the requirements for the degree of

Doctor of Philosophy

University of Pittsburgh

2023

UNIVERSITY OF PITTSBURGH

DIETRICH SCHOOL OF ARTS AND SCIENCES

This dissertation was presented

by

Jimeng Wei

It was defended on

May 25, 2023

and approved by

Jung-Kun Lee, PhD, Swanson School of Engineering

Haitao Liu, PhD, Department of Chemistry

Adrian Michael, PhD, Department of Chemistry

Dissertation Director: David Waldeck, PhD, Department of Chemistry

Role of Chirality in Electron Spin Filtering, Water Splitting and Electron Transfer

Jimeng Wei, B.S., Ph.D

University of Pittsburgh, 2023

The focus of my dissertation is to study the chiral induced spin selectivity (CISS) effect and how the CISS effect can be used to explain some biological electron transfer process and if chiral materials can act as spin filters to enhance water splitting efficiency. The cytochrome *c* – oligopeptide assembly we have built demonstrated that the chiral oligopeptide molecules are effective spin filters, and the electron transfer rate constant depends heavily on the whether the chirality of the cytochrome *c* and the oligopeptide matcher each other. We have also successfully electrodeposited chiral metal oxide films, where the chirality and spin filtering capabilities of these metal oxide films were confirmed using circular dichroism spectroscopy and photoemission spectroscopy. Moreover, we discovered that these chiral metal oxide films can be used to lower the overpotential of the water splitting reaction. However, a different approach to make chiral metal oxide films by using ALD does not show concrete evidence that the metal oxide films are chiral, and it requires further research and improvement.

Table of Contents

Acknowledgement ..... **xviii**

1.0 Introduction **1**

1.1 Chiral Induced Spin Selectivity Effect **1**

1.2 Electron transfer theory of peptide molecules **3**

1.3 Homochiral charge transport using immobilized cytochrome c on peptide self assembled monolayer **7**

1.4 Inorganic chiral metal oxide films **8**

1.5 Reference **11**

2.0 Examining the Effects of Homochirality for Electron Transfer in Protein Assemblies **13**

2.1 Introduction **13**

2.2 Results and Discussion **16**

2.3 Conclusion **26**

2.4 Experimental **27**

2.4.1 Hall Effect Device Fabrication and Measurement **27**

2.4.2 Electrode Fabrication, SAM Preparation, and Cytochrome c Assembly **28**

2.4.3 SAM and Tripeptide Characterization **28**

2.4.4 Cyclic Voltammetry **29**

2.5 Associated Content **30**

2.6 Reference **32**

3.0 Controlling Chemical Selectivity in Electrocatalysis with Chiral CuO Coated Electrodes 36

3.1 Introduction 36

3.2 Experimental 39

3.2.1 Growth and Characterization of CuO films 39

3.2.2 Photoemission Measurements 40

3.2.3 Electrochemical Measurements 41

3.3 Results and Discussion 42

3.3.1 Characterization of CuO films 42

3.3.2 Photoemission Studies 44

3.3.3 Electrolysis Studies 44

3.3.4 Hydrogen evolution and Peroxide suppression 46

3.4 Acknowledgements 52

3.5 Reference 54

4.0 Spin-polarized Photoemission from Chiral CuO Catalyst Thin Films 61

4.1 Introduction 61

4.2 Results and Discussion 63

4.2.1 Film Deposition and Characterization 63

4.2.2 Copper Oxidation State 64

4.2.3 Film Chirality 65

4.2.4 Electronic Structure 67

4.2.5 Spin Polarization Measurements 68

4.2.6 Origin of the Photoelectrons 72

4.2.6.1 Intrinsic Spin Polarization 73

4.2.7 Origin of the Photoelectron Spin Polarization 78

4.2.8 Magnetics 80

4.3 Summary and Outlook 83

4.4 Methods 84

4.4.1 Film Deposition 84

4.4.2 XPS Measurements 85

4.4.3 He(I) UPS Measurements 85

4.4.4 213 nm UPS Measurements 85

4.4.5 Absorption and CD Measurements 86

4.4.6 Spin Polarization Measurements 86

4.4.7 VSM Measurements 88

4.5 Associated Content 88

4.5.1 Supporting Information 88

4.5.2 Acknowledgements 89

4.6 Reference 90

5.0 Atomic layer deposition of chiral metal oxide 96

5.1 Introduction 96

5.2 Experimental 98

5.3 Results and Discussion 100

5.4 Conclusion 108

5.5 Reference 109

6.0 Conclusion 110

7.0 Appendix 111

7.1 Spectroscopic ellipsometry 111

7.2 Reference 114

List of Tables

Table 2-1. <k^0> for different SAMs, with 30 mM KCl. 26

List of Figures

Figure 1-1. Illustration of chiral induced spin selectivity effect. (a) A schematic description of the electron transmission through a chiral potential of pitch p, and B is the effective magnetic field generated by the movement of electrons. (b) A schematic description of the charge and spin polarization in chiral molecules, when the molecules are exposed to an electric field acting along their axes (black arrows). δ (+) and δ(−) denotes the transient spin polarization at the electric poles. Reprinted from ref 1.... 2

Figure 1-2. Electron transfer mechanisms through peptides by superexchange (bottom pathway) and hopping (top pathway). Reprinted from ref 5. 4

Figure 1-3. (A) Chemical structures and schematic illustration of the helical peptides. The helices are expressed in a ribbon representation and the other atoms are shown in a ball-and-stick format: C gray; N blue; O red; S yellow; Fe purple. (B) Plot of the inverse of the square root of $ket0$ versus the ellipsometry thickness. The dashed line is the linear fit and the solid line shows the result of calculations upon taking the tunneling and hopping mechanisms into consideration. Reprinted from ref 10..... 5

Figure 1-4. (A-B) AFM height and phase images of 1wt%AAKLVFF assembled in MeOH, respectively (z scale 234 nm and 65°, respectively). (C-D) AFM height and phase images of 1wt%AAKLVFF assembled in TDW, respectively (z scale 154 nm and 11°, respectively). (E) I-V curves and conductance values (inset) of 1wt%AAKLVFF assembled in either MeOH or TDW. Samples were prepared by drop-drying 5 µL droplets of the solution. Current measurements were obtained under pressure of 10-3 mbar. Reprinted from ref 11..... 6

Figure 2-1. Overview of the Hall effect measurements. (A) Schematic view of the experimental set-up for the Hall measurements. (B) Representative time-profile of a measurement in which the square wave feature (black) shows the applied gate voltage versus time and the red waveforms show the corresponding Hall voltage response. (C) Plot of the measured Hall response for the initial spike after application of the gate voltage for LLL- (blue), DDD- (red), and LDL-tripeptide (green) SAMs. The error bars represent one standard deviation of the error over all measurements and devices at the applied gate voltage. 17

Figure 2-2. Panel A shows a diagram for the electrochemical set-up and the SAM-coated working electrode. The tripeptide molecules were self-assembled on top of a Ni/Au film electrode, and the Cyt *c* was electrostatically immobilized on top of the SAM. The Cyt *c* structure shown is from the Protein Data Bank, code 3o20. (B) Cyclic voltammogram of an LLL-tripeptide SAM before (black) and after (blue) immobilization of Cyt *c*. (C) Plot of the peak current of Cyt *c* immobilized on an LLL-tripeptide SAM vs scan rate. The linear best fit line has an R^2 value of 0.9995. (D) Plot of the Cyt *c* anodic (blue, solid squares) and cathodic (blue, open squares) peak potential shift as a function of the scan rate for an LLL-tripeptide Cyt *c* assembly. The error bars quantify uncertainty in the fitted voltammetric peak positions; see Experimental details. The solid curves are three different theoretical Marcus fits to the experimental data with reorganization energies of 0.1 eV (orange), 0.3 eV (black), and 0.6 eV (grey); The R^2 values for the different reorganization energies are 0.90, 0.94, and 0.92, respectively. 19

Figure 2-3. (A) The asymmetry in electron transfer rate constants is plotted versus the solution ionic strength for Cyt *c* immobilized on an LLL-tripeptide SAM (blue), DDD-tripeptide SAM (red), LDL-tripeptide (green), and achiral 11-mercaptoundecanoic acid SAM (purple) at four different ionic strengths. (B) Asymmetry in electron transfer rates for Cyt *c* immobilized on an LLL-tripeptide SAM (blue, open symbol), DDD-tripeptide SAM (red, open symbol), LDL-tripeptide (green, open symbol), and achiral 11-MUA SAM (purple, open symbol) at 4 different ionic strengths. 22

Figure 2-4. Plot of the magnitude of rate constant asymmetry, $|A|$, for LLL-tripeptide (blue) and DDD-tripeptide assemblies as a function of the average rate constant, $\langle k^0 \rangle$, for different electrode preparations and solution conditions; 10 mM KCl (circles), 20mM KCl (diamonds), 30 mM KCl (triangles) and 40mM KCl (squares). The horizontal blue and red box plots on top of the figure represent statistics of $\langle k^0 \rangle$ values of LLL-tripeptide and DDD-tripeptide assemblies, respectively, and the vertical blue and red box plots on the right of the figure represent statistics of |A| values of LLL-tripeptide and DDD-tripeptide assemblies, respectively. For each box plot, the central line represents the median of the data, the box represents the interquartile range (IQR), the whiskers extend to the extreme observed data points falling within 1.5 IQRs of the median, and the notches represent an estimate of the 95% confidence interval that can be used to characterize the statistical significance of differences among the populations..... 24

Figure 3-1. The plot shows the spin polarization P of photoelectrons from the Au/CuO films as a function of the CuO film thickness d and its chirality. The red diamonds are the

L-CuO formed from L-tartrate:Cu^{2+} solutions and the blue diamonds are the D-CuO formed from the D-tartrate:Cu^{2+} solutions. 43

Figure 3-2. Panel A shows a UV-visible spectrum of a 50 nm thick L-CuO film with the UV-visible spectrum of a 20 nm Au substrate subtracted. Panel B shows circular dichroism (CD) spectra of 50 nm L-CuO film (red), D-CuO films (blue), and a meso-CuO film (purple). Note the approximate mirror symmetry of the L-CuO and D-CuO films, and the zero CD for the achiral meso-CuO..... 43

Figure 3-3. (A) Linear sweep voltammograms for 50 nm thick L-CuO (red) film electrodes, 50 nm thick D-CuO (blue) film electrodes, and bare Au (black) electrodes. The inset provides a zoomed-in view of the data and reveals a current prepeak which has been associated with a small percentage of highly active catalytic sites (see text). The potential is reported versus NHE, and the current density is given in mA/cm^2. (B) 500 nm thick films for which the onset potential shifts to larger values. The glycine-CuO films (shown in light green) are achiral and display less electrocatalytic activity than the chiral CuO films..... 45

Figure 3-4. (A) Linear sweep voltammetry curves for electrochemically deposited chiral CuO (induced by L-tartaric acid, red line) and achiral CuO (induced by meso-tartaric acid, black line) electrodes in a pH 9 aqueous buffer solution in dark conditions. (B) Rate of hydrogen production measured using electrochemically deposited CuO at constant potential 1.4 V vs NHE (red for chiral CuO and black for achiral CuO). (C) H_2O_2 detection. UV−vis absorption spectra (red line for chiral CuO and black line for achiral CuO) of the used 0.1 M Na_2SO_4 electrolyte after the titration with o-tolidine.

The electrochemical measurement is done by keeping the anode at a constant potential of 1.7 V versus NHE for 40 min in the dark. 47

Figure 3-5. Schematic of the electrochemical setup for the case where electrochemically deposited CuO is used as both cathode and anode. The results with the cell containing chiral CuO are presented in red, while those with achiral CuO are in black. The dotted lines represent the measurements carried out in the dark, and the solid line represents measurements carried out in the light. The current density versus applied potential is shown in panel B for the case where the bias is applied to the cathode (wiring diagram in panel A) and in panel D for the case where the bias is applied to the anode (wiring diagram in panel C). Electrochemical measurements were performed using 0.1 M Na_2SO_4 solution with pH 6.5. The scan is performed up to 1.5 V vs Ag/AgCl (3 M NaCl) with a scan rate of 20 mV/s in the dark. E(NHE) = E(vs Ag/AgCl) + E°(Ag/AgCl), where E°(Ag/AgCl, 3 M NaCl) = 0.195 V. 49

Figure 3-6. Energy diagram illustrating the possible reaction products from the combination of hydroxyl groups on the CuO surface. The spin restriction on the recombination leads to selectivity against H_2O_2 formation if the OH radical spins are aligned. 51

Figure 4-1. An XPS spectrum of the Cu2p peak region, acquired on a 40 nm oxide thin film, is shown. At binding energies of 940 to 945 eV and at 963 eV two satellite peaks to the Cu 2p3/2 and 2p1/2 peaks, respectively, appear which are indicative of CuO and are absent for Cu2O.[24] 65

Figure 4-2. CD spectra measured on 40 nm CuO thin films of either handedness (a) and the CD magnitude at different wavelengths as a function of the film thickness (b). 66

Figure 4-3. Energy scheme of the Au/CuO samples, determined from He I photoelectron spectra of a 200 nm CuO sample, and a bare gold substrate. Note that XCuO is the electron affinity of CuO and Eion is the position of the valence band edge relative to the Fermi level EF. A very slight shift ΔΦ of the vacuum level is measured. The other energies are specified in the text. 68

Figure 4-4. Simplified scheme of the Mott scattering setup. (b) Spin polarization measured upon front side excitation with linearly polarized light for L- and D-CuO films.9 (c) Further technically identical measurements (full symbols) and measurements with the laser impinging on the back side of the partially UV-transparent samples (empty symbols). Note that the plots in (b) and (c) have different scales for their horizontal axes. The red-shaded areas indicate the standard deviation σ / √ n, normalized to the number of individual measurements, n. In figure 5 (c), only one data point is available for 5 nm thin films; here, the uncertainty of the single measurement is indicated. Figure 5 (b) reprinted with permission from ref. 9. Copyright 2019 American Chemical Society. 71

Figure 4-5. Differential spin polarization measured upon excitation with cw and ccw circularly polarized light impinging on either the front (a) or back (b) side of the samples. The standard deviation σ / √ n, normalized to the number of individual measurements, n, is indicated by the red-shaded area. The light blue lines are a guide to the eye; overlapping points are offset for clarity. The same sample areas were studied in (a) and (b). 74

Figure 4-6. UV photoelectron spectra, acquired with the laser irradiating the samples at λ = 213 nm either from the front (labeled "F") or back (labeled "B") side. Shown are (a)

reference spectra from a from a 200 nm thick CuO layer and the bare gold substrate and spectra from samples with (b) 10 nm and (c) 40 nm thick CuO films. 76

Figure 4-7. Magnetization curves at T = 300 K of a sample with an achiral 200 nm thick CuO film (a) and a 200 nm thick L-CuO film before (b) and after (c) subtraction of the diamagnetic substrate signal. (d) Hysteresis at T = 4.3 K (blue) and 300 K (red) on an enlarged scale. 82

Figure 5-1. Representation of an ALD film growth process: Precursor A is pulsed into the reaction chamber and binds to the substrate, and then Precursor B is introduced to react with precursor A in order to form one layer of metal oxide. This cycle can be repeated many times to reach the desired thickness. Reprinted with permission from ref 4. 97

Figure 5-2. SHG intensity versus quarter wave plate rotation angle. Top: D and L-cysteine on gold; bottom: D- and L-cysteine on gold covered with TiO_2. Reprinted from ref 1. 101

Figure 5-3. Quartz microbalance (QCM) adsorption/desorption profile of L- and D-valine onto TiO_2 L- and D-cysteine nanofilms. Reprinted from ref 1. 102

Figure 5-4. (A) Ellipsometry of a TiO_2 film deposited using ALD on an Au substrate with L-Cys SAM. (B) Cyclic voltammogram of 0.1M K_2SO_4 solution with a TiO_2 film as the working electrode. The reference electrode is an Ag/AgCl electrode immersed in 1M KCl, and the counter electrode is a Pt mesh. 103

Figure 5-5. Cyclic voltammograms of L-tartrate (red) and D-tartrate (blue) in 0.1M Na_2SO_4 on 1.5 nm thick TiO_2 electrodes. (A) Working electrode consists of TiO_2 deposited on

L-Cys SAM using ALD. (B) Working electrode consists of TiO_2 deposited on D-Cys SAM using ALD. 104

Figure 5-6. CV of L-tartrate (red) and D-tartrate (blue) in 0.1M NaOH on 1.5nm thick TiO_2 electrodes. (A) Working electrode consists of TiO_2 deposited on L-Cys SAM using ALD. (B) Working electrode consists of TiO_2 deposited on D-Cys SAM using ALD. 105

Figure 5-7. CV of 400µM R-Fc (red) and S-Fc (blue) in 10mM Na_2SO_4 on 1.5nm thick TiO_2 electrodes. (A) 106

Figure 5-8. CV of L-tartrate (red) and D-tartrate (blue) in 0.1M NaOH on 100nm thick CuO electrodes. (A) Working electrode consists of CuO deposited using L-tartaric acid. (B) Working electrode consists of CuO deposited using D-tartaric acid. 107

Figure 5-9. (A) CV of 400µM R-Fc (red) and S-Fc (blue) in 10mM Na_2SO_4 on a bare Au film electrode. (B) Circular dichroism spectra of L-Cys TiO_2 film (red) and D-Cys TiO_2 (blue) on a 3nm Ti and 10nm Au film on fused silica substrates. Both the L- and D-TiO_2 are 3nm thick..... 108

Figure 7-1. The ellipsometry measurement is shown. Here, light polarized at 45◦ from the plane of incidence is shown scattering from a sample. The angle θ that the light makes with surface is shown in the main figure. Adapted from ref 1. 111

Figure 7-2. Illustration of reflection and transmission at a single interface. Adapted from ref 2..... 112

Acknowledgement

I would like to express my most sincere gratitude to Prof. David Waldeck, who has both given me a chance to study in his research group as well as all the guidance and patience I have received from him. Pursuing a PhD degree is never meant to be easy, and I certainly ran into many obstacles along the way, but I'm glad that Prof. Waldeck was always there whenever I needed feedback and alternatives.

I would also like to thank my parents for their continuous support for me. Without their support and understanding, it will not be possible for me to come to the United States in order to pursue my undergraduate and graduate degrees. In addition, I would like to thank Mr. John Auses, who is the ex-administrative officer of the department of chemistry. John has helped me tremendously during my early years as a graduate student, and I could not have achieved so much without his support.

I have had the pleasure to work with three excellent postdoctoral associates in our research group: Dr. Emil Wierzbinski, Dr. Brian Bloom and Dr. Wiley Dunlap-Shohl. All of them have given me a lot of mentoring to guide me through my research, and I have learned so much with them. Finally, I would like to thank all the current and previous Waldeck group members that I had a chance to work with. All of you have been so helpful and supportive , which makes the Waldeck lab a very happy and productive place for everyone.

1.0 Introduction

1.1 Chiral Induced Spin Selectivity Effect

Electrons have two possible spin states, and the two spin states are degenerate when no external magnetic field is present. When an external magnetic field is applied, this spin state degeneracy will be broken, and one spin state will be higher in energy than the other state. Because of the similarity between the two possible spin states of electrons and the binary data system of modern computer system, the spin states of electron can be used to transfer and store data; and such applications are called spintronics. Spintronic devices are not yet as fully developed as traditional electronic devices, the recent development of giant magnetoresistance (GMR) and its application in mechanical hard drives has opened the possibility for spintronics to serve as a viable alternative to electronics. However, the current spintronic devices do have many limitations, and one of these limitations is the reliance on an external magnetic field to break the spin state degeneracy. Specifically, it is extremely difficult to apply a magnetic field in many small devices and environments, thus it is important to find a different way to filter the electrons based on their spin states.

The chiral induced spin selectivity (CISS) effect is a promising alternative to using external magnetic fields to filter electrons based on their spin states. In 1999, Naaman and Waldeck first described the chiral induced spin selectivity (CISS) effect, and it relates to how chiral molecules and materials can act as electron spin filters. When electrons pass through a chiral material (Figure 1A[1]), the curvature of potential energy from the chiral electrostatic field acts on the electron aligned with its spin to the electrons' direction of momentum. The electrons experience a chiral

electrostatic potential, and their movement under this potential generates an effective magnetic field (B). This coupling between the spin state and the motion of the electron is called the spin-orbital coupling (SOC). Moreover, the chiral field of materials with opposite chirality are mirror images of each other, and electrons with different spin states have opposite magnetic dipoles, and the energies of the two spin states split so that one spin orients parallel to the momentum and the other orients antiparallel to the momentum.

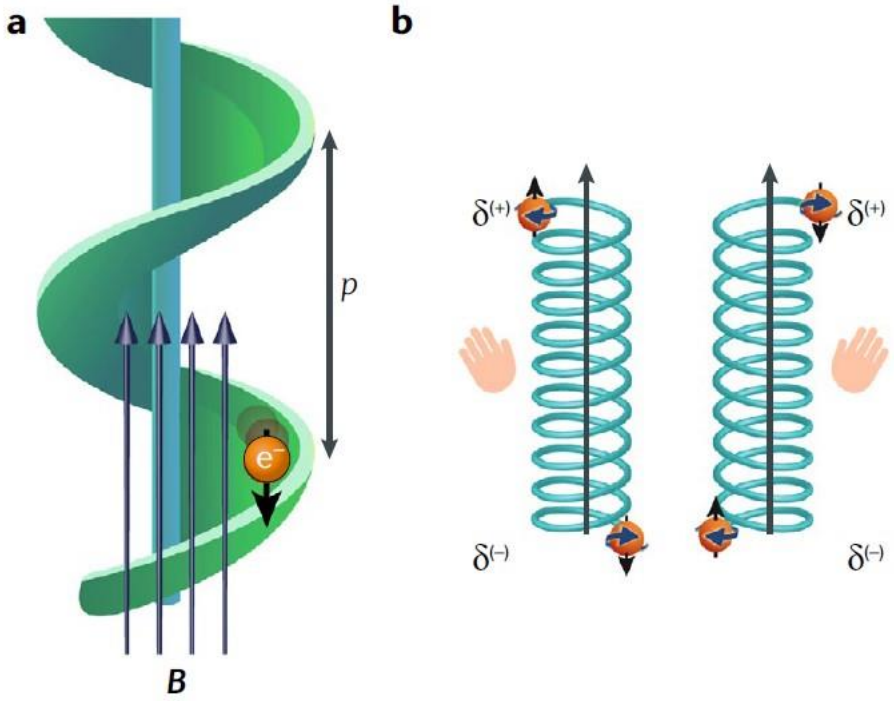

Figure 1-1. Illustration of chiral induced spin selectivity effect. (a) A schematic description of the electron transmission through a chiral potential of pitch p, and B is the effective magnetic field generated by the movement of electrons. (b) A schematic description of the charge and spin polarization in chiral molecules, when the molecules are exposed to an electric field acting along their axes (black arrows). δ (+) and δ(−) denotes the transient spin polarization at the electric poles. Reprinted from ref 1.

The electron transport through chiral materials is often presumed to involve tunneling, and when SOC breaks the degeneracy of the spin states, the tunneling barrier for one spin state will be higher than the other in a chiral material. This leads to a preference for the transmission of one spin state by a chiral material and the electrons with the unfavored spin state will not be able to pass due to the higher tunneling barrier; if a material with opposite chirality is used, the electron

spin preference reverses as well (See Figure 1). The CISS effect has been directly observed in photoemission studies. Namely, when the substrate is excited with a laser source, the photoelectrons generated that pass through chiral materials will become spin polarized[2-4].

The CISS effect is particularly useful because it is not limited by the same constraints as external magnetic fields. Specifically, it is extremely difficult to apply a magnetic field in many small devices and environments. With the CISS effect, it is possible to filter electrons based on their spin states without the need for external magnetic fields, making it a viable alternative for spintronics applications. It is worth mentioning that the CISS effect is still in the early stages of research, and much work is still needed to fully understand and utilize this effect in spintronic devices. Nonetheless, the discovery of the CISS effect has opened the door to new possibilities in the field of spintronics and may lead to the development of more efficient and versatile spintronic devices.

The CISS effect may help to explain why some electron transfer reactions are spin dependent, and this could help to explain the biological homochirality in nature. Furthermore, these non-magnetic spin filters may also suggest new designs for spintronic devices, which use the spin states of electrons to read and store information.

1.2 Electron transfer theory of peptide molecules

One of the major functions of peptides in biological systems is to facilitate electron transfer (ET), thus the ET mechanism of peptides has been studied in great detail. Typically, the ET through

peptides is believed to occur by two potential mechanisms; superexchange and hopping. For the shorter peptides, the electrons are transferred by superexchange where the electrons directly tunnel through the molecules. For the longer peptides, the electron transfer occurs by hopping where a multi-step tunneling would take place (see Figure 2[5]).

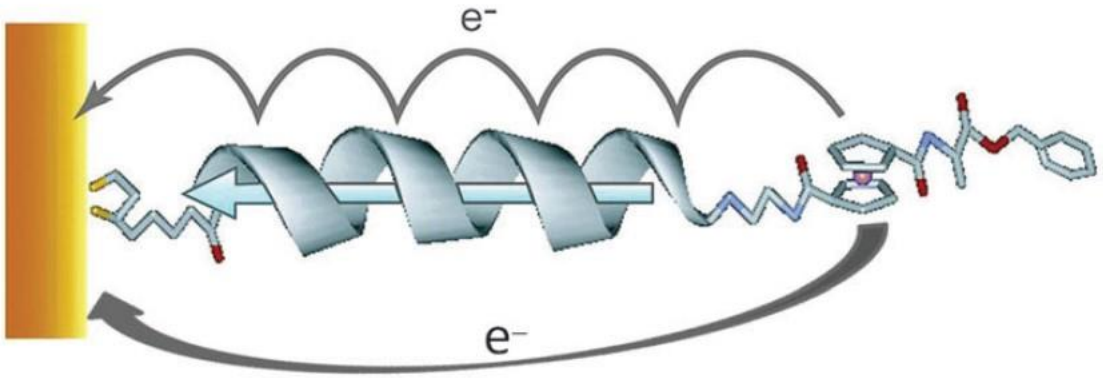

Figure 1-2. Electron transfer mechanisms through peptides by superexchange (bottom pathway) and hopping (top pathway). Reprinted from ref 5.

Several factors can affect the rate of electron transfer, and the length of the molecule is a major factor. Obviously, the electron transfer will become slower as the molecules get longer due to the increasing resistance, but the rate of decay follows different patterns for the two ET mechanisms. For the superexchange mechanism, the ET rate will decrease exponentially with respect to the peptide molecule length, and is often dictated well by the Marcus theory.[6-9] As the peptides get longer, the mechanism will change from superexchange to hopping and this change takes place at roughly 20 Å[8]. Because several steps of tunneling need to take place in the hopping mechanism, the ET rate decays in a more linear fashion, and this can be seen in Figure 3.[10] Arikuma et al. synthesized five different peptides with increasing length (see Figure 3A), and because of the alternating l-alanine (Ala) and a-aminoisobuty-ric acid (Aib) sequence, each of the tunneling barriers should have equal energy levels during the hopping electron transfer. And if the ET does takes place via hopping, the thickness of the SAM should be proportional to the square root of the

rate constant. Figure 3B shows a linear dependence between $(k_{et}^0)^{-0.5}$ and the thickness of the SAM, which supports the hopping mechanism for longer peptides.

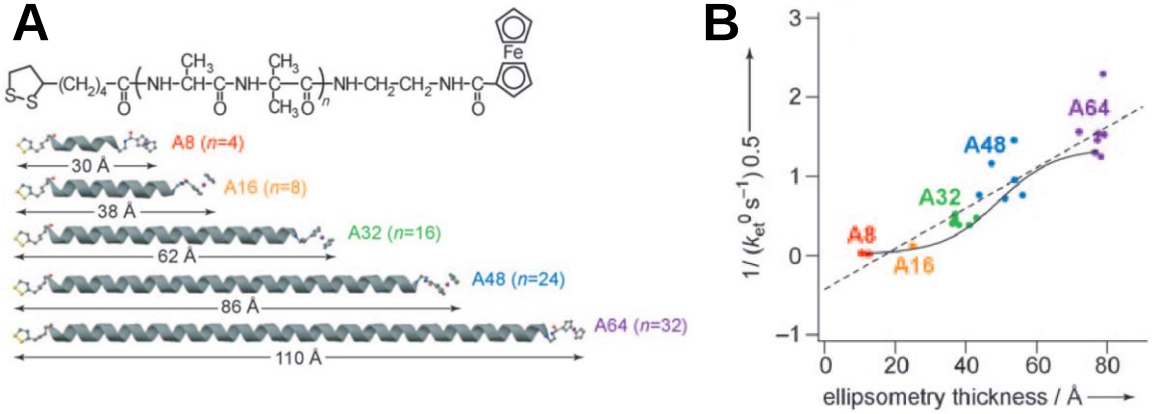

Figure 1-3. (A) Chemical structures and schematic illustration of the helical peptides. The helices are expressed in a ribbon representation and the other atoms are shown in a ball-and-stick format: C gray; N blue; O red; S yellow; Fe purple. (B) Plot of the inverse of the square root of k_{et}^0 versus the ellipsometry thickness. The dashed line is the linear fit and the solid line shows the result of calculations upon taking the tunneling and hopping mechanisms into consideration. Reprinted from ref 10.

In addition to the peptide molecule length, the morphology of the SAM and secondary structure of the peptide will affect the ET rate. The SAM morphology is easily affected by the impurities on the substrate surface, thus it is crucial to thoroughly clean the substrate before the SAM incubation. Moreover, the choice of solvent for dissolving the peptide can also affect the SAM morphology. Work by Amit et al., who prepared SAMs with the peptide AAKLVFF using both methanol and triply distilled water as solvents[11] illustrated this sensitivity. Figure 4A shows the current-voltage curve and conductance measurements of the two peptide SAMs that were prepared with different solvents. It is obvious that the peptide dissolved in methanol resulted in a much higher conductance than using water as the solvent. Given that both samples use the same peptide, it is safe to conclude the difference observed in Figure 4A is caused by the SAM morphology. Figures 4A to D show the AFM and phase images of the peptide SAM prepared using methanol and water respectively. Both Figure 4A and 4B show the peptide dissolved in methanol was able to form a network of elongated nanotubes, while Figure 4C and 4D show that peptide

dissolved in water formed small aggregates throughout the entire surface. Because these aggregates are not interconnected with each other, they would provide fewer pathways for electrons to pass through, hence decreasing the overall conductance.

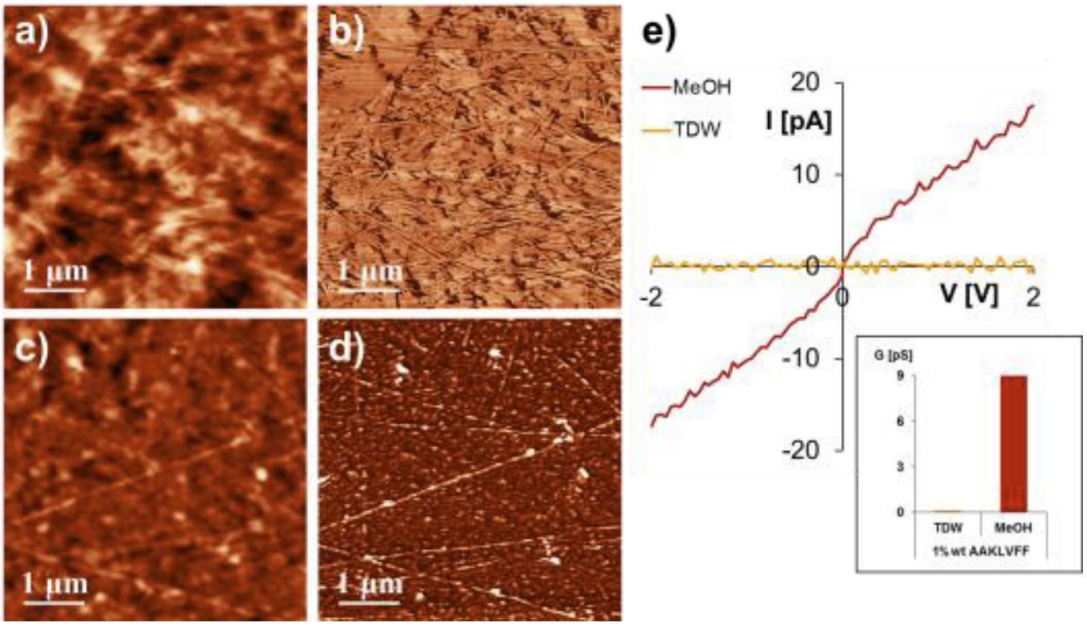

Figure 1-4. (A-B) AFM height and phase images of 1wt%AAKLVFF assembled in MeOH, respectively (z scale 234 nm and 65°, respectively). (C-D) AFM height and phase images of 1wt%AAKLVFF assembled in TDW, respectively (z scale 154 nm and 11°, respectively). (E) I-V curves and conductance values (inset) of 1wt%AAKLVFF assembled in either MeOH or TDW. Samples were prepared by drop-drying 5 µL droplets of the solution. Current measurements were obtained under pressure of 10-3 mbar. Reprinted from ref 11.

The peptide that we focus on in Chapter 2 has the sequence Cys-Ala-Glu, which is a very short peptide. Therefore we predict that the ET mechanism should be the superexchange where a single step of tunneling would take place. We also conducted studies of pure peptide vs peptide with diluent molecules to demonstrate how the change in SAM morphology can affect the ET rate and mechanism.

1.3 Homochiral charge transport using immobilized cytochrome c on peptide self assembled monolayer

Many organic molecules can have two enantiomeric forms, and during organic synthesis, it is common to end up with an equal amount of the two enantiomers as the final product (racemic mixture). However, when we look at biological systems on the earth, most of the organic molecules exist as one pure enantiomer instead of a mixture of two enantiomers. For example, the amino acids in most organisms are left-handed (levo), and almost all nucleic acids and sugars are right-handed (dextro). While countless studies have focused on how biological systems perform enantiospecific organic synthesis, one very important question still remains a mystery: Why do organisms prefer one chirality over the other?

Several hypotheses exist that try to explain the homochirality of biological systems, and the consensus is that some kind of chiral symmetry-breaking agent must be involved[12-14]. It is very possible that the origin of biological homochirality was caused by a combination of different factors, and we propose that the CISS effect is also part of that reason. Previous studies have shown that when spin polarized electrons (number of electrons with one spin state is more than the other spin state) are injected into a chiral material, the electron transfer rate would change depending on the chirality and the initial spin polarization[15, 16]. Furthermore, it has been shown that electrons become spin polarized when passing through chiral organic molecules, and the electrons with the unfavored spin would be scattered away[17]. Thus, if the spin polarized electrons from a chiral molecule A need to be transported through a chiral molecule B and reach molecule C (a typical charge transport pathway in biological systems), whether the chirality of molecule A and B match or mismatch can have a big impact on the electron transfer rate.

In order to mimic such a chiral electron transfer system, we built an electrode assembly with cytochrome c and oligopeptides. The oligopeptides we tested always have cysteine amino acid as the N-terminus, and the thiol group at this site allows for a self assembled monolayer (SAM) to form on an Au substrate by facilitating Au-S bonding. The C-terminal of the oligopeptides are carboxylic acids and they can become negatively charged at the correct pH, the cytochrome *c* (Cyt *c*) molecules can be immobilized on top of the peptide SAM via electrostatic interaction due to the positively charged lysine residue of Cyt *c*. The Cyt *c* has a heme unit that is redox active, and because all the amino acids in Cyt *c* have an L chirality, the electrons that enter or exit the Cyt c will become spin polarized, according to the CISS effect. When the spin polarized electrons pass through the peptide SAM, the rate constant of the ET process could be affected depending on the specific chirality of each amino acid in the peptide sequence. Thus, by comparing the rate constants of oligopeptide that have different chirality, it can enable us to see whether the CISS effect can manifest and affect the electron transfer rate. More details can be found in Chapter 2.

1.4 Inorganic chiral metal oxide films

In the previous sections, several examples of how a chiral material can spin filter the electrons have been described, but all of these examples focused on using organic molecules as the spin filter. While this helps to explain the spin-specific reactions in biological systems, it can become inadequate in applications that require solid state environments or the use of high potentials for prolonged period of time. Hence, it is important to develop chiral inorganic materials and see if they also exhibit the CISS effect.

Metal oxides could serve as a potential choice for applying the CISS effect in solid-state devices, because they have already seen extensive applications in electronics manufacturing due to their stability and semiconductor properties. However, metal oxides are inherently achiral materials, and chiral imprinting is needed to incorporate chirality into the metal oxide. The basic idea of chiral imprinting can be realized by introducing a chiral precursor during the metal oxide deposition process, so that the metal oxide could develop a chiral secondary structure. There are several different types of chiral precursors, and the two methods we have tried so far are chiral organometallic complexes from which electrodeposition proceeds, and a direct metal oxide deposition on top of a chiral self-assembled monolayer.

Electrodeposition is a very common method of making thin metal oxide films, and the process starts with forming a metal complex using an organic molecule, and the aqueous solution of this complex is used as the electrolyte in a galvanic cell. By applying a potential to the cell, the complex will be oxidized and forms a layer of metal oxide on the electrode. In our case, the organic molecule that is coordinating to the metal ions also serves as the chiral precursor[2, 3, 18]. Despite the fact that the exact mechanism is still unclear, it does create a chiral secondary structure and makes the metal oxide chiral. More details regarding the chirality of metal oxide and its application can be found in Chapter 3 and 4.

A second method of chiral imprinting is to begin by growing a layer of a chiral self-assembled monolayer film, and then directly depositing the metal oxide film on top of the monolayer[19, 20]. It is possible that the metal oxide will build its superstructure based on the chirality of the monolayer, thus incorporating the chirality into the metal oxide layer itself. Because of the delicacy of the monolayer, it is not smart to use methods like electrodeposition to grow the metal oxide. Instead, methods like chemical vapor deposition or atomic layer deposition are much less

damaging to the substrate surface; thus they serve as better alternatives for depositing metal oxide films on self-assembled monolayers. In Chapter 5, we focused on using atomic layer deposition to grow chiral metal oxide films.

In summary, our research focused on the study of CISS effect with two approaches. One is to use oligopeptide SAMs to see how chirality affects the biological electron transfer process, and by changing the chirality of the oligopeptides, we begin to explore whether the biological homochirality can be explained by the CISS effect. The other approach is to develop effective methods to deposit chiral metal oxides: Chiral metal oxides can serve as effective spin filters and electrocatalysts, and we would like to test different methods of incorporating chirality into metal oxide films, and how these chiral films can be applied in spintronics device fabrication and water splitting.

1.5 Reference

1.Naaman, R.; Paltiel, Y.; Waldeck, D. H., Chiral molecules and the electron spin. *Nature Reviews Chemistry* **2019,** *3* (4), 250-260.

2.Ghosh, K. B.; Zhang, W.; Tassinari, F.; Mastai, Y.; Lidor-Shalev, O.; Naaman, R.; Möllers, P.; Nürenberg, D.; Zacharias, H.; Wei, J.; Wierzbinski, E.; Waldeck, D. H., Controlling Chemical Selectivity in Electrocatalysis with Chiral CuO-Coated Electrodes. *The Journal of Physical Chemistry C* **2019,** *123* (5), 3024-3031.

3.Möllers, P. V.; Wei, J.; Salamon, S.; Bartsch, M.; Wende, H.; Waldeck, D. H.; Zacharias, H., Spin-Polarized Photoemission from Chiral CuO Catalyst Thin Films. *ACS Nano* **2022,** *16* (8), 12145-12155.

4.Möllers, P. V.; Ulku, S.; Jayarathna, D.; Tassinari, F.; Nürenberg, D.; Naaman, R.; Achim, C.; Zacharias, H., Spin-selective electron transmission through self-assembled monolayers of double-stranded peptide nucleic acid. *Chirality* **2021,** *33* (2), 93-102.

5.Shah, A.; Adhikari, B.; Martic, S.; Munir, A.; Shahzad, S.; Ahmad, K.; Kraatz, H.-B., Electron transfer in peptides. *Chem. Soc. Rev.* **2015,** *44* (4), 1015-1027.

6.Polo, F.; Antonello, S.; Formaggio, F.; Toniolo, C.; Maran, F., Evidence Against the Hopping Mechanism as an Important Electron Transfer Pathway for Conformationally Constrained Oligopeptides. *Journal of the American Chemical Society* **2005,** *127* (2), 492-493.

7.Inai, Y.; Sisido, M.; Imanishi, Y., Photoinduced electron transfer in a single .alpha.-helical polypeptide chain: evidence of a through-space mechanism. *The Journal of Physical Chemistry* **1991,** *95* (9), 3847-3851.

8.Xiao; Xu; Tao, Conductance Titration of Single-Peptide Molecules. *Journal of the American Chemical Society* **2004,** *126* (17), 5370-5371.

9.Sek, S.; Misicka, A.; Swiatek, K.; Maicka, E., Conductance of α-Helical Peptides Trapped within Molecular Junctions. *The Journal of Physical Chemistry B* **2006,** *110* (39), 19671-19677.

10.Arikuma, Y.; Nakayama, H.; Morita, T.; Kimura, S., Electron Hopping over 100 Å Along an α Helix. *Angewandte Chemie International Edition* **2010,** *49* (10), 1800-1804.

11.Amit, M.; Cheng, G.; Hamley, I. W.; Ashkenasy, N., Conductance of amyloid β based peptide filaments: structure–function relations. *Soft Matter* **2012,** *8* (33), 8690-8696.

12.Ozturk, S. F.; Sasselov, D. D., On the origins of life's homochirality: Inducing enantiomeric excess with spin-polarized electrons. *Proceedings of the National Academy of Sciences* **2022,** *119* (28), e2204765119.

13.Chen, Y.; Ma, W., The origin of biological homochirality along with the origin of life. *PLoS Comp. Biol.* **2020,** *16* (1), e1007592.

14.Bada, J. L., Origins of homochirality. *Nature* **1995,** *374* (6523), 594-595.

15.Mondal, P. C.; Fontanesi, C.; Waldeck, D. H.; Naaman, R., Field and Chirality Effects on Electrochemical Charge Transfer Rates: Spin Dependent Electrochemistry. *ACS Nano* **2015,** *9* (3), 3377-3384.

16.Mondal, P. C.; Fontanesi, C.; Waldeck, D. H.; Naaman, R., Spin-Dependent Transport through Chiral Molecules Studied by Spin-Dependent Electrochemistry. *Acc. Chem. Res.* **2016,** *49* (11), 2560-2568.

17.Naaman, R.; Waldeck, D. H., Chiral-Induced Spin Selectivity Effect. *The Journal of Physical Chemistry Letters* **2012,** *3* (16), 2178-2187.

18.Bohannan, E. W.; Nicic, I. M.; Kothari, H. M.; Switzer, J. A., Enantiospecific electrodeposition of chiral CuO films on Cu(110) from aqueous Cu(II) tartrate and amino acid complexes. *Electrochimica Acta* **2007,** *53* (1), 155-160.

19.Moshe, H.; Vanbel, M.; Valev, V. K.; Verbiest, T.; Dressler, D.; Mastai, Y., Chiral Thin Films of Metal Oxide. *Chemistry – A European Journal* **2013,** *19* (31), 10295-10301.

20.Moshe, H.; Levi, G.; Sharon, D.; Mastai, Y., Atomic layer deposition of enantioselective thin film of alumina on chiral self-assembled-monolayer. *Surface Science* **2014,** *629*, 88-93.

2.0 Examining the Effects of Homochirality for Electron Transfer in Protein Assemblies

This chapter was submitted to the Journal of Physical Chemistry and currently under review.

2.1 Introduction

Redox reactions are ubiquitous in nature and play an essential role in biochemical processes, including bioenergetics and photosynthesis.[1] Proteins immobilized on the surface of working electrodes coated with self-assembled monolayers (SAMs) are widely used to mimic fundamental features of electron transfer in biological systems.[2-4] For compact and insulating SAMs, the electron transfer proceeds by electron tunneling through the SAM,[2, 3, 5-7] and the standard heterogeneous electrochemical rate constant can be described using Marcus theory.[2, 3] Although electron transfer reactions in biology are well known, their possible connection with homochirality in biomolecules and their assemblies is not. It is established that natural biological assemblies are predominantly composed of levorotatory/L-amino acid and peptide building blocks, but why nature expresses this preference for homochirality is still a matter of debate. The discovery of chiral induced spin selectivity (CISS)[8] and its manifestation in biomolecules[9, 10] motivates examination of the connection between homochirality and long-range electron transport in supramolecular assemblies of chiral biomolecules. We hypothesize that chirality-based spin filtering can affect electron rates of biomolecular assemblies, somewhat like a spin valve does in a conventional circuit. That is, in heterochiral assemblies, the electron spin orientations conducive to transport in a certain direction abruptly shift (as in a spin valve with electrodes of opposite

magnetization), reducing the overall electron transfer rate. By contrast, homochiral systems maintain a consistent favorable spin orientation across the entire assembly (as in a spin valve with electrodes of the same magnetization), thereby enhancing electron transfer. This work studies the electron transfer through monolayer-coated electrodes to the immobilized protein, cytochrome *c*, as a model system for biological interfaces in which the enantiomeric form of the monolayer film's constituent molecules can be modified.

The CISS effect implies a connection between the electron spin and the efficiency of electron transmission through chiral molecules and chiral supramolecular constructs.[9] While CISS was not addressed in the study of electron transfer before the early 2000s, it has since been shown to manifest for electron transfer in DNA, oligopeptides, small chiral molecules, and chiral inorganic materials.[11-17] More recently, CISS was demonstrated in biomacromolecular systems; Naaman and coworkers showed that the electron conduits in cytochrome proteins MtrF and OmcA, from the bacterium *Shewanella oneidensis* MR-1, are spin polarized,[18] and similar spin-mediated effects have been probed using electrochemical experiments on proteins, such as laccase, cytochrome *c*, and bacteriorhodopsin.[19] Spin constraints arising from the CISS effect can also affect electron transfer kinetics. For instance, Bloom *et al.* showed how the photoinduced electron transfer rate to a chiral nanoparticle acceptor moiety, in a donor-bridge-acceptor assembly, depends on the sense of the circularly polarized light (clockwise versus counterclockwise) used to excite the donor nanoparticle.[20] A similar phenomenon was shown in electrochemical experiments. Tassinari *et al.* reported a chirality dependent asymmetry in the electron transfer rate between ferrocene and a gold substrate tethered through an oligopeptide SAM.[21] While these experiments demonstrate that the chiral components in biomolecules and biomolecular systems possess spin effects, a relationship between the homochirality of such assemblies and CISS has not been

reported. This work uses a modular approach to probe the role of spin polarization during electron transfer between cytochrome *c* (which inherently possesses levorotatory chirality) and ferromagnetic electrodes via short oligopeptide monolayers. Spin constraints on the electron transfer are revealed by magnetizing the electrode parallel or antiparallel to the direction of the electron current, and the effect of the film's chirality on the electron transfer is explored by changing the enantiomeric form of the amino acids comprising the oligopeptide molecules in the monolayer.

Globular cytochrome *c* (Cyt *c*), with its heme iron, was chosen as the redox couple because of its well characterized structure and electron transfer kinetics.[22, 23] The immobilization of Cyt *c* onto a SAM can be achieved in several ways, including electrostatic immobilization between the Cyt *c*'s surface lysine residues and the carboxylate termini of a SAM,[24] amide bond formation between the Cyt *c* surface and the SAM,[25] and ligation between the Cyt *c*'s heme iron and a nitrogen ligand of the SAM.[26] Electrostatic assembly is believed to most closely resemble Cyt *c*'s function *in vivo*, as an electron transport protein in the inner membrane of mitochondria,[23, 27] and hence was the chosen method for this work. Recent work by Clark and coworkers showed that the electrochemical rate constants for Cyt *c* immobilized on the surface of SAMs comprising Cys-Ala-Glu tripeptides are significantly different from that of 11-mercaptoundecanoic acid (11-MUA) SAMs, despite their overall length being similar.[22] Motivated by these studies, this work explores the electron transfer between Cyt *c* and a ferromagnetic electrode, across tripeptide SAMs, as a function of the electrode magnetization and the enantiomeric form (levorotatory, L, versus dextrorotatory, D) of the individual amino acids forming the tripeptide. Changes in the electron transfer kinetics with electrode magnetization are observed and indicate that the charge transport across the tripeptide SAM–Cyt *c* assembly is spin-polarized. The spin effects present in the peptide

assemblies are used to rationalize the stark difference in kinetics between homochiral systems with those possessing varying degrees of heterochirality. In particular, the average charge transfer rate is much faster for homochiral (LLL-tripeptide and L-protein) assemblies, compared to heterochiral (DDD-tripeptide and L-protein or LDL-tripeptide and L-protein) assemblies, for which the average rate constant is reduced by nearly an order of magnitude. These results demonstrate that homochiral assemblies confer a major advantage in facilitating electron transfer, providing a plausible explanation for their prevalence in Nature.

2.2 Results and Discussion

To demonstrate that the tripeptides used in this study exhibit an enantiospecific spin-filtering response (*i.e.*, the CISS effect), Hall measurements were performed. Figure 1A illustrates the experimental arrangement for our studies in which a monolayer of the tripeptide (Cys-Ala-Glu) is chemisorbed on an ultrathin (5 nm) Au film that coats a GaN substrate with an imbedded Hall bar circuit. The peptide-coated electrode is placed in an inert electrolyte solution and biased at a voltage with respect to a counter (or gate) electrode. Upon application of a bias voltage between the working electrode and the counter electrode, a charge displacement current flows in the SAM (double layer charging current). If the charging current is spin-polarized, then it generates a magnetization on the working electrode's surface and gives rise to a voltage between the Hall electrodes (the Hall voltage, V_H), within the imbedded Hall circuit. For a layer of achiral molecules on the electrode surface, no magnetization (V_H is zero) is found; whereas a layer of chiral molecules on the surface gives rise to a nonzero V_H that is enantiospecific.[28] Figure 1B shows representative Hall voltage signals (red) that were measured for a DDD-tripeptide coated electrode,

in which each amino acid is a D enantiomer, on a working electrode at different applied gate voltages, in a 100 mM tetrabutylammonium hexafluorophosphate electrolyte in acetonitrile solution. The initial peak is chosen for analysis as the double-layer charging current, and hence the injected magnetization, is at its maximum.

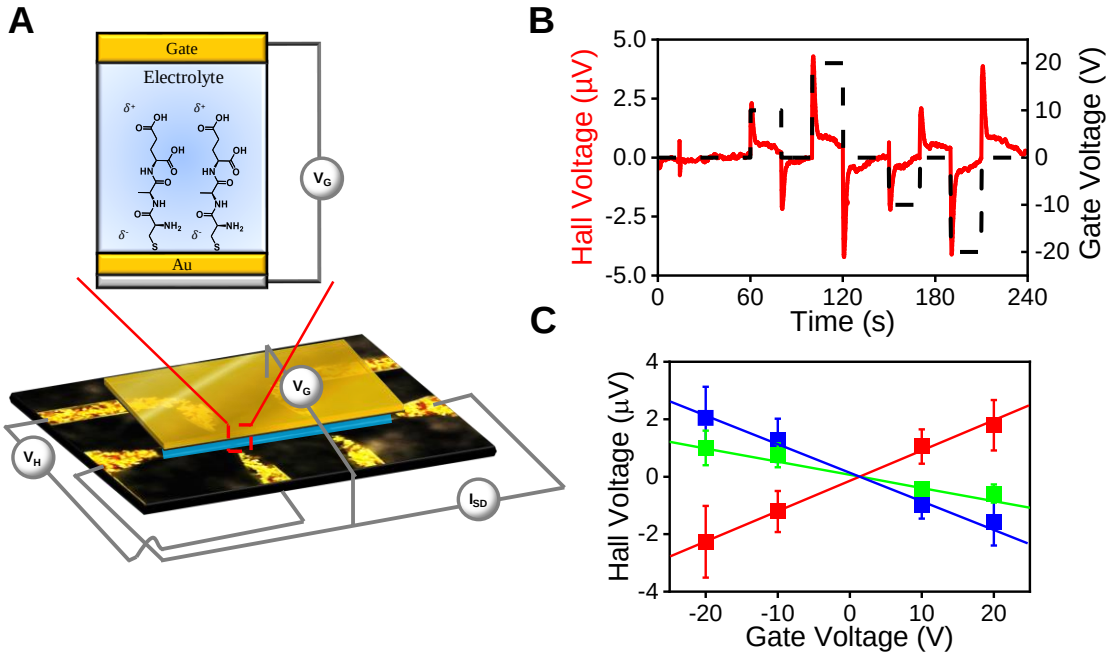

Figure 2-1. Overview of the Hall effect measurements. (A) Schematic view of the experimental set-up for the Hall measurements. (B) Representative time-profile of a measurement in which the square wave feature (black) shows the applied gate voltage versus time and the red waveforms show the corresponding Hall voltage response. (C) Plot of the measured Hall response for the initial spike after application of the gate voltage for LLL- (blue), DDD- (red), and LDL-tripeptide (green) SAMs. The error bars represent one standard deviation of the error over all measurements and devices at the applied gate voltage.

Figure 1C shows the corresponding Hall voltage for LLL-tripeptide (blue) and DDD-tripeptide SAMs (red) under different gate voltages. Measurements were also performed on tripeptides with mixed handedness, L-Cys D-Ala L-Glu (LDL-tripeptide), and they are shown in green. Multiple measurements of each device as a function of the bias voltage, and replicate measurements on multiple devices, show that the Hall voltage changes systematically with the gate voltage; it displays a negative slope for LLL- and LDL-tripeptide SAMs and a positive slope for DDD-tripeptide SAMs. The LDL-tripeptide has a less negative slope than that of the LLL-

tripeptide, which we attribute to its mixed chirality. The antisymmetry of the responses indicates that the LLL-tripeptide and LDL-tripeptide preferentially transmits electrons with their spin aligned antiparallel to their velocity, whereas the DDD-tripeptide transmits electrons with their spin aligned parallel to the velocity.[29, 30] Because previous works have shown a correlation between the chiroptical properties of materials and their spin filtering capabilities[20] and heterochiral tripeptides can adopt the handedness of either enantiomer,[31] the circular dichroism of each tripeptide was measured; see Figure S1. Here, the CD spectra of the LDL-tripeptide more closely resembles that of the LLL-tripeptide and is thus consistent with the spin filtering preference determined in the Hall device measurements.

Cyclic voltammetry was used to study the electron transfer kinetics of immobilized Cyt *c* through different tripeptide monolayers on a ferromagnetic working electrode. Figure 2A shows the experimental scheme in which a ferromagnetic electrode comprising a 100 nm Ni film with a 5 nm Au overlayer to protect the Ni from oxidation and to facilitate the assembly of the tripeptide SAM through cysteine-Au chemisorption; see Supplemental Information regarding characterization of the tripeptide SAMs. In particular, X-ray photoelectron spectroscopy measurements demonstrate that the SAMs densely coat the electrode, and that the coverages for LLL- and DDD-tripeptide SAMs are equal to within the limits of instrumental error (Figure S2 & Table S1). The electrode is magnetized by applying an external magnetic field along the electrode's surface normal, oriented either with the North or South pole toward the electrolyte. The magnetic field splits the spin sublevels of the working electrode's electron distribution and makes the electrode interface sensitive to the spin state of an incoming electron. Oxidation (reduction) of

the Cyt *c* heme unit proceeds by electron (hole) transfer from the immobilized Cyt *c* through the chiral SAM to the electrode.

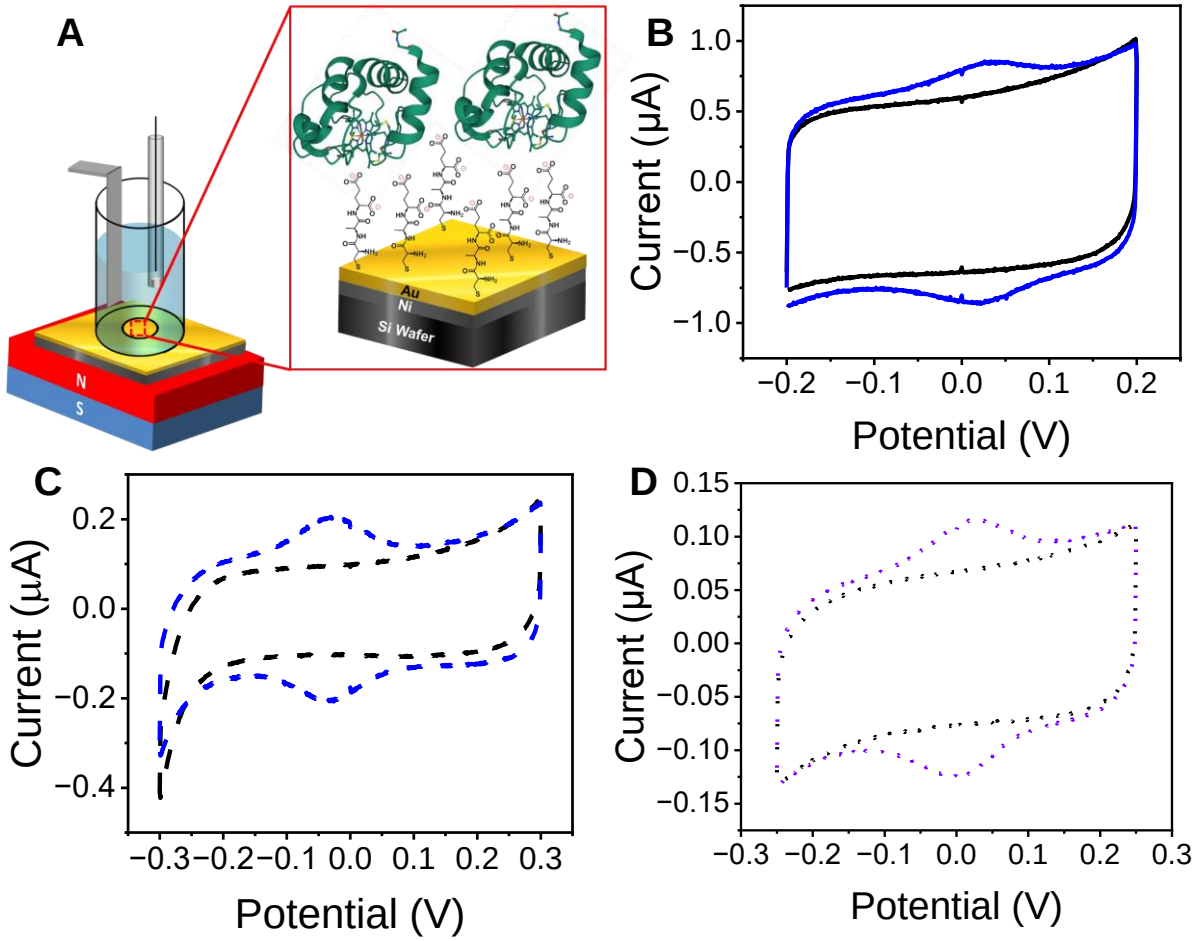

Figure 2-2. Panel A shows a diagram for the electrochemical set-up and the SAM-coated working electrode. The tripeptide molecules were self-assembled on top of a Ni/Au film electrode, and the Cyt *c* was electrostatically immobilized on top of the SAM. The Cyt *c* structure shown is from the Protein Data Bank, code 3o20. (B) Cyclic voltammogram of an LLL-tripeptide SAM before (black) and after (blue) immobilization of Cyt *c*. (C) Plot of the peak current of Cyt *c* immobilized on an LLL-tripeptide SAM vs scan rate. The linear best fit line has an R^2 value of 0.9995. (D) Plot of the Cyt *c* anodic (blue, solid squares) and cathodic (blue, open squares) peak potential shift as a function of the scan rate for an LLL-tripeptide Cyt *c* assembly. The error bars quantify uncertainty in the fitted voltammetric peak positions; see Experimental details. The solid curves are three different theoretical Marcus fits to the experimental data with reorganization energies of 0.1 eV (orange), 0.3 eV (black), and 0.6 eV (grey); The R^2 values for the different reorganization energies are 0.90, 0.94, and 0.92, respectively.

Figure 2B shows cyclic voltammograms for LLL-tripeptide (black) and LLL-tripeptide/Cyt *c* assemblies (blue) using a 100 mV/s scan rate and pH 7 phosphate buffer supporting electrolyte, under a North magnetic field. The full-width-at-half-maximum (FWHM) of 100.8 mV, after background subtraction, indicates that the Cyt *c* electron transfer is quasi-

reversible. The Faradaic current has an integrated charge of 9.82×10^{-8} C and indicates a Cyt *c* coverage of 2.03 pmol/cm^2. Figure S3 shows corresponding data for Cyt *c* immobilized on a mixed film of chiral LLL-tripeptide and achiral C6OH (6-mercapto-1-hexanol) diluent SAM and the case for Cyt *c* immobilized on an achiral control, 11-mercaptoundecanoic acid (11-MUA). The chiral SAM with diluent has a Cyt *c* coverage of 2.01 pmol/cm^2 and a FWHM of 115.8 mV, whereas the 11-MUA SAM has a Cyt *c* coverage of 0.84 pmol/cm^2 and a FWHM of 112.1 mV. Note that, reports of Cyt *c* redox properties on 11-MUA assemblies are comprehensive and consistent with our results.[22, 32-34] A modest shift in the apparent redox potential is present in the different SAM compositions and is likely associated with differences in the charge density on the film.[35]

The standard electrochemical rate constant for Cyt *c* in these assemblies was obtained by measuring the shift in anodic and cathodic peak potential (E_p) as a function of the scan rate. Figure 2C shows a plot of the peak current of the anodic wave of an LLL-tripeptide/Cyt *c* assembly versus the scan rate. The linear dependence between the peak current and the scan rate indicates that the Cyt *c* is immobilized on the monolayer surface, as opposed to free in solution. This experimental design simplifies the extraction of rate constants from the data by eliminating diffusion of the redox protein to the surface. Figure 2D shows a corresponding plot of the apparent anodic (blue, solid symbol) and cathodic (blue, open symbol) potential shift as a function of the scan rate. A fit to these data is then performed using Marcus theory, with the standard heterogeneous rate constant, k^0, the formal potential, E^0, and the reorganization energy, λ, as adjustable parameters.[23] The data analysis, however, does not depend strongly on the reorganization energy; Figure 2D shows that a Marcus fit using λ = 0.1 eV (orange), 0.3 eV (black), and 0.6 eV (grey) does not give appreciable changes in R^2 values for the data fitting; 0.90 for λ = 0.1 eV, 0.94 for λ = 0.3 eV, and 0.92 for λ = 0.6 eV. For this reason, λ = 0.3 eV was used exclusively for the determination of k^0, consistent

with reported values in previous studies.[23, 36] With this choice, curve fitting is optimized by adjusting k^0 and E^0, which corresponds to the electron transfer rate constant and formal potential between the electrode and the iron co-factor of the protein at $\Delta G = 0$.

To probe the effect of spin on the electron transport, the ferromagnetic electrode was magnetized by an external magnet (0.5 T) such that its field was oriented normal to the electrode surface. The difference in rate constant with applied magnetic field orientation, North vs South, were compared through an asymmetry polarization parameter, *A*, defined as

$$A = \frac{k^0_{parallel} - k^0_{antiparallel}}{<k^0>} \quad \text{and} < k^0 >= \frac{1}{2}(k^0_{parallel} + k^0_{antiparallel}) \qquad \textbf{Eqn. 1}$$

where $k^0_{parallel}$ and $k^0_{antiparallel}$ correspond to rate constants in which the applied magnetic field causes the electron velocity to be aligned parallel or antiparallel to its spin, respectively. Here placing the South pole of the magnet beneath the electrode corresponds to the parallel magnetization, and North to the antiparallel magnetization). Figure 3A shows *A* determined for Cyt *c* immobilized on LLL-tripeptide SAMs (blue), DDD-tripeptide SAMs (red), LDL-tripeptide SAMs (green), and achiral 11-MUA SAMs (purple) collected at pH = 7 for four different solution ionic strengths. Tables S2 and S3 report the average *A* and number of trials for each ionic strength using pure and diluted SAMs, respectively. While the asymmetry parameter for a particular chiral SAM-Cyt *c* assembly shows variations with ionic strength, the asymmetry in electron transfer rate

persists across different ionic strengths and indicates a magnetic field dependence, even as the solution resistance changes.

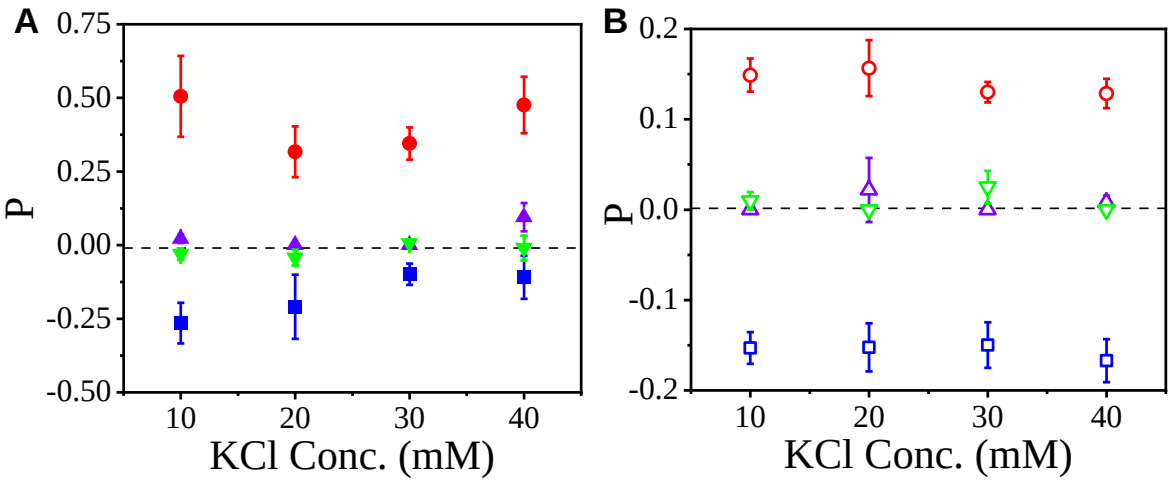

Figure 2-3. (A) The asymmetry in electron transfer rate constants is plotted versus the solution ionic strength for Cyt *c* immobilized on an LLL-tripeptide SAM (blue), DDD-tripeptide SAM (red), LDL-tripeptide (green), and achiral 11-mercaptoundecanoic acid SAM (purple) at four different ionic strengths. (B) Asymmetry in electron transfer rates for Cyt *c* immobilized on an LLL-tripeptide SAM (blue, open symbol), DDD-tripeptide SAM (red, open symbol), LDL-tripeptide (green, open symbol), and achiral 11-MUA SAM (purple, open symbol) at 4 different ionic strengths.

For the LLL-tripeptide assemblies, k^0 is larger when the electron transport is antiparallel to its spin whereas the opposite is true for the DDD-tripeptide assemblies, k^0 is larger when the electron transport is parallel to its spin. The change in sign of *A*, associated with oligopeptide handedness demonstrates that the SAM-coated electrode acts as a source of spin-polarized electrons that interact in a spin-dependent manner with the Cyt *c*. Because variables like temperature and reorganization energy do not change significantly with the magnetic field direction, and $\Delta G = 0$, the change in rate constants is assumed to arise from changes in the electronic coupling between the Cyt *c* and the SAM. In contrast, k^0 for 11-MUA and LDL-tripeptide assemblies are invariant with spin orientation. While the behavior of the LDL-tripeptide assemblies is surprising, considering the Hall response shown in Figure 1, the weaker spin polarization of the LDL oligopeptides may preclude rate constant asymmetries beyond the detection limit of our measurement system.

Figure 3B shows an analogous series of experiments to those in Figure 3A, but instead uses mixed SAMs comprising C6OH diluent molecules and the tripeptides, or 11-MUA. These data show the same general trend as the pure SAMs in that the achiral 11-MUA and the LDL-tripeptide containing assemblies show no significant rate asymmetry and the LLL-tripeptide and DDD-tripeptide containing assemblies show *A* of opposite signs. The magnitude of the *A* for the assemblies with LLL-tripeptides/C6OH and DDD-tripeptide/C6OH SAMs are lower than that found for those with pure LLL-tripeptides and DDD-tripeptide SAMs; however, they are more similar in magnitude to each other than those with the pure films were. Two distinct, but related, possible explanations for the reduced asymmetry are:

- The voltammograms have contributions from current flow through both the achiral C6OH diluent and the tripeptides, and this feature dilutes the overall magnitude of *A*; *e.g.*, half of the current flows through the achiral C6OH ($A \sim 0$) and the other half of the current flows through the homochiral tripeptide ($|A| \sim 0.30$) then the net asymmetry in rate constant would be polarized at $|A| \sim 0.15$. Such an explanation requires that the immobilized protein is located near regions of the film with a significant percentage of C6OH. Given that the cross-sectional area of Cyt *c* is approximately 0.105 nm^2,[22] it is plausible that it interacts with ~13 SAM molecules in the film and some dilution of the tunneling current's spin polarization is expected.
- Some theoretical models[37, 38] for spin-filtering of electrons through peptide SAMs on ferromagnetic electrodes posit that the spin filtering occurs at the FM electrode/chiral molecule boundary. In this case, the presence of achiral molecules in the film may reduce the net spin polarization of the electron current at the interface and hence the magnitude of the asymmetry in electrochemical rate constants.

Collectively, the data summarized in Figure 3 demonstrate that the electron current moving through the LLL-tripeptides and DDD-tripeptides is spin-polarized and that it depends on the magnetization of the electrode and the handedness of the chiral molecules, a hallmark of the CISS effect.

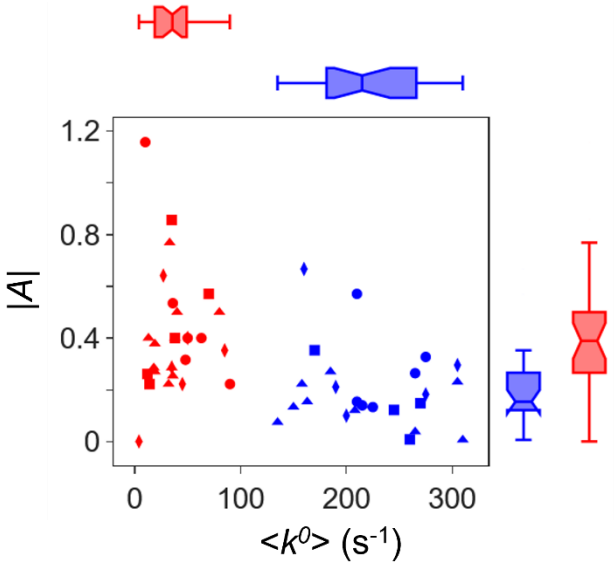

Figure 2-4. Plot of the magnitude of rate constant asymmetry, $|A|$, for LLL-tripeptide (blue) and DDD-tripeptide assemblies as a function of the average rate constant, $\langle k^0 \rangle$, for different electrode preparations and solution conditions; 10 mM KCl (circles), 20mM KCl (diamonds), 30 mM KCl (triangles) and 40mM KCl (squares). The horizontal blue and red box plots on top of the figure represent statistics of $\langle k^0 \rangle$ values of LLL-tripeptide and DDD-tripeptide assemblies, respectively, and the vertical blue and red box plots on the right of the figure represent statistics of |A| values of LLL-tripeptide and DDD-tripeptide assemblies, respectively. For each box plot, the central line represents the median of the data, the box represents the interquartile range (IQR), the whiskers extend to the extreme observed data points falling within 1.5 IQRs of the median, and the notches represent an estimate of the 95% confidence interval that can be used to characterize the statistical significance of differences among the populations.

In addition to a magnetic field dependence for the electrochemical rate constants in the LLL-tripeptide and DDD-tripeptide assemblies, we also observed a difference in the magnitudes of the average rate constants, $\langle k^0 \rangle$ (see Eqn. 1). While the electrochemical rate constants obtained for the tripeptides vary from one electrode preparation to the next, such behavior among differently prepared electrodes is not uncommon. For example, different works studying Cyt *c* immobilized on 11-MUA SAMs on Au substrates report k^0 values that vary from 10 s^{-1} to 100 s^{-1}.[22, 32-34] To explore whether the observed values of k^0 affect the observed changes in *A*, extended trials for

additional electrode preparations comprising LLL-tripeptide (blue) and DDD-tripeptide (red) assemblies were performed and are plotted in Figure4 and in Tables S4 and S5. Each data point represents a single measurement and variations in coverage and film structural quality, among independently prepared electrodes, are not minimized. Box and whisker plots are shown adjacent to the figure and illustrate that *i*) the |*A*| does not possess a significant correlation with $< k^0 >$, *ii*) the |*A*| is different for LLL-tripeptide and DDD-tripeptide assemblies, as neither the estimated 95% confidence intervals about the median nor the interquartile ranges overlap, and *iii*) the $< k^0 >$ of LLL-tripeptide and DDD-tripeptide assemblies are significantly different. We posit that the differences in the |*A*| between LLL-tripeptide and DDD-tripeptides assemblies is associated with structural stereoisomeric effects, seeing as how differences in asymmetry are minimized upon inclusion of a diluent; see Figure 3B. More strikingly, a large difference in $< k^0 >$, greater than 10-fold, is observed among the LLL-tripeptide and DDD-tripeptides assemblies; see Table 1. The change in $<k^0>$ is reflected by the homochirality or heterochirality of the ensemble namely, the handedness of the SAM, and its constituents, with respect to the handedness of the protein. For homochiral assemblies (LLL-tripeptide/Cyt *c*) $<k^0>$ is fast; however, when the homochirality of the assembly is interrupted, either between the SAM and Cyt *c* or within the SAM itself, a stark reduction of rate constants occurs. These data imply that the spin-filtering effects of chiral building blocks in nature lead to more efficient electron transfer for homochiral systems.

Table 2-1. $\langle k^0 \rangle$ for different SAMs, with 30 mM KCl.

SAM composition	$\langle k^0 \rangle$ (s^{-1})
LLL only	209 ± 20
DDD only	33 ± 5
11-MUA only	31 ± 4
LDL only	22 ± 2

2.3 Conclusion

This work establishes that assemblies comprising biological building blocks not only promote spin-filtering in electron transfer, but also increase the efficiency of electron transfer. Experiments on Cyt *c* assemblies immobilized on tripeptide SAMs in which all of the amino acids are the same enantiomer, *i.e.* LLL-tripeptides and DDD-tripeptides display a dependence of their electron transfer rate on the direction of a ferromagnetic electrode's magnetization. Conversely, SAMs comprising molecules that are achiral or of mixed chirality, *e.g.* 11-MUA or LDL-tripeptides, do not. Moreover, breaking the homochirality of the SAM-Cyt *c* assemblies, regardless of whether the interruption occurs between the tripeptide SAM and the Cyt *c* protein or within the tripeptide itself, causes a dramatic reduction in the electron transfer rate. Both the spin polarization and electron transfer rate effects arise from spin constraints during electron transmission, consistent with the chiral induced spin selectivity effect. This study shows that electron spin has profound importance for governing electron transfer processes in biological systems and related physical phenomena.

2.4 Experimental

2.4.1 Hall Effect Device Fabrication and Measurement

Hall effect devices were fabricated as reported previously[1] and cleaned by boiling in acetone (99.5%, Fisher) and in 2-propanol (99.5%, Fisher Chemical), rinsed in 2-propanol and water, and dried under a stream of Ar gas (90-99%, Matheson Tri-Gas, Inc.). The devices were then oxidized in a UV/Ozone cleaner (UV. TC. NA. 003, Bioforce Nanoscience Inc.) for 2 minutes and placed in ethanol for at least 30 minutes prior to incubation. The device was incubated in a 3.5 mM oligopeptide (95%, Genemed Synthesis Inc.) solution in ethanol (200 proof, Fisher Chemical) for 48 hours. Following incubation, the coated Au surface was rinsed with 3 M KCl (99%, Fisher Chemical), followed by deionized H_2O, and then dried under an Ar stream. A polydimethylsiloxane (PDMS) (Sylgard 184) electrochemical cell was assembled around the device and cured for 18 hours at 45°C.

Measurements were conducted in 100 mM tetrabutylammonium hexafluorophosphate ($TBAPF_6$) (98%, Sigma-Aldrich) electrolyte in acetonitrile (99.8%, anhydrous, Sigma-Aldrich). Using a Keithley 2636 source measure unit, a constant current of 50 μA is applied between the 'source' and 'drain' while a polarizing 'gate' voltage is applied perpendicular to both the source-drain current and the Hall voltage probes. The voltage was electrically insulated from the solution by a ~0.18 mm thick glass slide. The Hall voltage is measured using a Keithley Nanovoltmeter 2182A device. The direction of the source-drain current was then reversed, and the measurements repeated, to account for any asymmetry in the device.

2.4.2 Electrode Fabrication, SAM Preparation, and Cytochrome c Assembly

The working electrodes were fabricated by evaporating 100 nm of Ni, followed by 5 nm of Au, onto a glass microscope slide (Fisher Scientific) or silicon wafer (University Wafer Inc.) that possessed a 5 nm Ti adhesion layer using a Plassys electron beam evaporator MEB550S. Following evaporation, the electrode was fixed onto the bottom of an electrochemical cell using silicone caulk (General Electric) and allowed to cure overnight. The circular cutout on the bottom of the cell has a diameter of ~6 mm and acts to define the geometric active area (~0.28 cm^2) for the working electrode. After the silicone caulk was cured, a SAM solution containing either pure oligopeptide or oligopeptide mixed with a diluent was added to the electrochemical cell and incubated for 48 hours. The incubation solution for assembly of the pure SAM was 2 mM of oligopeptide dissolved in ethanol. For mixed SAMs the concentration of the oligopeptide was the same, but the solution also included 1.5 mM 6-mercapto-1-hexanol (98%, Tokyo Chemical Industry), of a diluent molecule. Following incubation, the electrode was rinsed with fresh ethanol and 4.4 mM phosphate buffer solutions (pH = 7, 99.8%, Fisher Chemical). To immobilize Cyt *c* (95%, Sigma-Aldrich) on top of the SAM, a Cyt *c* solution comprising 30 µM equine heart Cyt *c* in 4.4 mM phosphate buffer was added to the washed electrochemical cell and incubated for at least 1 hour. The cell was then rinsed with 40 mM KCl solution to remove any weakly adsorbed Cyt *c*.

2.4.3 SAM and Tripeptide Characterization

X-ray photoelectron spectroscopy measurements were performed using a Thermo Fisher ESCALAB 250 Xi instrument on Au electrodes and referenced to adventitious carbon (284.8 eV).

The SAM surface coverage was determined using previously established methods.[2] Circular dichroism (CD) spectroscopy was used to measure the chiroptical properties of the tripeptides using an Olis DSM 17 CD spectropolarimeter.

2.4.4 Cyclic Voltammetry

All of the electrochemical measurements were performed using a CH Instruments 618b potentiostat in a CH Instruments 200B Faraday cage. The reference electrode was Ag/AgCl in 3 M KCl and the counter electrode was a Pt wire. The distance between the working electrode and the reference electrode was fixed at 4 mm. Prior to the cyclic voltammetry, a magnet with a strength of 0.5 T was placed directly beneath the working electrode and the magnet was oriented with either its north or south pole perpendicular to the electrode surface. The magnet was located outside of the electrochemical cell and changing the field's orientation did not alter the cell arrangement or geometry. The cyclic voltammograms were collected over a potential range from -0.3 V to 0.3 V and the scan rate was varied from 40 mV/s to 6000 mV/s.

The accuracy of k^0 depends sensitively on the peak potential and possible distortion of the peak assignment from non-faradaic background current in each voltammogram. To reliably assign the peak potentials in the voltammogram, the analysis uses a background and Voigt peak fitting function; see the SI for a more detailed discussion and corresponding Python script used for analysis. Three separate scans at each scan rate for each electrode were averaged to characterize and mitigate uncertainty in the peak potential and peak currents. In addition, a minimum of three independent electrode preparations were made for each series of experiments. The k^0 values obtained from a Marcus analysis were used to quantify how the electron transfer depends on the

electrode's magnetization and the enantiomeric form of the amino acids comprising the tripeptide SAMs.

2.5 Associated Content

Supporting Information

Figure S1 - Circular dichroism measurements of tripeptide solutions, Figure S2 – Representative XPS of LLL-tripeptide self-assembled monolayer, Figure S3 – Voltammetry of LLL-tripeptide with C6OH diluent SAM, and 11-MUA tripeptide, assemblies before and after immobilization of Cyt *c*, Table S1 – Surface coverage of tripeptide self-assembled monolayers, Table S2 – Experimental data for Figure 3, Table S3 – Experimental data for Figure 3, Table S4 – Experimental data of LLL-tripeptide assemblies in Figure 4, Table S5 – Experimental data of DDD-tripeptide assemblies in Figure 4, Supplementary Note 1 – Python script for data analysis.

AUTHOR INFORMATION

Corresponding Author

*David H. Waldeck

Address: University of Pittsburgh, 219 Parkman Ave, Pittsburgh, PA, USA 15260

Email: dave@pitt.edu

Phone: 412-624-8430

Competing Interest

The authors declare no competing interest.

ACKNOWLEDGMENT

The authors acknowledge support from the National Science Foundation grant CHE-1900078

2.6 Reference

1.Moser, C. C.; Keske, J. M.; Warncke, K.; Farid, R. S.; Dutton, P. L., Nature of biological electron transfer. *Nature* **1992,** *355* (6363), 796-802.

2.Waldeck, D. H.; Khoshtariya, D. E., Fundamental Studies of Long- and Short-Range Electron Exchange Mechanisms between Electrodes and Proteins. In *Applications of Electrochemistry and Nanotechnology in Biology and Medicine I*, Eliaz, N., Ed. Springer New York: New York, NY, 2011; pp 105-238.

3.Yue, H.; Khoshtariya, D.; Waldeck, D. H.; Grochol, J.; Hildebrandt, P.; Murgida, D. H., On the Electron Transfer Mechanism Between Cytochrome c and Metal Electrodes. Evidence for Dynamic Control at Short Distances. *J. Phys. Chem. B* **2006,** *110* (40), 19906-19913.

4.Léger, C.; Bertrand, P., Direct Electrochemistry of Redox Enzymes as a Tool for Mechanistic Studies. *Chem. Rev.* **2008,** *108* (7), 2379-2438.

5.Shah, A.; Adhikari, B.; Martic, S.; Munir, A.; Shahzad, S.; Ahmad, K.; Kraatz, H.-B., Electron transfer in peptides. *Chem. Soc. Rev.* **2015,** *44* (4), 1015-1027.

6.Smalley, J. F.; Feldberg, S. W.; Chidsey, C. E. D.; Linford, M. R.; Newton, M. D.; Liu, Y.-P., The Kinetics of Electron Transfer Through Ferrocene-Terminated Alkanethiol Monolayers on Gold. *J. Phys. Chem.* **1995,** *99* (35), 13141-13149.

7.Giese, B.; Graber, M.; Cordes, M., Electron transfer in peptides and proteins. *Curr. Opin. Chem. Biol.* **2008,** *12* (6), 755-759.

8.Ray, K.; Ananthavel, S. P.; Waldeck, D. H.; Naaman, R., Asymmetric Scattering of Polarized Electrons by Organized Organic Films of Chiral Molecules. *Science* **1999,** *283* (5403), 814-816.

9.Michaeli, K.; Kantor-Uriel, N.; Naaman, R.; Waldeck, D. H., The electron's spin and molecular chirality – how are they related and how do they affect life processes? *Chem. Soc. Rev.* **2016,** *45* (23), 6478-6487.

10.Naaman, R.; Paltiel, Y.; Waldeck, D. H., Chiral Induced Spin Selectivity and Its Implications for Biological Functions. *Annu. Rev. Biophys.* **2022,** *51* (1), 99-114.

11.Abendroth, J. M.; Stemer, D. M.; Bloom, B. P.; Roy, P.; Naaman, R.; Waldeck, D. H.; Weiss, P. S.; Mondal, P. C., Spin Selectivity in Photoinduced Charge-Transfer Mediated by Chiral Molecules. *ACS Nano* **2019,** *13* (5), 4928-4946.

12.Kim, Y.-H.; Zhai, Y.; Lu, H.; Pan, X.; Xiao, C.; Gaulding, E. A.; Harvey Steven, P.; Berry Joseph, J.; Vardeny Zeev, V.; Luther Joseph, M.; Beard Matthew, C., Chiral-induced spin selectivity enables a room-temperature spin light-emitting diode. *Science* **2021,** *371* (6534), 1129-1133.

13.Naaman, R.; Paltiel, Y.; Waldeck, D. H., Chiral molecules and the electron spin. *Nat. Rev. Chem.* **2019,** *3* (4), 250-260.

14.Naaman, R.; Waldeck, D. H., Chiral-Induced Spin Selectivity Effect. *J. Phys. Chem. Lett.* **2012,** *3* (16), 2178-2187.

15.Naaman, R.; Fontanesi, C.; Waldeck, D. H., Chirality and its role in the electronic properties of peptides: spin filtering and spin polarization. *Current Opinion in Electrochemistry* **2019,** *14*, 138-142.

16.Ghosh, K. B.; Zhang, W.; Tassinari, F.; Mastai, Y.; Lidor-Shalev, O.; Naaman, R.; Möllers, P.; Nürenberg, D.; Zacharias, H.; Wei, J.; Wierzbinski, E.; Waldeck, D. H., Controlling Chemical Selectivity in Electrocatalysis with Chiral CuO-Coated Electrodes. *J. Phys. Chem. C* **2019,** *123* (5), 3024-3031.

17.Bloom, B. P.; Kiran, V.; Varade, V.; Naaman, R.; Waldeck, D. H., Spin Selective Charge Transport through Cysteine Capped CdSe Quantum Dots. *Nano Lett.* **2016,** *16* (7), 4583-4589.

18.Mishra, S.; Pirbadian, S.; Mondal, A. K.; El-Naggar, M. Y.; Naaman, R., Spin-Dependent Electron Transport through Bacterial Cell Surface Multiheme Electron Conduits. *J. Am. Chem. Soc.* **2019,** *141* (49), 19198-19202.

19.Varade, V.; Markus, T.; Vankayala, K.; Friedman, N.; Sheves, M.; Waldeck, D. H.; Naaman, R., Bacteriorhodopsin based non-magnetic spin filters for biomolecular spintronics. *Phys. Chem. Chem. Phys.* **2018,** *20* (2), 1091-1097.

20.Bloom, B. P.; Graff, B. M.; Ghosh, S.; Beratan, D. N.; Waldeck, D. H., Chirality Control of Electron Transfer in Quantum Dot Assemblies. *J. Am. Chem. Soc.* **2017,** *139* (26), 9038-9043.

21.Tassinari, F.; Jayarathna, D. R.; Kantor-Uriel, N.; Davis, K. L.; Varade, V.; Achim, C.; Naaman, R., Chirality Dependent Charge Transfer Rate in Oligopeptides. *Adv. Mater.* **2018,** *30* (21), 1706423.

22.Yawitz, T. M.; Patterson, K. S.; Onkst, B. X.; Youmbi, F.; Clark, R. A., Cytochrome c electrochemistry on peptide self-assembled monolayers. *J. Electroanal. Chem.* **2018,** *828*, 59-62.

23.Alvarez-Paggi, D.; Hannibal, L.; Castro, M. A.; Oviedo-Rouco, S.; Demicheli, V.; Tórtora, V.; Tomasina, F.; Radi, R.; Murgida, D. H., Multifunctional Cytochrome c: Learning New Tricks from an Old Dog. *Chem. Rev.* **2017,** *117* (21), 13382-13460.

24.Khoshtariya, D. E.; Wei, J.; Liu, H.; Yue, H.; Waldeck, D. H., Charge-Transfer Mechanism for Cytochrome c Adsorbed on Nanometer Thick Films. Distinguishing Frictional Control from Conformational Gating. *J. Am. Chem. Soc.* **2003,** *125* (25), 7704-7714.

25.Davis, K. L.; Drews, B. J.; Yue, H.; Waldeck, D. H.; Knorr, K.; Clark, R. A., Electron-Transfer Kinetics of Covalently Attached Cytochrome c/SAM/Au Electrode Assemblies. *J. Phys. Chem. C* **2008,** *112* (16), 6571-6576.

26.Wei, J.; Liu, H.; Dick, A. R.; Yamamoto, H.; He, Y.; Waldeck, D. H., Direct Wiring of Cytochrome c's Heme Unit to an Electrode: Electrochemical Studies. *J. Am. Chem. Soc.* **2002,** *124* (32), 9591-9599.

27.Ishigami, I.; Zatsepin, N. A.; Hikita, M.; Conrad, C. E.; Nelson, G.; Coe, J. D.; Basu, S.; Grant, T. D.; Seaberg, M. H.; Sierra, R. G.; Hunter, M. S.; Fromme, P.; Fromme, R.; Yeh, S.-R.; Rousseau, D. L., Crystal structure of CO-bound cytochrome c oxidase determined by serial femtosecond X-ray crystallography at room temperature. *Proc. Natl. Acad. Sci. U.S.A.* **2017,** *114* (30), 8011.

28.Kumar, A.; Capua, E.; Kesharwani, M. K.; Martin, J. M. L.; Sitbon, E.; Waldeck, D. H.; Naaman, R., Chirality-induced spin polarization places symmetry constraints on biomolecular interactions. *Proc. Natl. Acad. Sci. U.S.A.* **2017,** *114* (10), 2474.

29.Kettner, M.; Göhler, B.; Zacharias, H.; Mishra, D.; Kiran, V.; Naaman, R.; Waldeck, D. H.; Sęk, S.; Pawłowski, J.; Juhaniewicz, J., Spin Filtering in Electron Transport Through Chiral Oligopeptides. *The Journal of Physical Chemistry C* **2015,** *119* (26), 14542-14547.

30.Clever, C.; Wierzbinski, E.; Bloom, B. P.; Lu, Y.; Grimm, H. M.; Rao, S. R.; Horne, W. S.; Waldeck, D. H., Benchmarking Chiral Induced Spin Selectivity Measurements - Towards

Meaningful Comparisons of Chiral Biomolecule Spin Polarizations. *Isr. J. Chem.* **2022,** *62* (11-12), e202200045.

31.Marchesan, S.; Easton, C. D.; Styan, K. E.; Waddington, L. J.; Kushkaki, F.; Goodall, L.; McLean, K. M.; Forsythe, J. S.; Hartley, P. G., Chirality effects at each amino acid position on tripeptide self-assembly into hydrogel biomaterials. *Nanoscale* **2014,** *6* (10), 5172-5180.

32.El Kasmi, A.; Wallace, J. M.; Bowden, E. F.; Binet, S. M.; Linderman, R. J., Controlling Interfacial Electron-Transfer Kinetics of Cytochrome c with Mixed Self-Assembled Monolayers. *J. Am. Chem. Soc.* **1998,** *120* (1), 225-226.

33.Tanimura, R.; Hill, M.; Margoliash, E.; Niki, K.; Ohno, H.; Gray, H., Active Carboxylic Acid-Terminated Alkanethiol Self-Assembled Monolayers on Gold Bead Electrodes for Immobilization of Cytochromes c. *Electrochem. Solid-State Lett.* **2002,** *5*.

34.Wei, J. J.; Liu, H.; Niki, K.; Margoliash, E.; Waldeck, D. H., Probing Electron Tunneling Pathways: Electrochemical Study of Rat Heart Cytochrome c and Its Mutant on Pyridine-Terminated SAMs. *J. Phys. Chem. B* **2004,** *108* (43), 16912-16917.

35.Petrović, J.; Clark, R. A.; Yue, H.; Waldeck, D. H.; Bowden, E. F., Impact of Surface Immobilization and Solution Ionic Strength on the Formal Potential of Immobilized Cytochrome c. *Langmuir* **2005,** *21* (14), 6308-6316.

36.Weidinger, I. M.; Murgida, D. H.; Dong, W.-f.; Möhwald, H.; Hildebrandt, P., Redox Processes of Cytochrome c Immobilized on Solid Supported Polyelectrolyte Multilayers. *The Journal of Physical Chemistry B* **2006,** *110* (1), 522-529.

37.Alwan, S.; Dubi, Y., Spinterface Origin for the Chirality-Induced Spin-Selectivity Effect. *J. Am. Chem. Soc.* **2021,** *143* (35), 14235-14241.

38.Wolf, Y.; Liu, Y.; Xiao, J.; Park, N.; Yan, B., Unusual Spin Polarization in the Chirality-Induced Spin Selectivity. *ACS Nano* **2022,** *16* (11), 18601-18607.

3.0 Controlling Chemical Selectivity in Electrocatalysis with Chiral CuO Coated Electrodes

This chapter was reprinted with permission from Ghosh, K. B.; Zhang, W.; Tassinari, F.; Mastai, Y.; Lidor-Shalev, O.; Naaman, R.; Möllers, P.; Nürenberg, D.; Zacharias, H.; Wei, J.; Wierzbinski, E.; Waldeck, D. H., Controlling Chemical Selectivity in Electrocatalysis with Chiral CuO-Coated Electrodes. *The Journal of Physical Chemistry C* **2019,** *123* (5), 3024-3031. I was reponsible for developing the electrodeposition method of the chiral CuO films, making the CuO films and collecting the UV-Vis spectrum, circular dichorism spectrum, and the linear sweep voltammetry studies of the oxygen evolution reaction. The rest of the work was done by our collaborators.

3.1 Introduction

Since its initial report in 1999,[1] a variety of experimental methods have been used to demonstrate that the electron transmission through chiral molecules and chiral molecular films is spin-dependent.[2] The chiral-induced spin selectivity (CISS) effect results from the motion of the electron probability density in the chiral electrostatic field of the molecules, which gives rise to an effective magnetic field, in the rest frame of the electron, that acts on the electron's magnetic moment.[3, 4] Experimental studies have shown that the effect manifests in a variety of processes, ranging from electron transfer in redox proteins and multi-electron redox processes with chiral electrodes[5] to organic spintronic devices,[6] but all of these studies involve organic molecules in the

electron transmission process. Applications in electronics and in electrocatalysis would benefit from robust inorganic nanomaterials that act as a spin filter.

The present work describes the creation of ultrathin, inorganic, chiral CuO films which act as spin filters and demonstrates their use for controlling the product formation in electrocatalytic water-splitting. CuO films were grown by electrodeposition onto electrodes from an electrolyte solution containing chiral Cu(II) complexes, and the film's chiral nature was confirmed by circular dichroism spectroscopy. Spin-dependent photoemission spectroscopy was used to measure the spin filtering of electrons by the ultrathin (5 nm to 50 nm) CuO films on Au electrodes. This method was used in earlier work to demonstrate the spin filtering properties of chiral molecular layers of ds-DNA oligomers,[7] proteins,[8] oligopeptides,[9] and helicene[10] on Au, as well as on other substrates like Al,[8] Si,[11] Cu, and Ag.[10]

Photoelectrochemical water splitting has received much attention as a possible path for the production of hydrogen from water, however the efficiency of the oxygen evolution reaction (OER) on the anode remains a roadblock to widespread applications. In OER, the production of O_2 molecules requires transfer of four electrons and the kinetically favorable OER process is believed to occur through a multi-step reaction with single-electron transfers at each step. It has been found that the electrochemical OER process requires a significant overpotential,[12, 13] of about 0.4 V,[14] and extensive research effort has focused on finding a suitable catalyst that reduces this overpotential.[15-21] Theoretical work suggests that the overpotential arises from electron spin restrictions in forming the ground state triplet oxygen molecule.[22-24] While magnetic electrodes have been shown to address this challenge, they have not proven economically or technologically viable.[25, 26] In recent experimental work with chiral, organic molecule-coated anodes, it has been shown that the overpotential is reduced and the formation of hydrogen peroxide as a by-product is

suppressed;[27-29] albeit with a low overall current density (microamps/cm^2). Higher current was obtained by using chiral-molecule-coated iron oxide nanoparticles as a catalyst.[30]

Because of the CISS effect, a chiral electrocatalyst should polarize the electron spin distribution on the catalytic surface and favor the production of the spin allowed triplet oxygen channel over that of singlet oxygen and hydrogen peroxide. CuO is a small bandgap (1.3 to 1.7 eV) material that is known to display (photo)electrocatalytic properties for the water splitting reaction,[31-33] and we postulate that chiral CuO should be a more efficient electrocatalyst than achiral CuO. Tafel plots of CuO imply that the initial formation and stabilization of hydroxyl and/or peroxyl surface species are rate-limiting.[34] When the anode is coated with a chiral CuO layer, the electron transfer from the hydroxide species to the anode is spin-specific, leaving the unpaired electrons on the hydroxyl radicals aligned in a spin parallel fashion. Because the ground state oxygen molecule is a triplet, the reaction of two hydroxyl radicals of parallel spins is spin-allowed. In contrast, the formation of hydrogen peroxide, which is a singlet species, is spin-forbidden. For the case of an achiral anode, no correlation between the spins of the two hydroxyl radicals is expected and the interaction between the two hydroxyls may occur on a singlet surface, which correlates with the production of hydrogen peroxide (H_2O_2) by-product.

In the present study, we report on the role played by chirality for inorganic CuO anodes in electrochemical water splitting. We find that the CuO chirality reduces the overpotential and suppresses the production of the hydrogen peroxide by-product, while maintaining currents that are orders of magnitude higher than that obtained when the electrode is coated with organic chiral molecules. The manuscript is divided into three major parts. First we describe the creation of CuO films, their characterization, and their circular dichroism properties. Second we describe the Mott-polarimetry photoemission measurements for electrodeposited chiral CuO films. Third, we

describe our measurements of the oxygen evolution reaction (OER) for different chiral CuO anodes.

3.2 Experimental

3.2.1 Growth and Characterization of CuO films

Metal oxide films, which are typically considered to be achiral, can display chirality if the film deposition process or the substrate has a chiral bias. In this work, the electrodeposition method, pioneered by Switzer et al.,[35] is used to create a chiral CuO film on polycrystalline gold and on TiO_2/FTO thin film electrodes. In this method, the CuO film is electrodeposited from an electrolyte solution that contains chiral complexes of Cu-tartrate, and the CuO film growth occurs through irreversible electro-oxidation of the tartrate ligand, leaving a pure CuO layer on the substrate. Even though the bulk structure of CuO is achiral, the CuO films electrodeposited by way of Cu(II)-tartrate complexes display a preferred chiral crystallographic orientation; e.g., films deposited on Au(001) from Cu^{2+}/L-tartaric acid solution have a $(1\bar{1}\bar{1})$ orientation, and those electrodeposited from Cu^{2+}/D-tartaric acid solution have a preferred $(\bar{1}11)$ orientation.[35, 36]

CuO films were grown from a basic (3M NaOH) solution of 0.2 M Cu-tartrate, and subsequently were baked to remove any moisture and to oxidize any Cu_2O. The film thickness was determined by optical absorbance and atomic force microscopy measurements, and X-ray photoelectron spectra were obtained to confirm that the films were >99% pure CuO [see supporting information S1 and S2 (Figure S1-S6) for further details]. The film chirality was confirmed by circular dichroism (CD) spectroscopy.

3.2.2 Photoemission Measurements

The spin polarization of the photoemitted electrons was measured as a function of the CuO film thickness and the CuO chirality. The photoemission spectrometer (see Figure S7 in SI) and the Mott polarimetry method have been described previously.[7] Photoelectrons were ejected from the Au/CuO films by excitation with a 213 nm (hν = 5.83 eV) laser pulse (circa 200 ps pulse duration, 20 kHz repetition rate) that impinged normal upon the CuO/vacuum interface. Photoelectrons with a kinetic energy of up to ~ 1 eV were extracted parallel to the surface normal of the CuO sample, bent around electrostatically by 90°, and accelerated with 50 kV towards the target in a Mott scattering apparatus. Two detectors at ± 120° scattering angle from the incident electron beam direction register the scattering intensity. The asymmetry in the detectors' count rates is analyzed to provide the average longitudinal spin polarization of the electrons; see supplementary section S3. In this way the longitudinal spin polarization of the electrons ejected from the sample is determined. A polycrystalline Au sample, which was mounted right beneath the CuO sample on the sample manipulator, was used as a reference. When excited by linearly polarized light, the intensities from this reference measured by the Mott detectors are taken to determine the instrumental asymmetries and thus calibrate zero spin polarization. A quarter wave plate was used to generate either clockwise (cw), counter clockwise (ccw), or linearly polarized light. For each experimental run, this quarter wave plate was rotated once about 360°, then the reference sample was moved into the measurement position to determine the asymmetry corresponding to zero spin polarization.

For each experimental run about 10^6 laser pulses were applied which resulted in one spin polarization determination. All measurement results are plotted as a histogram; see the Supplemental Information, Fig S8. A Gaussian fit to the histogram distribution yields the average

spin polarization with its FWHM denoted as the error. It should be noted that before and after the measurements of one sample, the spin polarization from a clean Au(111) sample was measured, yielding spin polarizations of about +25 % and -25% for ccw and cw polarized light, respectively. Only when the same spin polarization was measured for the Au(111) with circular polarized excitation, both before and after the CuO measurement, were the results for the CuO sample taken as valid.

3.2.3 Electrochemical Measurements

Electrochemical studies were carried out for chiral and achiral CuO-coated anodes in 0.1 M Na_2SO_4 solution (pH 6.5) and 0.2 M borate buffer solution (pH 9) using a Pt wire as the counter electrode and Ag/AgCl (in 3 M NaCl) as the reference electrode in the dark and under illumination. The measurements were done using linear sweep voltammetry in the potential range from −0.2 to 1.5 V vs Ag/AgCl (3 M NaCl) with a scan rate of 20 mV/s in the dark. An 8 W white light LED lamp was used for the illumination. The rate of hydrogen production using chiral and achiral CuO anodes was measured in 0.1 M Na_2SO_4 at a constant potential of 1.2 V vs Ag/AgCl (3 M NaCl) reference electrode in the dark. We also studied an electrochemical cell with chiral (and achiral) CuO-coated cathodes and anodes and compared their performance in the dark to that under irradiation.

3.3 Results and Discussion

3.3.1 Characterization of CuO films

Figure 1A shows an optical absorbance spectrum for a 50 nm thick CuO film grown from an L-tartrate:Cu^{2+} solution on a 20 nm Au substrate. The direct and indirect band gaps of the CuO film were extracted from Tauc plots of the absorbance spectrum and are found to be 2.84 and 1.25 eV respectively (see Figure S3).[37] The indirect gap is consistent with literature reports, and the higher energy, direct band gap is consistent with literature reports for a polycrystalline bulk CuO band gap[38-49] with some quantum confinement shift.[50-52]

The circular dichroism (CD) spectra of two 50 nm CuO films, electrodeposited from L-tartrate:Cu^{2+} (L-CuO) and from D-tartrate:Cu^{2+} (D-CuO) onto Au films, are shown in Figure 1B. The peak at 400 nm in the CD spectrum is close to the energy of the direct band gap. The CD spectra display an approximate mirror symmetry for the CuO films, which are grown from aqueous solutions of different Cu-tartrate chirality, and indicate that the chirality of the two CuO films are opposite. Note that the measurement is for two separately prepared films for which small differences in thickness and/or morphology can cause deviations from perfect mirror symmetry. Meso-tartrate:Cu^{2+} complexes do not possess a net average chirality because the meso-tartrate has

two opposite chiral centers; in this case, an achiral film is electrodeposited on the substrate (the purple curve in Figure 1B).

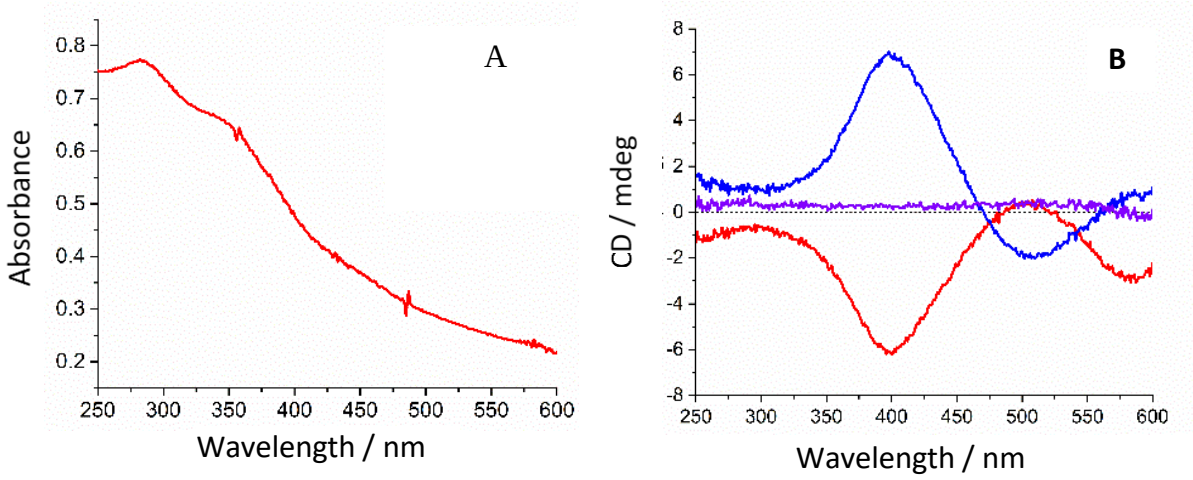

Figure 3-2. Panel A shows a UV-visible spectrum of a 50 nm thick L-CuO film with the UV-visible spectrum of a 20 nm Au substrate subtracted. Panel B shows circular dichroism (CD) spectra of 50 nm L-CuO film (red), D-CuO films (blue), and a meso-CuO film (purple). Note the approximate mirror symmetry of the L-CuO and D-CuO films, and the zero CD for the achiral meso-CuO.

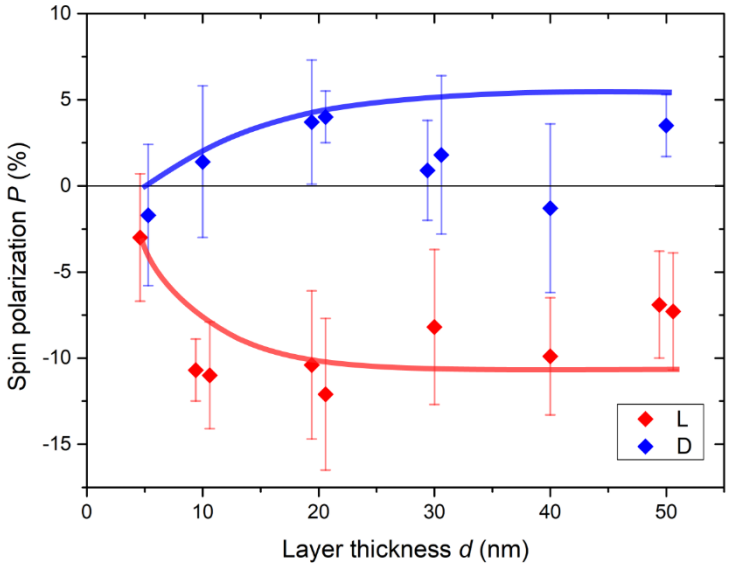

Figure 3-1. The plot shows the spin polarization P of photoelectrons from the Au/CuO films as a function of the CuO film thickness d and its chirality. The red diamonds are the L-CuO formed from L-tartrate:Cu^{2+} solutions and the blue diamonds are the D-CuO formed from the D-tartrate:Cu^{2+} solutions.

3.3.2 Photoemission Studies

Figure 2 shows a plot of the spin polarization measured as a function of the chiral CuO film thickness in different trials and with different samples for each nominal thickness. The spin polarization, which is defined as $P = (N_u-N_d)/(N_u+N_d) \times 100\%$, is found to change sign as the chirality of the CuO film is changed; $N_u(N_d)$ is the average number of electrons measured that correspond to spin up (down). The polarization has a negative value for the L-CuO film and, on average, has a positive value for the D-CuO. The spin polarization obtained from the L-CuO films has a significantly higher absolute value than that obtained with the D-CuO films.

For films with thicknesses below 20 nm, the spin polarization increases with the film thickness; and for films thicker than 20 nm, the spin polarization remains relatively constant with increase of the film thickness up to about 50 nm.

3.3.3 Electrolysis Studies

Electrolysis studies were performed for CuO anodes that ranged in thickness from 10 nm to a few micrometers in thickness, both on Au substrates and on TiO2substrates. In each case the chirality of the CuO was confirmed by circular dichroism spectroscopy. The spin filtering studies described above imply that the charge transfer from solution species (and adsorbates) is spin selective for at least the first 50nm of the CuO film.

Current-Voltage Behavior. Linear sweep voltammetry was used to examine the oxygen evolution reaction (OER) for 10 nm thick and 500 nm thick CuO electrodes on Au at pH 9.5. The current-voltage curves in Figure 3A display a clear enhancement of the OER rate when a 10 nm CuO film is present (onset potentials between 1.20 and 1.28 V versus NHE), as compared to the

case of bare Au (onset potential of 1.4 to 1.5 V versus NHE) which is the black trace. The CuO onset potential range represents a 350 mV to 450 mV overpotential for the pH 9.5 solutions used here; see the Supporting Information for details on overpotential calculation.

The inset of Figure 3A shows an expanded current scale (0 to 1 mA/cm^2) and reveals small pre-peaks that are observed before the full onset of OER by the electrode. Following previous literature, these peaks are tentatively assigned to the presence of highly active impurities ions from the electrolyte, e.g., Fe ions,[53] and/or highly active Au oxides on the surface.[54] Figure 3B shows current-voltage curves for 500 nm CuO films, in which the chiral electrodes (red and blue) have a higher current density than the achiral CuO film (green curve).

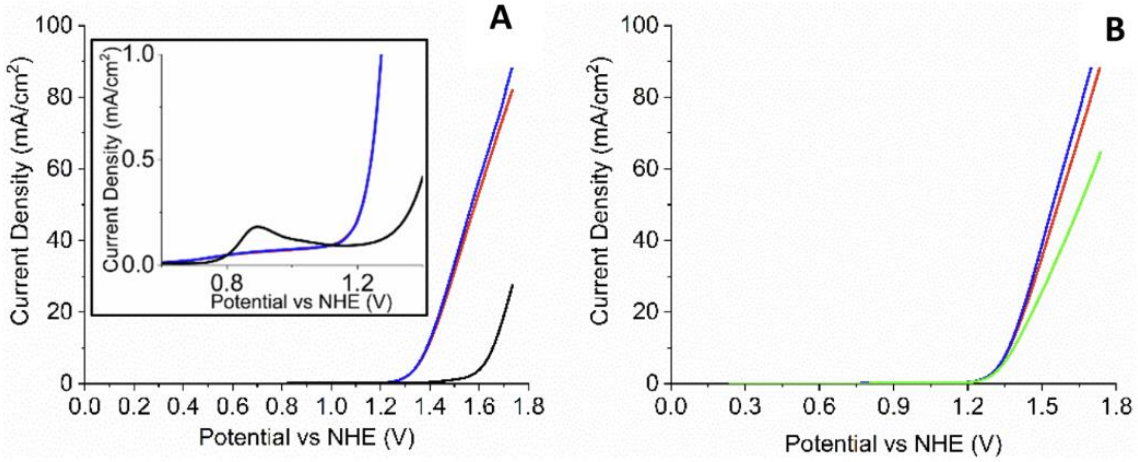

Figure 3-3. (A) Linear sweep voltammograms for 50 nm thick L-CuO (red) film electrodes, 50 nm thick D-CuO (blue) film electrodes, and bare Au (black) electrodes. The inset provides a zoomed-in view of the data and reveals a current prepeak which has been associated with a small percentage of highly active catalytic sites (see text). The potential is reported versus NHE, and the current density is given in mA/cm^2. (B) 500 nm thick films for which the onset potential shifts to larger values. The glycine-CuO films (shown in light green) are achiral and display less electrocatalytic activity than the chiral CuO films.

Plots of the overpotential versus the logarithm of the current (Tafel plots) provide information about the electrochemical exchange current and the reaction mechanism.[55, 56] For 400 mV to 600 mV overpotentials the slope is 70 to 80 mV/decade; these values are similar to those reported for achiral CuO electrocatalysis.[14, 57-59] Tafel plots and more discussion for the data in

Figure 3 are shown in the Supplemental Information (Figures S11 and S12). The remainder of the work focuses on thicker CuO films.

Chiral CuO layers of ~3 μm thickness were electrodeposited on TiO_2 (~1 μm) coated FTO glass, using L-tartaric acid as the chiral bias and meso-tartaric acid as the achiral control; see section S2 of the Supporting Information for more details. Figure 4A shows plots of the current density vs. applied voltage that were obtained using the electrochemically deposited chiral and achiral CuO coated anodes in 0.1 M pH 9 aqueous buffer solution in the dark. As shown in Figure 4A, the onset potential of achiral CuO (black line) is obviously higher than that of chiral CuO (red line), supporting the earlier inference that spin filtering at the solution/CuO interface is enough for the spin enhancement effect to manifest.

3.3.4 Hydrogen evolution and Peroxide suppression

The rate of hydrogen production was used to assess the overall water-splitting efficiency; note that the number of H_2 mols produced is the sum of one mol of H_2 for each mol of H_2O_2 produced and two mol of H_2 for each mol of O_2 produced. The total yield of H_2 was measured for chiral and achiral electrocatalysts at a constant voltage of 1.4 V vs NHE (Figure 4B). The current of the chiral anode was about 1.4 mA/cm^2 at 1.4 V potential (NHE), whereas that of the achiral anode was about 0.7 mA/cm^2 at 1.4 V potential (NHE). Although the current differs by a factor of~2, the H_2 yield data show that the chiral anode(red points, 187 nL/s) produces~8 times more H_2 than the achiral anode (black points, 23.5 nL/s), indicating that the chiral electrode produces about 4 times more H_2 per mA of current than does the achiral electrode when the applied potential

was 1.4V (NHE). As the H_2 production occurs on the Pt cathode in both cases, the chiral anode must produce a larger percentage of O_2 (as compared to H_2O_2) than does the achiral electrode.

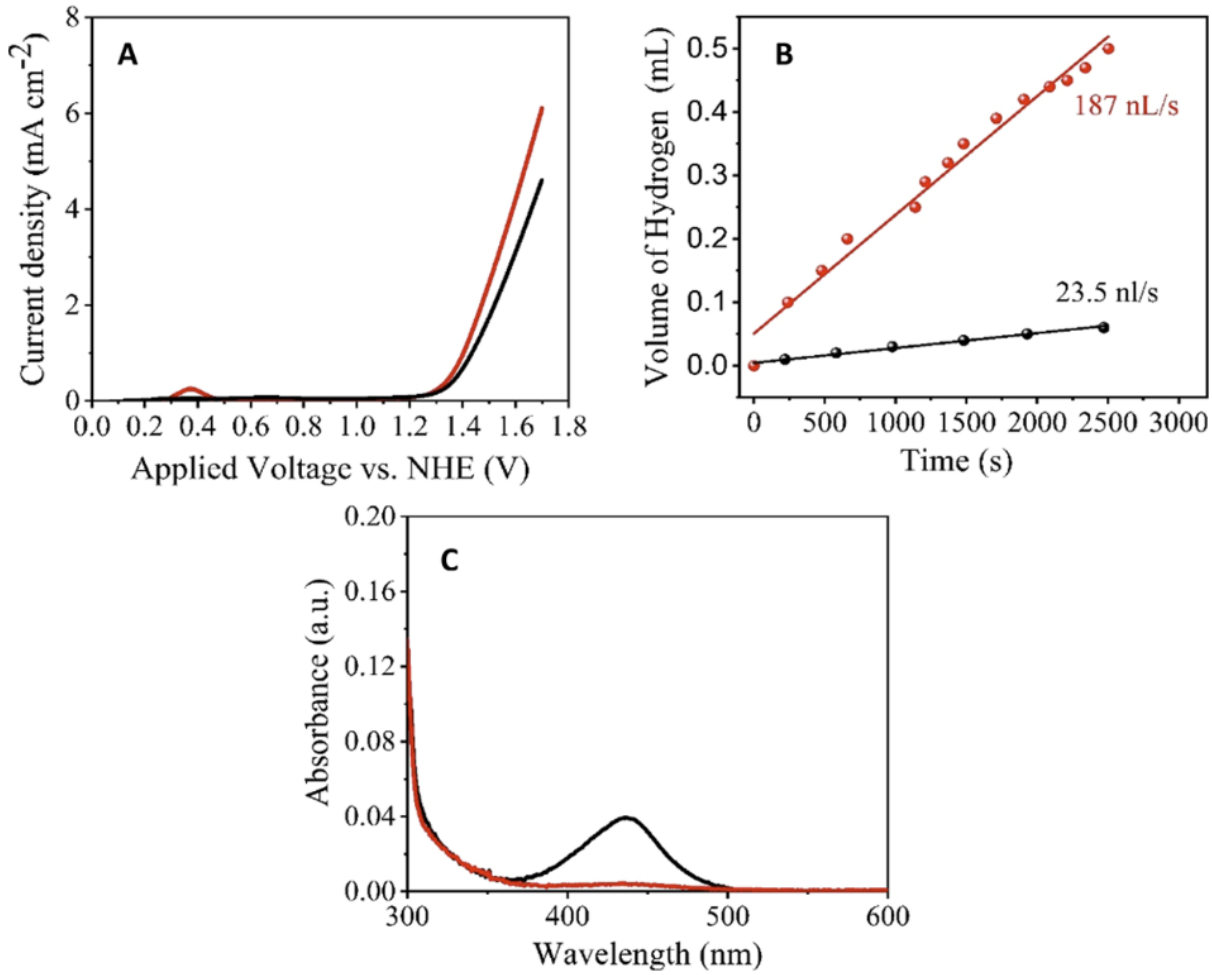

Figure 3-4. (A) Linear sweep voltammetry curves for electrochemically deposited chiral CuO (induced by L-tartaric acid, red line) and achiral CuO (induced by meso-tartaric acid, black line) electrodes in a pH 9 aqueous buffer solution in dark conditions. (B) Rate of hydrogen production measured using electrochemically deposited CuO at constant potential 1.4 V vs NHE (red for chiral CuO and black for achiral CuO). (C) H_2O_2 detection. UV−vis absorption spectra (red line for chiral CuO and black line for achiral CuO) of the used 0.1 M Na_2SO_4 electrolyte after the titration with o-tolidine. The electrochemical measurement is done by keeping the anode at a constant potential of 1.7 V versus NHE for 40 min in the dark.

The selectivity for the production of O_2 by the chiral electrode was corroborated by measuring the H_2O_2 yield during electrolysis. To detect the production of hydrogen peroxide, we employed o-tolidine as an indicator.[60, 61] Figure 4c shows the ultraviolet (UV) −visible absorption spectra obtained after titration with o-tolidine when the solution used as the electrolyte in the electrolysis cell was 0.1 M Na_2SO_4, pH 6.5. The titrations were performed after keeping the chiral

and achiral CuO anode of the electrochemical cell ata constant voltage of 1.7 V vs NHE for 40 min in the dark. The cell with an achiral CuO anode shows an absorbance peak at 436 nm which indicates the production of H_2O_2 during wateroxidation. For the chiral CuO anodes, the peroxide signal is 13 times weaker, for the same reaction time and conditions. Together these data explain how the current densities (Figure 4A) can differ by a factor of only about two but the hydrogen yields (Figure 4B) can differ by eight times; namely, a significant amount of the current in the achiral electrodesgenerates hydrogen peroxide rather than oxygen.

Comparing Chirality effect for CuO anode and CuO cathode. Replacing the Pt cathode, used for the data in Figure 4, with a CuO cathode decreases the overall cell performance by reducing the efficiency of the cathodic reaction, hydrogen evolution reaction; however, it allows

us to ascertain whether there is a chirality effect when the kinetics of the oxygen evolution reaction and the hydrogen evolution reaction are comparable.

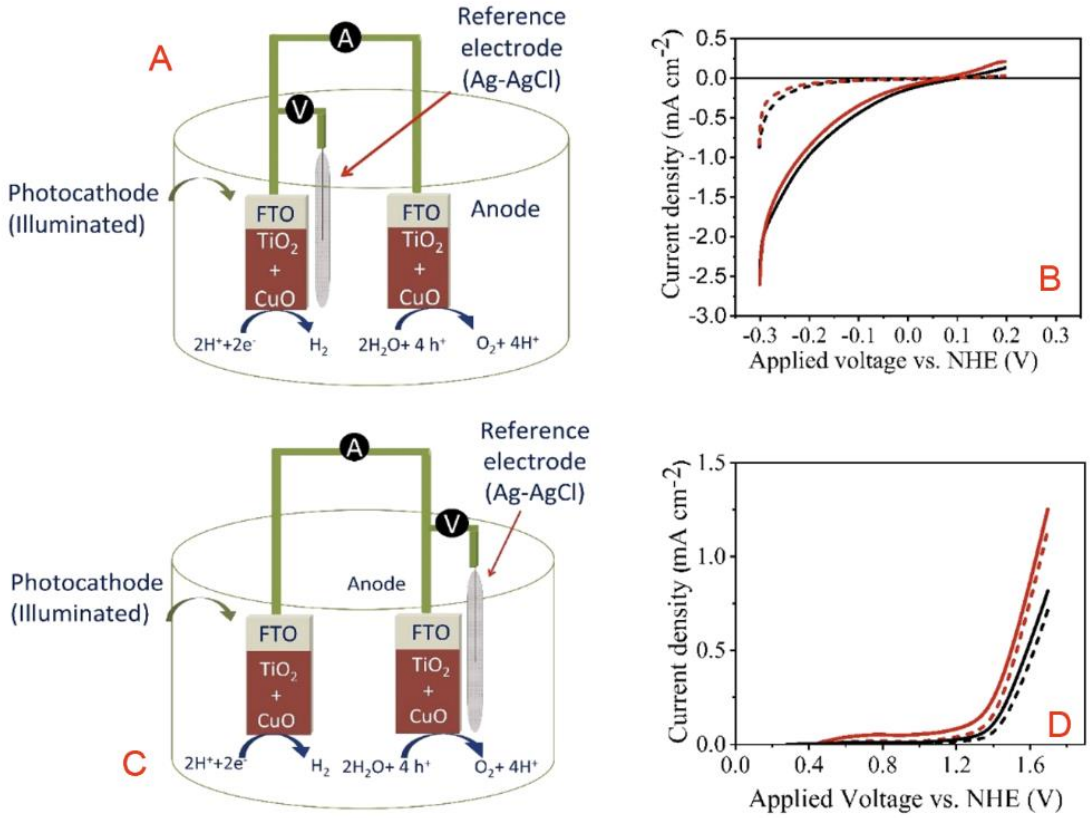

Figure 3-5. Schematic of the electrochemical setup for the case where electrochemically deposited CuO is used as both cathode and anode. The results with the cell containing chiral CuO are presented in red, while those with achiral CuO are in black. The dotted lines represent the measurements carried out in the dark, and the solid line represents measurements carried out in the light. The current density versus applied potential is shown in panel B for the case where the bias is applied to the cathode (wiring diagram in panel A) and in panel D for the case where the bias is applied to the anode (wiring diagram in panel C). Electrochemical measurements were performed using 0.1 M Na_2SO_4 solution with pH 6.5. The scan is performed up to 1.5 V vs Ag/AgCl (3 M NaCl) with a scan rate of 20 mV/s in the dark. E(NHE) = E(vs Ag/AgCl) + E°(Ag/AgCl), where E°(Ag/AgCl, 3 M NaCl) = 0.195 V.

Figure 5 summarizes the current-voltage behavior of an electrochemical cell, in which both the anode and the cathode comprise CuO electrodes, both in the dark and under illumination. Figure 5A shows the electrical set-up used to apply a negative voltage on the cathode, relative to the anode.

Figure 5B shows the current density versus applied voltage that was measured in this arrangement for both chiral (red curves)and achiral (black curves) CuO-coated cathodes. The data in Figure 5B display a pronounced photocurrent, and the current density for the chiral electrodes is somewhat smaller than for the achiral electrodes. The significant photocurrent is consistent with a forward bias band structure postulated for metal−copper oxide interfaces.[62] In addition, the somewhat larger negative current density for the achiral cathodes is consistent with the generation of a statistical mixture of spin orientations. Given that H_2 (a singlet) is generated on the cathode, preservation of the spin orientation of adsorbed H atoms should inhibit product formation. The small effect observed here suggests that the reaction rate is only weakly affected by these spin constraints; other processes (e.g., generation of adsorbed H atoms from the "neutral" solution)affect the rate more.

Figure 5C shows the electrical setup used to apply a positive voltage on the anode, and Figure 5D shows the measured current−voltage curves. In this case, the cell with the chiral CuO produces a higher current density than the cell with achiral electrodes, and the photocurrent is small. The small value for the photocurrent is consistent with a placement of the CuO valence band edge near the conduction band edge of the TiO_2. The chirality effect is consistent with the production of spin-polarized OH radicals which facilitate the production of triplet oxygen, over singlet oxygen and hydrogen peroxide. The onset potentials for oxygen production are calculated (see Figure S10 for details) to be 1.38 and 1.35 V for chiral CuO in the dark and light and 1.43 and 1.39 V for the achiral CuO in the dark and in the light, respectively. The chiral CuO-coated anode

displays a higher current density and a somewhat lower threshold potential for water splitting, as compared to the achiral electrode.

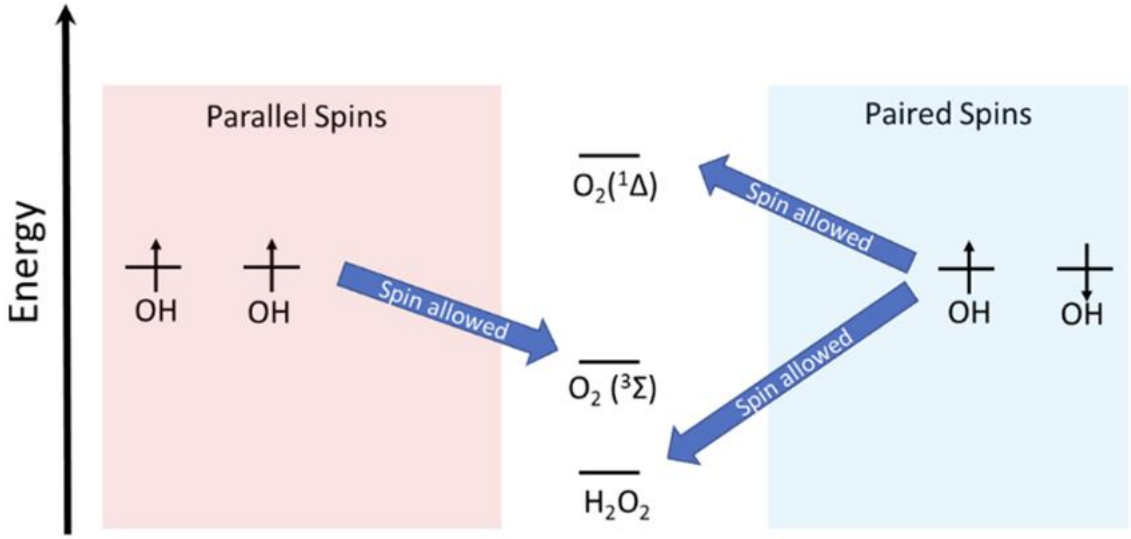

Figure 3-6. Energy diagram illustrating the possible reaction products from the combination of hydroxyl groups on the CuO surface. The spin restriction on the recombination leads to selectivity against H_2O_2 formation if the OH radical spins are aligned.

Others have examined the OER on achiral CuO electrodes, and recent studies find overpotentials in the 300−400 mV range, for pH 9.[57, 59, 63] The OER is strongly dependent on the solution pH, and hydrogen peroxide can be a significant side-product in this reaction. The generation of H_2O_2 demonstrated in this study was attributed to the use of an achiral electrode (see Figure 4C). In contrast, anodes comprising chiral CuO films inhibit the formation of H_2O_2 and maintain low overpotentials. Figure 6 shows an energy scheme that rationalizes a mechanism assuming the combination of surface adsorbed OH to explain how the selectivity occurs. When the surface OH species are spin parallel, they can combine and produce a triplet state product, the O_2 ground electronic state; however, if they have their spins antiparallel, they can combine to form either H_2O_2 or the O_2 first excited state, which is a singlet. Because of the CISS effect, the charge transfer at the CuO surface generates a spin polarization (preference for aligned spins), and this enhances the production of the triplet product, as compared to the possible singlet products. While

the rationale is given here for a mechanism involving their combination of adsorbed OH intermediates, the rationale should be applied to other mechanisms, such as the oxide path and the metal peroxide path.[64] The selectivity for oxygen production is like that found in earlier work with chiral molecules,[27-29] but this study uses an all-inorganic system (CuO) and generates a current density more than 103 times higher than that observed with organic molecule-coated electrodes (mA/cm^2 versus $\mu A/cm^2$).

This work demonstrates that chiral CuO films act as electron spin filters and can be used as selective electrocatalysts in the oxygen evolution reaction. Chiral CuO films were electro-deposited on an Au substrate, and their spin-filtering properties were demonstrated by Mott polarimetry measurements for a range of CuO thicknesses. Chiral CuO films were grown on both Au and FTO/TiO_2 electrodes, and they were used in electrolysis studies of water. Because of the electron spin dependence for the oxygen evolution reaction and the generation of spin-polarized reaction intermediates, the chiral CuO anodes enable selective production of O_2 over that of H_2O_2. While CuO is used in this study, it should not be considered unique; other chiral metal oxides should display analogous properties. This work demonstrates that chiral electrocatalysts offer a new approach for realizing selectivity in electrochemical transformations, and it should be synergistic with other electrocatalysis strategies.[15]

3.4 Acknowledgements

D.H.W. acknowledges support from United States National Science Foundation Grant CHE-1464701. R.N. acknowledges funding from the European Research Council (ERC) under European Union's Seventh Framework Program FP7/2007-2013/ERC Grant 338720 CISS (chiral-

induced spin selectivity). R.N. and H.Z. are grateful for partial funding by the Volkswagen Foundation via grants 93454 and 93451, respectively.

3.5 Reference

1.Ray, K.; Ananthavel, S. P.; Waldeck, D. H.; Naaman, R., Asymmetric Scattering of Polarized Electrons by Organized Organic Films of Chiral Molecules. *Science* **1999,** *283* (5403), 814-816.

2.Naaman, R.; Waldeck, D. H., Spintronics and Chirality: Spin Selectivity in Electron Transport Through Chiral Molecules. *Annu. Rev. Phys. Chem.* **2015,** *66* (1), 263-281.

3.Naaman, R.; Waldeck, D. H., Chiral-Induced Spin Selectivity Effect. *The Journal of Physical Chemistry Letters* **2012,** *3* (16), 2178-2187.

4.Medina, E.; González-Arraga, L. A.; Finkelstein-Shapiro, D.; Berche, B.; Mujica, V., Continuum model for chiral induced spin selectivity in helical molecules. *The Journal of Chemical Physics* **2015,** *142* (19), 194308.

5.Michaeli, K.; Kantor-Uriel, N.; Naaman, R.; Waldeck, D. H., The electron's spin and molecular chirality – how are they related and how do they affect life processes? *Chemical Society Reviews* **2016,** *45* (23), 6478-6487.

6.Michaeli, K.; Varade, V.; Naaman, R.; Waldeck, D. H., A new approach towards spintronics–spintronics with no magnets. *Journal of Physics: Condensed Matter* **2017,** *29* (10), 103002.

7.Göhler, B.; Hamelbeck, V.; Markus, T. Z.; Kettner, M.; Hanne, G. F.; Vager, Z.; Naaman, R.; Zacharias, H., Spin Selectivity in Electron Transmission Through Self-Assembled Monolayers of Double-Stranded DNA. *Science* **2011,** *331* (6019), 894-897.

8.Mishra, D.; Markus, T. Z.; Naaman, R.; Kettner, M.; Göhler, B.; Zacharias, H.; Friedman, N.; Sheves, M.; Fontanesi, C., Spin-dependent electron transmission through bacteriorhodopsin embedded in purple membrane. *Proceedings of the National Academy of Sciences* **2013,** *110* (37), 14872-14876.

9.Kettner, M.; Göhler, B.; Zacharias, H.; Mishra, D.; Kiran, V.; Naaman, R.; Waldeck, D. H.; Sęk, S.; Pawłowski, J.; Juhaniewicz, J., Spin Filtering in Electron Transport Through Chiral Oligopeptides. *The Journal of Physical Chemistry C* **2015,** *119* (26), 14542-14547.

10.Kettner, M.; Maslyuk, V. V.; Nürenberg, D.; Seibel, J.; Gutierrez, R.; Cuniberti, G.; Ernst, K.-H.; Zacharias, H., Chirality-Dependent Electron Spin Filtering by Molecular Monolayers of Helicenes. *J Phys Chem Lett* **2018,** *9* (8), 2025-2030.

11.Kettner, M.; Bhowmick, D. K.; Bartsch, M.; Göhler, B.; Zacharias, H., A Silicon-Based Room Temperature Spin Source without Magnetic Layers. *Advanced Materials Interfaces* **2016,** *3* (20), 1600595.

12.Tahir, M.; Pan, L.; Idrees, F.; Zhang, X.; Wang, L.; Zou, J.-J.; Wang, Z. L., Electrocatalytic oxygen evolution reaction for energy conversion and storage: A comprehensive review. *Nano Energy* **2017,** *37*, 136-157.

13.Xia, Z., Hydrogen evolution: Guiding principles. *Nature Energy* **2016,** *1* (10), 16155.

14.Liu, X.; Cui, S.; Sun, Z.; Ren, Y.; Zhang, X.; Du, P., Self-Supported Copper Oxide Electrocatalyst for Water Oxidation at Low Overpotential and Confirmation of Its Robustness by Cu K-Edge X-ray Absorption Spectroscopy. *The Journal of Physical Chemistry C* **2016,** *120* (2), 831-840.

15.Siahrostami, S.; Li, G.-L.; Viswanathan, V.; Nørskov, J. K., One- or Two-Electron Water Oxidation, Hydroxyl Radical, or H2O2 Evolution. *The Journal of Physical Chemistry Letters* **2017,** *8* (6), 1157-1160.

16.Hisatomi, T.; Kubota, J.; Domen, K., Recent advances in semiconductors for photocatalytic and photoelectrochemical water splitting. *Chemical Society Reviews* **2014,** *43* (22), 7520-7535.

17.Roger, I.; Shipman, M. A.; Symes, M. D., Earth-abundant catalysts for electrochemical and photoelectrochemical water splitting. *Nature Reviews Chemistry* **2017,** *1* (1), 0003.

18.Anantharaj, S.; Ede, S. R.; Sakthikumar, K.; Karthick, K.; Mishra, S.; Kundu, S., Recent Trends and Perspectives in Electrochemical Water Splitting with an Emphasis on Sulfide, Selenide, and Phosphide Catalysts of Fe, Co, and Ni: A Review. *ACS Catalysis* **2016,** *6* (12), 8069-8097.

19.Martin, D. J.; Reardon, P. J. T.; Moniz, S. J. A.; Tang, J., Visible Light-Driven Pure Water Splitting by a Nature-Inspired Organic Semiconductor-Based System. *Journal of the American Chemical Society* **2014,** *136* (36), 12568-12571.

20.Zhang, Z.; Long, J.; Yang, L.; Chen, W.; Dai, W.; Fu, X.; Wang, X., Organic semiconductor for artificial photosynthesis: water splitting into hydrogen by a bioinspired C3N3S3polymer under visible light irradiation. *Chemical Science* **2011,** *2* (9), 1826-1830.

21.Arango, A. C.; Johnson, L. R.; Bliznyuk, V. N.; Schlesinger, Z.; Carter, S. A.; Hörhold, H. H., Efficient Titanium Oxide/Conjugated Polymer Photovoltaics for Solar Energy Conversion. *Advanced Materials* **2000,** *12* (22), 1689-1692.

22.Chrétien, S.; Metiu, H., O2 evolution on a clean partially reduced rutile TiO2(110) surface and on the same surface precovered with Au1 and Au2: The importance of spin conservation. *The Journal of Chemical Physics* **2008,** *129* (7), 074705.

23.Nazmutdinov, R. R.; Santos, E.; Schmickler, W., Spin effects in oxygen electrocatalysis: A discussion. *Electrochemistry Communications* **2013,** *33*, 14-17.

24.Gracia, J., Spin dependent interactions catalyse the oxygen electrochemistry. *Physical Chemistry Chemical Physics* **2017,** *19* (31), 20451-20456.

25.Torun, E.; Fang, C. M.; de Wijs, G. A.; de Groot, R. A., Role of Magnetism in Catalysis: RuO2 (110) Surface. *The Journal of Physical Chemistry C* **2013,** *117* (12), 6353-6357.

26.Yang, W.; Yu, Y.; Starr, M. B.; Yin, X.; Li, Z.; Kvit, A.; Wang, S.; Zhao, P.; Wang, X., Ferroelectric Polarization-Enhanced Photoelectrochemical Water Splitting in TiO2–BaTiO3 Core–Shell Nanowire Photoanodes. *Nano Letters* **2015,** *15* (11), 7574-7580.

27.Mtangi, W.; Tassinari, F.; Vankayala, K.; Vargas Jentzsch, A.; Adelizzi, B.; Palmans, A. R. A.; Fontanesi, C.; Meijer, E. W.; Naaman, R., Control of Electrons' Spin Eliminates Hydrogen Peroxide Formation During Water Splitting. *J Am Chem Soc* **2017,** *139* (7), 2794-2798.

28.Mtangi, W.; Kiran, V.; Fontanesi, C.; Naaman, R., Role of the Electron Spin Polarization in Water Splitting. *J Phys Chem Lett* **2015,** *6* (24), 4916-4922.

29.Tassinari, F.; Banerjee-Ghosh, K.; Parenti, F.; Vankayala, K.; Mucci, A.; Naaman, R., Enhanced Hydrogen Production With Chiral Conductive Polymer-Based Electrodes. *J Phys Chem A* **2017**.

30.Zhang, W.; Banerjee-Ghosh, K.; Tassinari, F.; Naaman, R., Enhanced Electrochemical Water Splitting with Chiral Molecule-Coated Fe3O4 Nanoparticles. *ACS Energy Letters* **2018,** *3* (10), 2308-2313.

31.Deng, Y.; Handoko, A. D.; Du, Y.; Xi, S.; Yeo, B. S., In Situ Raman Spectroscopy of Copper and Copper Oxide Surfaces during Electrochemical Oxygen Evolution Reaction: Identification of CuIII Oxides as Catalytically Active Species. *ACS Catalysis* **2016,** *6* (4), 2473-2481.

32.Shi, Y.; Gimbert-Suriñach, C.; Han, T.; Berardi, S.; Lanza, M.; Llobet, A., CuO-Functionalized Silicon Photoanodes for Photoelectrochemical Water Splitting Devices. *ACS Applied Materials & Interfaces* **2016,** *8* (1), 696-702.

33.de Brito, J. F.; Tavella, F.; Genovese, C.; Ampelli, C.; Zanoni, M. V. B.; Centi, G.; Perathoner, S., Role of CuO in the modification of the photocatalytic water splitting behavior of TiO2 nanotube thin films. *Applied Catalysis B: Environmental* **2018,** *224*, 136-145.

34.Walter, M. G.; Warren, E. L.; McKone, J. R.; Boettcher, S. W.; Mi, Q.; Santori, E. A.; Lewis, N. S., Solar Water Splitting Cells. *Chemical Reviews* **2010,** *110* (11), 6446-6473.

35.Kothari, H. M.; Kulp, E. A.; Boonsalee, S.; Nikiforov, M. P.; Bohannan, E. W.; Poizot, P.; Nakanishi, S.; Switzer, J. A., Enantiospecific Electrodeposition of Chiral CuO Films from Copper(II) Complexes of Tartaric and Amino Acids on Single-Crystal Au(001). *Chemistry of Materials* **2004,** *16*, 4232-4244.

36.Widmer, R.; Haug, F.-J.; Ruffieux, P.; Gröning, O.; Bielmann, M.; Gröning, P.; Fasel, R., Surface Chirality of CuO Thin Films. *J. Am. Chem. Soc.* **2006,** *128* (43), 14103-14108.

37.Pankove, J. I., *Optical Processes in Semiconductors*. Dover: 1975.

38.Dhineshbabu, N. R.; Rajendran, V.; Nithyavathy, N.; Vetumperumal, R., Study of structural and optical properties of cupric oxide nanoparticles. *Applied Nanoscience* **2016,** *6* (6), 933-939.

39.Wang, D.; Song, C.; Lv, X.; Wang, Y., Design of preparation parameters for commendable photocatalytic properties in CuO nanostructures. *Applied Physics A* **2016,** *122* (12), 1020.

40.Erdoğan, İ. Y.; Güllü, Ö., Optical and structural properties of CuO nanofilm: Its diode application. *Journal of Alloys and Compounds* **2010,** *492* (1), 378-383.

41.Liu, Q.; Liu, H.; Liang, Y.; Xu, Z.; Yin, G., Large-scale synthesis of single-crystalline CuO nanoplatelets by a hydrothermal process. *Materials Research Bulletin* **2006,** *41* (4), 697-702.

42.Han, X.; Liao, F.; Zhang, Y.; Xu, C.; Chen, H., Dendrite-like cupric oxide microstructures prepared via a facile SDBS-assisted hydrothermal route. *Journal of Materials Science: Materials in Electronics* **2018,** *29* (4), 3178-3181.

43.Jiang, T.; Wang, Y.; Meng, D.; Wu, X.; Wang, J.; Chen, J., Controllable fabrication of CuO nanostructure by hydrothermal method and its properties. *Applied Surface Science* **2014,** *311*, 602-608.

44.Zhang, X.; Zhang, D.; Ni, X.; Zheng, H., Optical and electrochemical properties of nanosized CuO via thermal decomposition of copper oxalate. *Solid-State Electronics* **2008,** *52* (2), 245-248.

45.Morasch, J.; Wardenga, H. F.; Jaegermann, W.; Klein, A., Influence of grain boundaries and interfaces on the electronic structure of polycrystalline CuO thin films. *physica status solidi (a)* **2016,** *213* (6), 1615-1624.

46.Gaur, U. K.; Kumar, A.; Varma, G. D., The synthesis of self-assembled polycrystalline 1-D CuO nanostructures in aqueous medium and a study of their multifunctional features. *CrystEngComm* **2014,** *16* (14), 3005-3014.

47.Das, S.; Alford, T. L., Structural and optical properties of Ag-doped copper oxide thin films on polyethylene napthalate substrate prepared by low temperature microwave annealing. *Journal of Applied Physics* **2013,** *113* (24), 244905.

48.Izaki, M.; Nagai, M.; Maeda, K.; Mohamad, F.; Motomura, K.; Sasano, J.; Shinagawa, T.; Watase, S., Electrodeposition of 1.4-eV-Bandgap p-Copper (II) Oxide Film With Excellent Photoactivity. *Journal of The Electrochemical Society* **2011,** *158*, D578-D584.

49.Koffyberg, F. P.; Benko, F. A., A photoelectrochemical determination of the position of the conduction and valence band edges of p ‐ type CuO. *Journal of Applied Physics* **1982,** *53* (2), 1173-1177.

50.Maji, S. K.; Mukherjee, N.; Mondal, A.; Adhikary, B.; Karmakar, B., Chemical synthesis of mesoporous CuO from a single precursor: Structural, optical and electrical properties. *Journal of Solid State Chemistry* **2010,** *183* (8), 1900-1904.

51.Pappas, S. D.; Poulopoulos, P.; Kapaklis, V.; Grammatikopoulos, S.; Trachylis, D.; Velgakis, M. J.; Meletis, E. I.; Politis, C., Growth and Experimental Evidence of Quantum Confinement Effects in Cu2O and CuO Thin Films. *Journal of Nano Research* **2011,** *15*, 69-74.

52.Borgohain, K.; Mahamuni, S., Formation of Single-phase CuO Quantum Particles. *Journal of Materials Research* **2002,** *17* (5), 1220-1223.

53.Klaus, S.; Trotochaud, L.; Cheng, M.-J.; Head-Gordon, M.; Bell, A. T., Experimental and Computational Evidence of Highly Active Fe Impurity Sites on the Surface of Oxidized Au for the Electrocatalytic Oxidation of Water in Basic Media. *ChemElectroChem* **2016,** *3* (1), 66-73.

54.Doyle, R. L.; Lyons, M. E. G., The mechanism of oxygen evolution at superactivated gold electrodes in aqueous alkaline solution. *Journal of Solid State Electrochemistry* **2014,** *18* (12), 3271-3286.

55.Shinagawa, T.; Garcia-Esparza, A. T.; Takanabe, K., Insight on Tafel slopes from a microkinetic analysis of aqueous electrocatalysis for energy conversion. *Scientific Reports* **2015,** *5* (1), 13801.

56.Fang, Y.-H.; Liu, Z., Tafel Kinetics of Electrocatalytic Reactions: From Experiment to First-Principles. *ACS Catalysis* **2014,** *4*, 4364-4376.

57.Chen, H.; Gao, Y.; Lu, Z.; Ye, L.; Sun, L., Copper Oxide Film In-situ Electrodeposited from Cu(II) Complex as Highly Efficient Catalyst for Water Oxidation. *Electrochimica Acta* **2017,** *230*, 501-507.

58.Liu, X.; Jia, H.; Sun, Z.; Chen, H.; Xu, P.; Du, P., Nanostructured copper oxide electrodeposited from copper(II) complexes as an active catalyst for electrocatalytic oxygen evolution reaction. *Electrochemistry Communications* **2014,** *46*, 1-4.

59.Yu, F.; Li, F.; Zhang, B.; Li, H.; Sun, L., Efficient Electrocatalytic Water Oxidation by a Copper Oxide Thin Film in Borate Buffer. *ACS Catalysis* **2015,** *5* (2), 627-630.

60.Li, Z.; Kong, C.; Lu, G., Visible Photocatalytic Water Splitting and Photocatalytic Two-Electron Oxygen Formation over Cu- and Fe-Doped g-C3N4. *The Journal of Physical Chemistry C* **2016,** *120* (1), 56-63.

61.Gu, B.; Kiwi, J.; Grätzel, M., PHOTOCHEMICAL WATER CLEAVAGE IN SUSPENSIONS OF Pt-LOADED TITANIA PARTICLES WITH 0.7% OVERALL LIGHT TO CHEMICAL CONVERSION EFFICIENCY. In *Hydrogen Systems*, Veziroglu, T. N.; Yajie, Z. H. U.; Deyou, B. A. O., Eds. Pergamon: 1986; pp 121-134.

62.Zhang, Z.; Wang, P., Highly stable copper oxide composite as an effective photocathode for water splitting via a facile electrochemical synthesis strategy. *Journal of Materials Chemistry* **2012,** *22* (6), 2456-2464.

63.Liu, X.; Zheng, H.; Sun, Z.; Han, A.; Du, P., Earth-Abundant Copper-Based Bifunctional Electrocatalyst for Both Catalytic Hydrogen Production and Water Oxidation. *ACS Catalysis* **2015,** *5* (3), 1530-1538.

64.Bockris, J. O. M., Kinetics of Activation Controlled Consecutive Electrochemical Reactions: Anodic Evolution of Oxygen. *The Journal of Chemical Physics* **1956,** *24* (4), 817-827.

4.0 Spin-polarized Photoemission from Chiral CuO Catalyst Thin Films

This chapter was reprinted with permission from Möllers, P. V.; Wei, J.; Salamon, S.; Bartsch, M.; Wende, H.; Waldeck, D. H.; Zacharias, H., Spin-Polarized Photoemission from Chiral CuO Catalyst Thin Films. *ACS Nano* **2022,** *16* (8), 12145-12155. Copyright 2022 American Chemical Society. I was reponsible for developing the electrodeposition method of the chiral CuO film, making the CuO films and collecting the thickess measurements of the CuO films. The rest of the work was done by our collaborators.

4.1 Introduction

The electrolysis of water holds promise to provide a route for the production of hydrogen, which is a sustainable fuel when generated by electricity from renewable energy sources, like wind power, photovoltaics, or direct water splitting by sunlight.[1-4] For the latter process, the overall efficiency of the water-splitting reaction, comprising the hydrogen evolution reaction (HER) at the cathode and the oxygen evolution reaction (OER) at the anode, is severely limited by the high overpotential required for the OER.[5] Because molecular oxygen is a triplet species in its ground state, the overpotential is thought to arise partially from spin constraints in the formation of the O=O double bond. Furthermore, the OER at the anode suffers from side reactions, such as the generation of hydrogen peroxide, which can degrade the electrode material.

Recent work has demonstrated that the electron spin provides a means to control and enhance the chemical selectivity of the electrocatalytic water-splitting reaction.[6-10] The OER

involves the transfer of four electrons to the anode, that is, through the catalytic surface of the electrode material, and the generation of surface-adsorbed radical intermediates (OH, O, OOH). If the electron current to the anode is spin polarized, then so must be the intermediate radicals generated on the catalyst surface. The spin polarization is believed to favor the formation of triplet oxygen and to suppress the generation of singlet byproducts, such as hydrogen peroxide. The initial implementations[6-8] of this concept were based on the chirality-induced spin selectivity (CISS) effect[11] in chiral organic molecule layers that were adsorbed on the electrode surface. This concept was extended to intrinsically chiral cupric oxide (CuO)[9] and cobalt oxide (CoO*x*)[10] catalyst materials, which spin filter electron currents and therefore spin polarize intermediate radical species. While these explorative approaches have proven successful, the origin of the electron spin polarization in the chiral oxide layers is not yet understood. Direct electron polarimetry established CISS so far for helical organic molecules such as DNA,[12, 13] PNA,[14] oligopeptides,[15] and helicene.[16] To promote the well-targeted improvement of these catalyst systems, an understanding of the spin-polarizing mechanism in the chiral oxide layers is required. This work explores the electron spin selectivity by spin-resolved photoemission measurements conducted with chiral CuO thin films that were electrochemically deposited onto 20 nm thick Au films using a method pioneered by Switzer et al.[17-19] Circular dichroism (CD) spectroscopy is used to confirm that the electrodeposited oxide films possess a well-defined chirality, and Mott polarimetry is used to quantify the spin-polarized photoelectron distributions. Photoelectrons are generated by UV laser radiation impinging either from the CuO-coated front or from the substrate (back) side of the UV-transparent samples. The photoelectron spectra indicate that the relative numbers of photoelectrons emitted from the CuO film itself and from the gold substrate depend on the illumination direction. It is found that, upon changing the excitation direction, which changes the source of photoelectrons

from either the gold substrate or the chiral CuO film, the sign of the spin polarization changes. The results provide further evidence that the spin polarization in the chiral CuO layer is strongly energy dependent, because backside illumination yields electrons with higher kinetic energies. Magnetization curves indicate a weak ferromagnetic behavior in the chiral oxide layers and therefore suggest that the measured spin polarization could arise as a sum of the CISS effect and an intrinsic spin polarization in these layers due to structurally no longer compensated spins in the usually antiferromagnetically (AF) ordered CuO or by the Dzyaloshinsky-Moriya interaction.[20, 21]

4.2 Results and Discussion

4.2.1 Film Deposition and Characterization

While transition metal oxides are generally achiral, chiral oxide layers can be grown by the introduction of a chiral bias in the layer deposition process. Switzer et al. demonstrated the electrodeposition of chiral copper oxide layers from Cu(II)-ligand complexes in solution.[17, 18] The films grown based on this method exhibit a well-defined oxidation state and crystallographic texture on both monocrystalline[17, 18] and polycrystalline[17, 19] substrates. Copper complexes with chiral ligands, such as tartaric acid, can be employed as chiral precursors to electrodeposit chiral CuO films.[18, 22] The sense of the oxide film's chirality ("left" vs "right") is determined by the enantiomeric form of the ligand, and this enantioselectivity allows for the generation of films with identical chemical composition but opposite handedness.

For the present study, CuO films were electrodeposited from a solution containing chiral Cu(II)-tartrate complexes as described previously.[9] The film thickness as a function of the

electrodeposition time was calibrated by atomic force microscopy (AFM) line profile measurements. Films with a thickness ranging from 5 to 40 nm were investigated. The films were deposited on fused silica slides coated with 20 nm thin gold films on 3 nm thin titanium adhesion layers. This allows for UV illumination from both the front (CuO) and back (substrate) side of the samples and for the acquisition of optical absorption and circular dichroism spectra. Samples with CuO layers deposited from complexes containing L-[(R,R)-(+)-] and D-[(S,S)-(−)-] tartaric acid are labeled as L- and D-CuO in the following.

The nanometer- to micrometer-scale film quality was evaluated by AFM measurements. Representative topography images are shown in section S1 of the Supporting Information. Consistent with previous scanning electron microscopy (SEM) studies,[9] the films have a crystalline structure. The crystallite size is comparable to the layer thickness, which gives rise to a rather high roughness of ∼10 nm at the nanometer scale. The topography is independent of the film's chirality. On the micrometer scale, the films are mostly continuous but, nevertheless, exhibit defects and inhomogeneities.

4.2.2 Copper Oxidation State

X-ray photoelectron spectroscopy (XPS) of the Cu 2p peak region allows one to determine the oxidation state of Cu in the film. A representative example is given in Figure 1. The chemical shift of the Cu $2p_{3/2}$ peak at E_b = 933 eV differs between CuO (i.e., Cu^{2+}) and Cu_2O (Cu^{+}) by ∼1.5 eV.[23] Multiplet broadening is only observed in the case of CuO, and the satellite peaks around E_b ≈ 940 to 945 and 963 eV, arising from shakeups of the $3d^9$ state of Cu^{2+}, are not present in Cu_2O.[24] Therefore, the observed spectra can unambiguously be assigned to originate from CuO. Survey

spectra can be found in section S2 of the Supporting Information. Further high-resolution XPS spectra obtained from several oxide films were acquired in order to analyze for possible ferromagnetic contaminations from cobalt, iron, nickel, chromium, or manganese. Using both XPS and time-of-flight secondary ion mass spectroscopy (ToF-SIMS), no evidence of ferromagnetic contamination was found (see the Supporting Information, sections S2 and S3, for more detail). Further, no carbon residues from the organic seed precursor were detected in the film with either method after the preparation was finished by final heating.

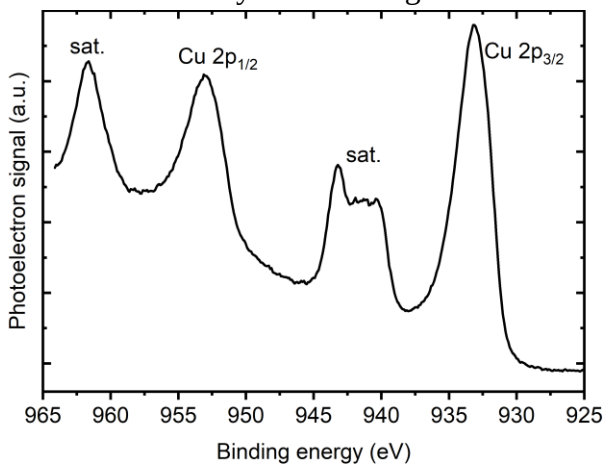

Figure 4-1. An XPS spectrum of the Cu2p peak region, acquired on a 40 nm oxide thin film, is shown. At binding energies of 940 to 945 eV and at 963 eV two satellite peaks to the Cu 2p3/2 and 2p1/2 peaks, respectively, appear which are indicative of CuO and are absent for Cu2O.[24]

4.2.3 Film Chirality

While the film deposition method employed here was unambiguously shown to generate chiral oxide films, the nature of this chirality is the subject of ongoing research. The means through which surfaces of materials with an achiral bulk structure (e.g., face-centered cubic (fcc) and body-centered cubic (bcc) lattices) can be rendered chiral were previously presented by Gellman.[25] Notably, surfaces of these materials with higher Miller indices (*hkl*) with $h \neq k$, $k \neq l$, $l \neq h$, and $h \times k \times l \neq 0$ can exhibit step edges with low symmetry that make the surfaces intrinsically chiral.[26]

CuO has a monoclinic structure; that is, exactly one angle between the lattice vectors deviates from 90° and induces a screw symmetry along the *b*-axis [010]. Planes that are parallel to this axis are achiral, and those with $k \neq 0$ are chiral.[27] The chirality of the CuO layers is, besides optical CD measurements, predominantly established through X-ray diffraction (XRD)[18, 22] and X-ray photoelectron diffraction (XPD)[22] measurements. These studies showed that the chiral CuO films have textures in which chiral planes are preferentially exposed along the sample surface plane. More specifically, the oxygen atoms in the CuO lattice structure can occupy two nonequivalent positions.[22] The XPD measurements, which are sensitive only to the topmost surface layers, reveal that the surface chirality is determined by which of these oxygen atoms terminate the surface. Switzer et al. also demonstrated that the chiral films can act as enantioselective catalysts.[17] Recent transmission electron microscopy (TEM) studies of similar compounds by Bai et al. furthermore indicate that the bulk crystal structure of the investigated nickel and iron oxide films is chirally distorted.[28, 29]

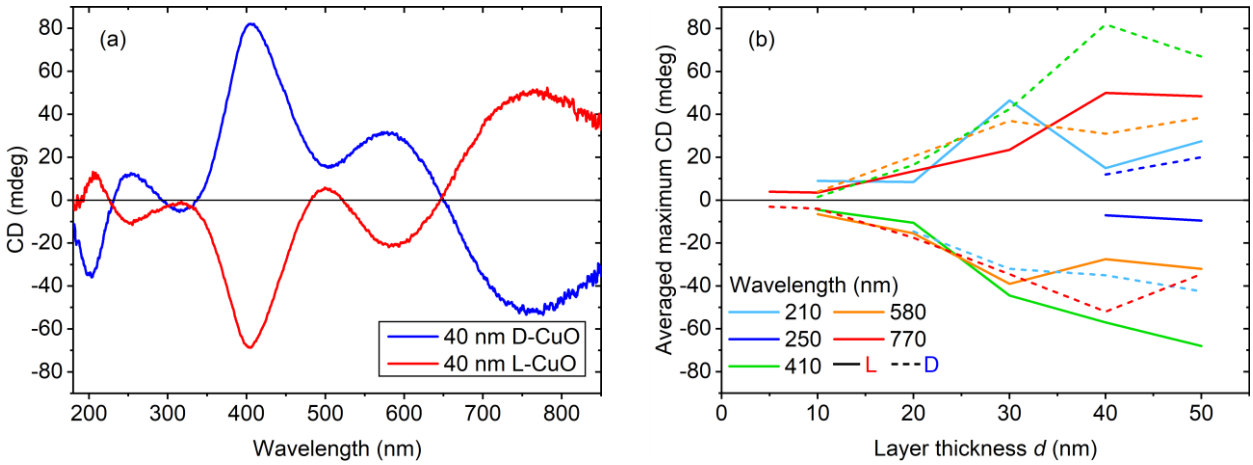

Figure 4-2. CD spectra measured on 40 nm CuO thin films of either handedness (a) and the CD magnitude at different wavelengths as a function of the film thickness (b).

To confirm that the films investigated in this study are chiral as expected, transmission circular dichroism (CD) spectra were acquired from each sample prior to the photoemission measurements. Figure 2a shows representative CD spectra measured on 40 nm CuO thin films of

both L and D chirality. The spectra show a CD of up to 80 mdeg and confirm that the films are indeed chiral. The CD spectra of the L and D films are, to a good approximation, mirror images of one another, indicating that the films deposited from complexes with L- and D-tartaric acid have opposite chirality. The CD magnitudes at the various peak wavelengths are shown in Figure 2b as a function of the film thickness. A systematic increase of the CD magnitude with the film thickness is observed, which suggests that the chirality is retained throughout the entire layer thickness. This supports the notion of a chiral bulk structure, that is, a chirally distorted atomic lattice. The energetic positions of the spectral peaks (Figure 2a) do not shift with the film thickness.

4.2.4 Electronic Structure

Despite its relevance for high temperature superconductivity, the electronic structure of CuO, in contrast to Cu_2O, is still not fully elucidated. Theoretical band structure calculations deviate more strongly from experimentally obtained results for CuO than is the case for Cu_2O, and this may result from strong electron−electron correlation effects near the valence band edge (VBE).[30, 31] For very thin films, additional deviations from the bulk structure are possible, for example, due to (quantum) confinement effects or depending on a local film texture.

For initial characterization, baseline-corrected absorption spectra in the UV−vis−IR region were acquired. The data can be found in section S4 of the Supporting Information. At λ = 213 nm, the absorption coefficient is $\alpha = 3 \times 10^5$ cm^{-1}, corresponding to a 1/e penetration depth of ∼30 nm. Figure S6b,c shows Tauc plots that indicate the position of the main absorption edges. The direct and indirect band gaps are identified at ΔE_{dir} = 3.08 eV and ΔE_{ind} = 1.20 eV, respectively. The nature of the low-energy band gap is still under debate.[32] The higher-energy edge matches the position of the main peaks at λ = 410 nm in the CD spectra. The electronic structure of the samples

was further characterized by He I ultraviolet photoelectron spectroscopy (UPS) measurements[33] of both a 200 nm CuO thin film and the bare gold substrate. An energy level diagram derived from these data is shown in Figure 3. The work function of the 20 nm gold substrate is determined to be Φ_{Au} = 4.65 eV. This value is reduced compared to the work function of bulk gold because of the low film thickness, consistent with literature values.[34] The work function of the CuO sample is determined to be Φ_{CuO} = 4.61 eV, and the VBE of CuO is located 0.34 eV below the Fermi level; that is, VBE = Φ_{CuO} + E_{ion} ≈ 4.95 eV. Indeed, copper vacancies make cupric oxide an intrinsic p-type semiconductor.[35] The VBE position is higher than in bulk samples, where VBE = 5.4 eV,[36] but consistent with reports for CuO thin films.[25] Similar values were obtained from UPS spectra of 30 nm thin CuO films.

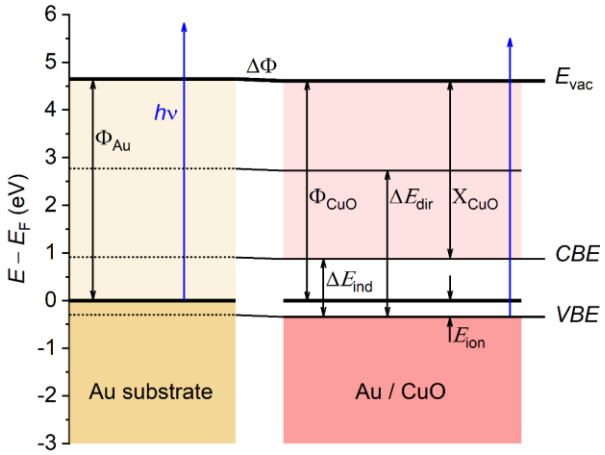

Figure 4-3. Energy scheme of the Au/CuO samples, determined from He I photoelectron spectra of a 200 nm CuO sample, and a bare gold substrate. Note that XCuO is the electron affinity of CuO and Eion is the position of the valence band edge relative to the Fermi level EF. A very slight shift ΔΦ of the vacuum level is measured. The other energies are specified in the text.

4.2.5 Spin Polarization Measurements

The spin polarization of photoelectrons emitted from the samples was measured in a Mott scattering apparatus, illustrated in Figure 4a, and described previously.[9] Photoelectrons are excited by laser pulses at λ = 213 nm ($h\nu$ = 5.83 eV) with a pulse duration of 200 ps and at a repetition rate

of 20 kHz. The light impinges on the samples along the surface normal, perpendicular to the surface plane, and the photoelectrons are as well collected along the surface normal. In the experimental geometry used, the spin polarization along the surface normal of the samples is measured. Throughout the measurement procedure, the polarization of the laser light is interchanged from s-linear to clockwise (cw) and counterclockwise (ccw) circular by the rotation of a quarter-wave plate (QWP). At each position of the QWP, about 104 electrons are collected. After a full QWP rotation, the measurement position is interchanged between the sample and a polycrystalline gold substrate without an oxide layer, mounted directly beneath the sample. The polycrystalline gold emits unpolarized electrons upon excitation with linearly polarized light and is used to correct for instrumental asymmetries.

In Figure 4b, the results from our previously published spin-resolved photoemission study[9] on chiral CuO layers are shown, where the illumination occurred from the front (CuO) side of the sample. Each data point comprises ∼100 single measurements, that is, ∼106 measured electrons. From samples coated with 5−50 nm thin CuO films, photoelectrons with an average spin polarization of up to $P = -10$ to −12% are emitted upon excitation with linearly polarized laser pulses at $\lambda = 213$ nm. These values were obtained from L-CuO films. The negative sign corresponds to electrons whose spin is aligned antiparallel to the electron momentum, that is, antiparallel to the surface normal of the sample. The values measured on D-CuO layers, that is, on layers with opposite chirality, on average show a spin polarization with the opposite sign of polarization, albeit at less significant values. The smaller magnitude of the spin polarization in these samples is the subject of further investigations, and we focus on the L-CuO samples in this study. However, the correct calibration of the Mott polarimeter was carefully confirmed prior and subsequent to each individual spin polarization measurement. The data include many samples, and

L and D samples were measured in random order. Thus, a systematic error in the spin polarization toward negative values seems to be unlikely. This asymmetry of the spin polarization values is therefore a property of the chiral CuO films. In Figure 4c, results of additional spin polarization measurements on 5−40 nm thick L-CuO layers are shown. Filled diamond symbols correspond to measurements in which the sample was irradiated from the CuO-coated front side in technically identical measurements as shown in Figure 4b. Multiple data points at each thickness correspond to spin polarization measurements on different positions of the sample surface. With an uncertainty $\Delta P = \sigma/\sqrt{n}$ of up to $\Delta P = \pm$ 1.9% points, the standard deviation σ normalized to the number of measurements n, shown in the shaded area, reveals a considerable spread of the results on most samples. We previously considered only the maximum values on each sample, as reduced values are most likely due to inhomogeneities and defects on the surface and hence do not reflect the true

spin polarization capacity of the samples. The spin polarization values shown in Figure 4b,c are consistent with one another.

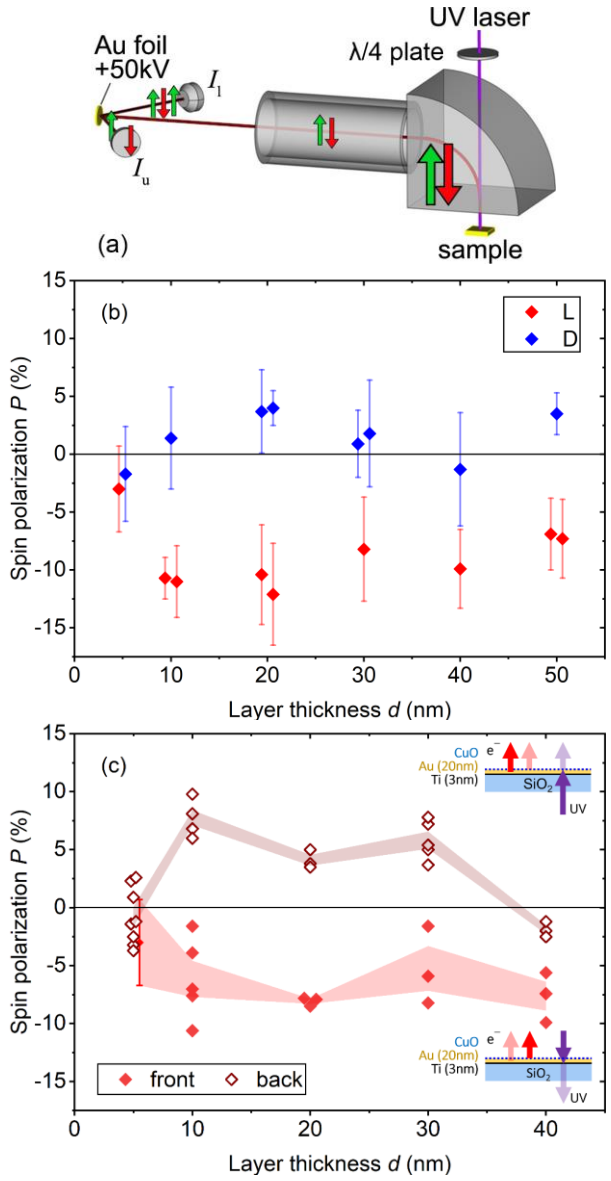

Figure 4-4. Simplified scheme of the Mott scattering setup. (b) Spin polarization measured upon front side excitation with linearly polarized light for L- and D-CuO films.9 (c) Further technically identical measurements (full symbols) and measurements with the laser impinging on the back side of the partially UV-transparent samples (empty symbols). Note that the plots in (b) and (c) have different scales for their horizontal axes. The red-shaded areas indicate the standard deviation σ/√n, normalized to the number of individual measurements, n. In figure 5 (c), only one data point is available for 5 nm thin films; here, the uncertainty of the single measurement is indicated. Figure 5 (b) reprinted with permission from ref. 9. Copyright 2019 American Chemical Society.

Further measurements were conducted with the laser impinging on the back side of the sample, as illustrated in the inset of Figure 4c, and the results of these measurements are shown as open diamond symbols. We note that the same samples and the same surface areas were studied as for front side illumination, within the positioning accuracy of the 300 μm diameter of the laser beam. Because the substrate is UV-transparent fused silica, most (~80%) of the light is absorbed in the gold layer underneath the CuO films. Further, the CuO film thickness is in the range of the electron mean free path (MFP). Hence the relative amount of the photoelectrons originating in the gold layer, instead of the CuO film, is expected to be significantly increased for these measurements as compared to front side illumination. As with front side illumination, no significant spin polarization is obtained from the 5 nm thin CuO films, and the highest polarization of $P \approx +10\%$ is obtained from the 10 nm thick films. Notably, the sign of the spin polarization is positive upon irradiation from the back side; that is, the electrons spins are, on average, aligned parallel to the electron momentum, in contrast to the illumination from the front side. For the 40 nm thick film, however, a negative polarization is measured independently of the direction of illumination. To understand these results, the origin of the photoelectrons excited from both the front and back sides of the samples is discussed in the following.

4.2.6 Origin of the Photoelectrons

The inelastic MFP of electrons traveling through the nonmolecular solid follows a general empirical dependency on the electron energy.[37] This dependency reflects the energy-dependent cross sections of different excitation processes, such as the generation of phonons, plasmons, or electron−hole pairs. On the basis of the work function of the CuO samples and the employed laser photon energy, the electrons that are measured in the present work have energies of $E - E_F \approx$

4.6−5.8 eV with respect to the Fermi level. The MFP at these energies is in the range of 4−8 nm, on the order of the film thickness. Hence, a careful analysis of the electron's origin for the different measurements is conducted below.

4.2.6.1 Intrinsic Spin Polarization

In materials with significant intrinsic spin−orbit coupling, the spin degeneracies in the valence band are lifted, and electrons can be excited into specific final spin states. In the present experimental geometry both light irradiation and electron emission occur along the surface normal. In this highly symmetric configuration and with centrosymmetric surfaces, such as the (111) surface of metals with an fcc crystal lattice (e.g., gold), unpolarized electrons are emitted upon irradiation with unpolarized or linearly polarized light. Circularly or elliptically polarized light excites spin-polarized electrons,[38-40] and the sign of the spin polarization is reversed due to symmetry constraints if the direction of the photon's circular polarization, clockwise or counterclockwise, is reversed, that is, $P_{cw} = -P_{ccw}$. As a manifestation of the spin-split band structure of the material, this spin polarization is material specific. Because the polarization of the incident laser light was interchanged between s-linear, cw, and ccw circular throughout the spin polarization measurement procedure, these data provide the initial evidence that irradiation of the samples from the front side predominately generates photoelectrons from the CuO film rather than from the gold substrate underneath it.

Figure 5a shows the spin polarization difference ($P_{cw} - P_{ccw}$) upon excitation with circularly polarized light impinging on the front side of the samples. The data points at d = 0 nm (orange) are measured on a bare polycrystalline gold substrate, from which an average differential polarization of $(P_{cw} - P_{ccw}) \approx (6.8 \pm 0.5)\%$ is observed in this excitation geometry. The deviations of the single measurements from the mean value reflect variations in the local crystallinity of the

surface. At the other extreme of the thickness range, on 200 and 210 nm thick CuO films, the electron MFP of 4−8 nm and the light penetration depth of ~30 nm in CuO imply that all of the detected photoelectrons originate from the CuO layer. These samples are therefore used as a CuO reference. On these samples, a differential polarization of ($P_{cw} - P_{ccw}$) ≈ −3% is measured upon excitation from the front side.

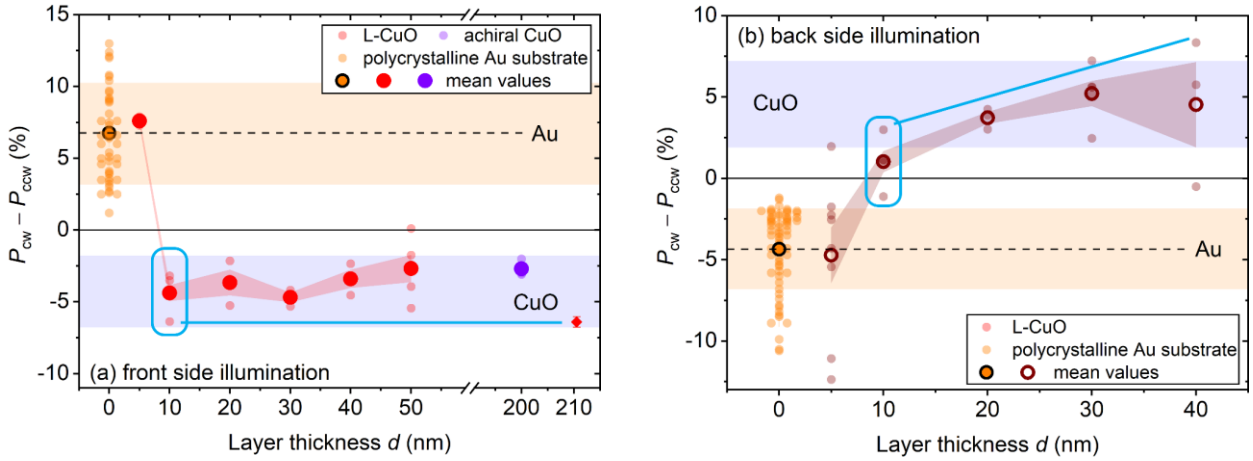

Figure 4-5. Differential spin polarization measured upon excitation with cw and ccw circularly polarized light impinging on either the front (a) or back (b) side of the samples. The standard deviation σ/√n, normalized to the number of individual measurements, n, is indicated by the red-shaded area. The light blue lines are a guide to the eye; overlapping points are offset for clarity. The same sample areas were studied in (a) and (b).

For 5 nm thin CuO films the polarization values are mostly comparable to the values measured at the bare Au substrate, which suggests that the electrons are mostly excited in the gold layer. For a film thickness of d = 10 nm and larger, the spin polarization values consistently and significantly deviate from what is measured on gold and closely resemble the polarization measured on the CuO reference samples. The broader distribution of the individual results suggests that the layers are laterally inhomogeneous over the sample surface area. The average photoelectron spin polarization, however, does not change with the CuO film thickness. Thus, for CuO films with a thickness of 10 nm or more, the detected photoelectrons originate predominantly from the oxide film rather than from the gold substrate, when the samples are irradiated from the front side. In Figure 5b the results of identical measurements performed with excitation from the

sample back side are shown. Changing from front to back side illumination reverses the k vector of the laser light with respect to the spin quantization axis. Because the sense of the circular polarization is defined with respect to the k vector of the light, changing the illumination direction interchanges cw and ccw polarization relative to the space-fixed spin quantization axis. Consequently, upon excitation from the back side, the gold substrates emit electrons with the reversed average differential spin polarization, $(P_{cw} - P_{ccw}) = (-4.4 \pm 0.3)\%$. In contrast to the observations for front side illumination, the differential electron spin polarization now increases until a CuO film thickness of ~40 nm. While for front side illumination the 10 nm thick CuO film already gives rise to the same polarization value as the CuO reference, the polarization values obtained with back side illumination are distributed in a range intermediate between what is measured on the gold and the CuO references. In the case of front side illumination, the maximum polarization values are constant from 10 nm thickness on, while in the case of back side illumination they reach the maximum value only at a thickness of 40 nm. These observations support the notion that, for back side illumination of the samples, the observed photoelectrons originate predominantly from gold, albeit with a contribution from the CuO layers.

Energy Considerations. The conclusions drawn from the differential spin polarization are corroborated by time-of-flight (ToF) UPS spectra acquired with radiation at $\lambda = 213$ nm, as used for the spin analysis. These spectra provide the electron energy distribution over which the spin polarization is averaged. In Figure 6a photoelectron spectra obtained from the bare thin-film gold substrates are shown. The dashed and solid orange lines denote photoelectrons from Au via front side and back side illumination, respectively, with the latter further highlighted by the yellow area in the graph. Here, the energy distribution of the photoelectrons and the sample work function are independent of the laser excitation direction. From the position of the Fermi edge at $E_{kin} \approx 1.07$

eV, a work function of $\Phi_{Au} \approx 4.76$ eV is calculated, which, with a small deviation, matches the value of $\Phi_{Au} = 4.65$ eV determined above by He I UPS. Also shown in Figure 6a is the spectrum measured on a 200 nm thick CuO film excited from the front side, as a blue line and blue-shaded area. At this thickness, all photoelectrons arise from the oxide layer. The maximum kinetic energy $E_{kin} = h\nu - \text{VBE} \approx 0.82$ eV indicates that the VBE is located 5.0 eV below the vacuum level, consistent with the value determined from the He I spectra (Figure 3). Because the work functions of both materials are similar, the difference in the maximum kinetic energies in the gold and oxide spectra reflects mostly the position of the VBE below the Fermi level.

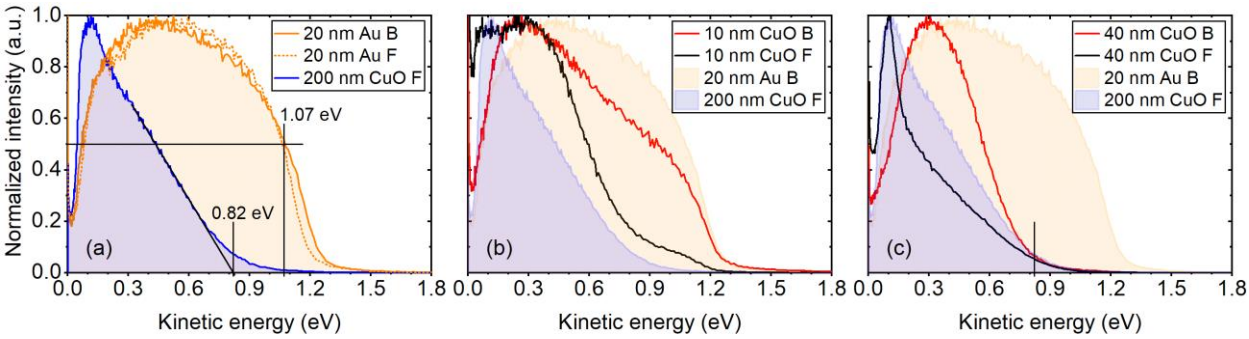

Figure 4-6. UV photoelectron spectra, acquired with the laser irradiating the samples at λ = 213 nm either from the front (labeled "F") or back (labeled "B") side. Shown are (a) reference spectra from a from a 200 nm thick CuO layer and the bare gold substrate and spectra from samples with (b) 10 nm and (c) 40 nm thick CuO films.

Figure 6b shows spectra acquired on a sample with a 10 nm thick CuO film. The gold and CuO reference spectra shown in Figure 6a are replicated as shaded areas for comparison. On this sample, the maximum kinetic energies match well the value found on the bare gold film, but the shape of the spectra has changed. It can be described as a composite of the Au and CuO spectra in panel (a). On the basis of the VBE of the CuO layer and the work function of the pure gold film, electrons with kinetic energies in the range of $E_{kin} = 0.0{-}0.8$ eV arise from both the gold and the oxide film, while electrons with higher energies of up to $E_{kin} = 1.23$ eV arise solely from the gold substrate.

The front side illumination spectra exhibit pronounced secondary electron signals at low kinetic energies. (Note that the samples were neither heated nor sputtered to avoid impairing the chiral layer structure.) The secondary electron signal varies between the individual measurements, which hampers an exact quantification of the Au and CuO contributions in the spectra. However, the Au/CuO ratio in the photoelectron signal is significantly larger for back side than for front side illumination. To obtain an estimate of the electron yield from either layer, the gold reference spectrum was scaled to match the higher-energy parts of the spectra from the 10 nm thick CuO film; see section S5 in the Supporting Information. The total photoelectron signal from the gold layer is quantified by integration over these scaled gold spectra. For each illumination direction, the area underneath the scaled gold spectrum is subtracted from the area underneath the CuO/Au spectrum; the difference is assumed to correspond to the photoelectron signal from the CuO layers. The ratios of the spectral areas indicate that, for front side illumination, the electron signal from the 10 nm thick CuO layer is ∼4 times higher than the signal from the gold layer. For back side illumination, the ratio is roughly reversed, that is, only onequarter of the photoelectrons is emitted from the oxide layer.

The spin polarization measurements shown in Figure 4c demonstrate that the sign of the spin polarization becomes independent of the direction of illumination at a CuO layer thickness of 40 nm. The photoemission spectra measured on this sample are shown in Figure 6c. In contrast to the thinner films, the maximum kinetic energy for the 40 nm CuO films is as well independent of the direction of illumination and corresponds to the value found in the reference CuO spectrum. The data therefore indicate that the contribution of electrons originating in the gold layer to the signal is negligible in oxide layers with a thickness of 40 nm, or larger.

4.2.7 Origin of the Photoelectron Spin Polarization

The ability of chiral oxide films to spin filter electron currents was reported previously for chiral CuO[9] and, indirectly, for chiral CoO*x*[10] layers, and those findings were interpreted as a manifestation of the CISS effect. This more comprehensive study of the photoelectron spectra and spin polarization measurements indicates that the observed spin polarization depends on the electron kinetic energy and the material from which the electrons originate. In agreement with the earlier study, the electrons arising from the gold layer underneath the oxide as well as from a finite depth in the oxide layer itself appear to be spin filtered during the transmission through the chiral oxide. As shown in Figure 4a, the spin polarization is correlated with the film chirality; this observation strongly supports the interpretation as a CISS-based phenomenon. Indeed, there is growing evidence for the occurrence of CISS in inorganic solids.[10, 41-43] In addition to the spin filtering effect, however, photoelectrons generated directly from the CuO itself contribute significantly to the spin polarization, vide infra, which suggests the presence of an additional polarization mechanism in the oxide layer, distinct from the spin filtering. We elaborate on this interpretation in the following section.

The photoelectron spectra presented in Figure 6b,c can be understood as composites of the spectra of the bare gold and pure CuO. The lower-energy electrons (E_{kin} < 0.8 eV) are emitted predominantly from the CuO layer, while the higherenergy electrons (E_{kin} > 0.8 eV) originate solely from the gold. On the basis of this interpretation, the ratio of the electrons emitted from either material depends on both the oxide layer thickness and the direction of illumination. The fraction of electrons emitted from the gold layer is higher for thinner oxide layers and illumination from the back side. Figure 6c indicates that no photoelectrons from the gold layer are detected on a sample with a 40 nm thick oxide film.

As Figure 4c reveals, the sign of the spin polarization changes with the CuO film thickness and the photoexcitation geometry; this dependence correlates with the changes in the photoelectron kinetic energy distributions as a function of the photoexcitation geometry and the CuO thickness. The spin polarization is positive for back side illumination and an oxide film thickness below 40 nm. For back side illumination and thicker films as well as upon front side illumination, a negative spin polarization is found. These correlations between the data sets suggest that, for L-CuO samples, the photoelectrons originating directly from the CuO are negatively polarized, while the (higher-energy) photoelectrons originating from the Au are positively polarized. The relative numbers of photoelectrons from either layer suggests that the electrons originating from the Au exhibit a similar magnitude of polarization as those from CuO. However, the high fraction of secondary electrons in the lower-energy interval is expected to reduce the average spin polarization if the spins depolarize during the scattering events, which yield the secondary electrons. At higher energies, the relative number of secondary electrons is significantly lower, which suggests that the spin polarization in the lower-energy interval, that is, of the electrons originating predominantly in the CuO film, is initially larger than the polarization of the higher-energy electrons emitted solely from the Au film. Because linearly polarized UV light is employed, the electrons originally emitted from the Au substrate are unpolarized and must become spin polarized as they transit through the chiral structure of the CuO film. That is, they are spin filtered by the CISS effect. With respect to the Fermi level, the electrons from the CuO and Au layers have energies of $4.6-5.4$ eV and up to 5.8 eV, respectively. A strong energy dependence of the spin filtering, including changes in sign on a scale of a few 100 meV, is consistent with the predictions of various model calculations,[44-47] albeit such calculations are currently only available for molecular spin-filtering

systems. The correlation between the electron kinetic energy distributions and the measured average spin polarization could hence reflect the energy dependence of the CISS effect.

Apart from a CISS-related spin filtering effect, however, the measured spin polarization shows a contribution from a distinct second mechanism, where the electrons emitted from the CuO are intrinsically spin polarized. Given that the spinpolarized photoelectron distribution arises from a pure CISS related spin filtering effect for photoelectrons originating from the Au (and inner layers of CuO) and an intrinsic spin polarization for the photoelectrons originating the CuO layer, what causes the intrinsic spin polarization in the chiral CuO? In CuO, with Cu(II), one d electron is unpaired,[48] and cupric oxide is antiferromagnetic below a Néel temperature of ∼230 K.[49] Above this temperature, the copper and oxygen atoms are thought to form one-dimensional antiferromagnetic chains in the [101] direction.[48, 50] The strength of the exchange term, which could induce long-range magnetic order, depends on the Cu−O−Cu bond angle.[49] We hypothesize that a chiral distortion of the atomic lattice could prevent the compensation of the magnetic moments of the magnetic sublattices and introduce ferrimagnetic behavior. Similarly, a Dzyaloshinsky-Moriya interaction,[20, 21] arising from the asymmetrically distorted chiral CuO lattice,[25, 26] may lead to a not fully compensated antiferromagnetic order.

4.2.8 Magnetics

To examine the magnetic properties of the chiral CuO thin films, magnetization curves were acquired with a vibrating sample magnetometer (VSM). Results of these measurements are shown in Figure 7. The $M(H)$ curves were recorded at temperatures of 4.3 and 300 K and up to maximum fields of ±9 T. A measurement at T = 300 K on a sample with an achiral 200 nm thick CuO film, shown in Figure 7a, reveals purely diamagnetic behavior, consistent with the negative

susceptibility of the Au and quartz substrate materials. No deviations that would indicate the presence of a ferromagnetic contaminant are evident. In contrast, a magnetization curve measured on a sample with a chiral, 200 nm thick L-CuO layer shown in Figure 7b exhibits paramagnetic behavior and a distinct, albeit small, magnetization hysteresis, indicative of ferromagnetic behavior. These signals are superimposed on the diamagnetic substrate signal. Figure 7c shows the sample curve after subtraction of the diamagnetic background (-3.9×10^{-3} $Am^2/(kgT)$) of the sample, representing only the paramagnetic signal and the ferromagnetic hysteresis of the oxide layer. From these data, a saturation magnetization of $\sim 6.3 \times 10^{-4}$ Am^2/kg at 0.5 T is determined. This value corresponds to a magnetic moment of $\sim 1.3 \times 10^{-2}$ Bohr magnetons per copper atom. Figure 7d shows a close-up view of the same data, along with corresponding data acquired at 4.3 K. The curves exhibit asymmetric zero-field magnetization values of 0.3×10^{-4} $Am^2/$ kg and -0.9×10^{-4} Am^2/kg at 300 K and $\sim 0.6 \times 10^{-4}$ Am^2/kg and -1.6×10^{-4} Am^2/kg at 4.3 K. An average coercive field strength of ~5 mT is determined at 300 K, which increases to 9 mT at 4.3 K. Because of the ultrathin film thickness, the absolute oxide amount in the samples is low. To assign the ferromagnetic behavior to the oxide layer, a possible contamination with ferromagnetic elements was assessed through high-resolution XPS spectra acquired in the 2p peak regions of the ferromagnetic elements Cr, Mn, Fe, Co, and Ni. On the basis of these data, contamination above the XPS detection threshold of ~0.1 atom % in the probed surface layers (up to several nanometers depth) was ruled out. Subsequently, time-of-flight secondary ion mass spectra (ToF-SIMS) were acquired, probing the entire layer thickness, which did not reveal any ferromagnetic contamination either; see section S3 in the Supporting Information. Ferromagnetic behavior of transition metal

oxides is discussed in the literature as a consequence of oxygen vacancies and interfacial effects.[51-58]

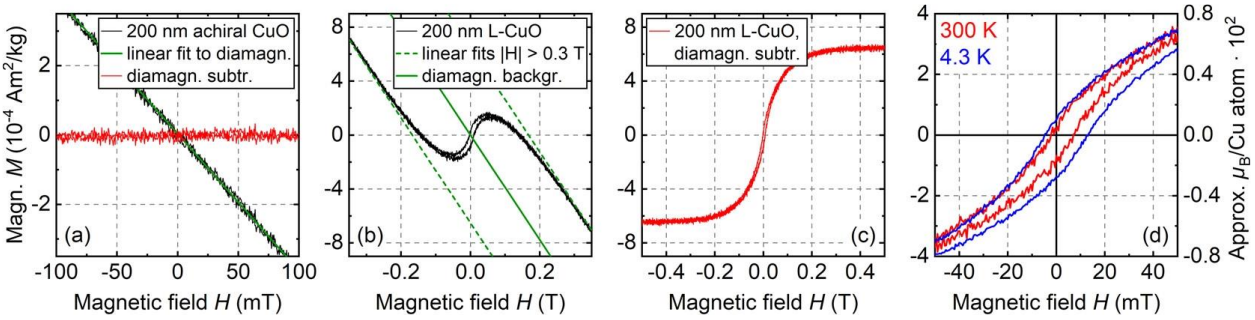

Figure 4-7. Magnetization curves at T = 300 K of a sample with an achiral 200 nm thick CuO film (a) and a 200 nm thick L-CuO film before (b) and after (c) subtraction of the diamagnetic substrate signal. (d) Hysteresis at T = 4.3 K (blue) and 300 K (red) on an enlarged scale.

The finding of these hitherto rather explorative measurements is that the chiral CuO layers, in contrast to their achiral counterparts, can exhibit ferrimagnetic behavior. It supports the hypothesis that the energy dependence of the measured spin polarization reflects an interplay of CISS and a magnetization in the material rather than solely the energy dependence of the CISS effect. The origin of the magnetization of the CuO layers is not yet identified. The chiral CuO films were shown to have textures that preferentially expose chiral planes along the sample surface;[17, 18, 22] all chiral planes have Miller indices (*hkl*) with $k \neq 0.27$. The copper atoms in the oxide form one-dimensional antiferromagnetic chains along the [101] direction.[48, 50] Since $k = 0$, this orientation cannot be exactly perpendicular to any chiral plane. We argue that the atomic lattice of the CuO films is chirally distorted, consistent with findings by Widmer et al.[22] using XPD and by Bai et al.[28, 29] using a TEM analysis. The observed monotonous increase of the CD magnitude with the film thickness (Figure 2b) supports this argument. We hypothesize that the chiral, stressed lattice exhibits a canted spin order,[59] which introduces a magnetic moment with a fixed orientation within the crystal lattice that is perpendicular to the direction of the AF ordering. As mentioned above, the direction of the AF ordering is never exactly perpendicular to the preferentially exposed chiral planes. Therefore, even though the plane in which the magnetic moment induced by the spin

canting lies is not known, the magnetic moment will generally have a component perpendicular to the chiral planes. Simultaneously, the film textures imply that most CuO crystallites have the same out-of-plane orientation. The spin canting-induced magnetic moments thus have nonzero components perpendicular to the sample surface, and these components do not cancel out even if the in-plane (azimuthal) orientation of the crystallites is random; see section S6 of the Supporting Information.

Testing this hypothesis will require further experimental investigations, beyond the scope of the present study. Employing energy-resolved spin polarization measurements, the contribution of the bulk CuO can be singled out when well-defined magnetizations of the samples are related to the spin polarization of emitted photoelectrons. However, the asymmetric remanent magnetization values evident in Figure 7d are consistent with a magnetization bias introduced by the proposed mechanism. A chirality-induced magnetization switching of ferromagnets, which would manifest itself similarly in a shifted zero-field magnetization, was recently observed by Paltiel and co-workers after adsorption of α-helix polyalanine on a cobalt substrate.[60, 61] This effect was attributed to a charge polarization upon adsorption of the molecules that is accompanied by a spin polarization along the molecules.[62]

4.3 Summary and Outlook

In conclusion, cupric oxide thin films electrodeposited on polycrystalline Au film electrodes from a solution of Cu^{2+}/ tartaric acid were shown to exhibit strong circular dichroism that depends on the enantiomeric form of the tartaric acid in solution. The chiral CuO films were studied by Mott polarimetry and magnetometry. By controlling both the illumination direction and

the oxide film thickness, the relative number of photoelectrons originating from the gold substrate and from the copper oxide layer could be distinguished. Analysis of the photoelectron spectra and the spin polarization measurements indicates that the spin polarization of photoelectrons emitted from the Au/CuO layer system depends on the origin of the photoelectrons. The analysis shows that the photoelectrons originating from the gold substrate are spin filtered by the chiral oxide layers, as a manifestation of the CISS effect. The energy dependence of the spin filtering is consistent with theoretical considerations of models of helical organic systems[43, 46] and helical minimal models.[45] Beyond this notion, the measured spin polarization values could be rationalized as a sum of two contributions by assuming that photoelectrons emitted from the oxide layer are intrinsically spin polarized. We hypothesize that the chiral modification of the oxides lifts the antiferromagnetic compensation of the magnetic moments of the unpaired copper d electrons and introduces ferrimagnetic behavior. Indeed, a weak magnetization hysteresis was evident in VSM measurements, which could not be related to a possible ferromagnetic contamination of the samples. The definitive determination of the nature of these mechanisms will require quantitative knowledge about the energy dependence of the spin polarization, and it is a subject of future investigations.

4.4 Methods

4.4.1 Film Deposition

The film deposition procedure, as adopted from Switzer et al.,[17-19] was described previously.[9] For the electrodeposition a PAR model 173 galvanostat was used. The reference and

counter electrode consisted of an Ag/AgCl electrode and a Pt foil, respectively. The Au substrates acted as the working electrode. The electrodeposition solution comprised 0.2 M $CuSO_4$ (≥98.0%, EM Science) and 0.2 M L-tartaric acid (≥99.5%, Sigma-Aldrich) or D-tartaric acid (≥99.0%, Sigma-Aldrich) in 3 M NaOH. The current density controlled at the working electrode was 0.5 mA/cm^2. Depending on the desired film thickness, the deposition time was varied between 10 min and 1 h. After the deposition procedure, all samples were baked at 450 °C for 1 h to ensure the complete oxidation of the films from Cu_2O to CuO and remove any organic residues.

4.4.2 XPS Measurements

XPS measurements were performed on a Kratos Axis Ultra system using monochromatized Al Kα radiation at $h\nu$ = 1486.6 eV. The binding energy scale was calibrated to the Fermi edge and the C 1s peak at 284.8 eV.

4.4.3 He(I) UPS Measurements

The He(I) UPS measurements were conducted emloying He(I) radiation at $h\nu$ = 21.22 eV and a SPECS Phoibos 150 hemispherical analyzer. Throughout the measurements, a sample bias of −4.0 V was applied.

4.4.4 213 nm UPS Measurements

Ultraviolet photoelectron spectra were acquired employing the same laser radiation as used for the spin polarization measurements and inside the same UHV chamber. In contrast to these

measurements, the laser impinged onto the sample surface under an angle of 60° with respect to the surface normal. The electrons were detected around the surface normal. Energy resolution was achieved using a 400 mm long time-of-flight tube; the electrons were registered by a microchannel plate detector.

4.4.5 Absorption and CD Measurements

UV−Vis absorption measurements were performed using a Jasco V-770 absorption spectrometer at a measurement speed of 100 nm/min and with both step size and bandwidth set to 1 nm. For the optical CD measurements a Jasco J-815 CD spectrometer was used. The data were recorded at 100 nm/min and with a pitch of 0.2 nm and an integration time of 1 s. The CD specta were each averaged over three runs. In each case, the sample was mounted on a custom-designed sample holder in which the samples were oriented perpendicularly to the light direction. The sample holder included an aperture of approximately 2×4 mm^2, exposing only the oxide-coated surface area to the light. All optical measurements were corrected for a baseline measurement on a bare quartz/Au substrate sample.

4.4.6 Spin Polarization Measurements

The spin polarization of photoelectrons emitted from the samples was measured in a Mott scattering apparatus, illustrated in Figure 4a. As described previously,[9] photoelectrons are excited by laser pulses at λ = 213 nm ($h\nu$ = 5.83 eV) with a pulse duration of 200 ps and at a repetition rate of 20 kHz. The light impinges on the samples along the surface normal, perpendicular to the surface plane, and the photoelectrons are as well collected along the surface normal. Electron

optics guide the electrons toward a scattering target that is set to a potential of +50 kV, accelerating the electrons to weakly relativistic energies. Two detectors placed symmetrically around the incident electron beam at angles of ±120° register electrons that are backscattered from the target. Because of the high scattering energy, the nuclei of the scattering target, which consists of a 70 nm thin gold foil, generate a magnetic field in the rest frame of the electrons and introduce a spindependent term into the scattering potential. The intensity asymmetry $A = (I_u - I_l)/(I_u + I_l)$ in the number of electrons I_u and I_l scattered into the upper and lower detectors, respectively, is therefore a measure of the average spin polarization of the emitted photoelectrons. The spin polarization P is connected with this asymmetry A via the analyzing power or Sherman function S of the Au scattering foil by $P = A/S$. Because the scattering cross section only depends on the projection of the spin onto the direction of the magnetic field, the electron optics include an element to bend the electron beam by 90°, converting an initially longitudinal spin polarization into a transverse polarization prior to the Mott scattering process. This means that the spin polarization along the surface normal of the samples is measured in the present configuration. Throughout the measurement procedure, the polarization of the laser light is interchanged from slinear to clockwise and counterclockwise circular by rotation of a quarter-wave plate (QWP). At each position of the QWP, ∼104 electrons are collected. After a full QWP rotation, the measurement position is interchanged between the sample and a polycrystalline gold substrate without an oxide layer mounted directly beneath the sample. The polycrystalline gold emits unpolarized electrons upon excitation with linearly polarized light and is used to correct for instrumental asymmetries. The measurements were conducted under ultrahigh vacuum (UHV) conditions at a base pressure of less than 3×10^{-9} Torr. The UHV chamber comprised a permalloy

shielding against external magnetic fields and was placed inside three Helmholtz coils, which compensate for the earth's magnetic field. The residual magnetic fields are smaller than $\sim$20 μT.

4.4.7 VSM Measurements

The magnetization curves were recorded using the vibrating sample magnetometry option of a Quantum Design DynaCool physical property measurement system (PPMS). The $M(H)$ curves were recorded at temperatures of 4.3 and 300 K and up to maximum fields of ±9 T. The entire samples were probed. The samples were mounted longitudinally using the original Quantum Design sample holders; that is, the in-plane component was measured.

4.5 Associated Content

4.5.1 Supporting Information

The Supporting Information is available free of charge at https://pubs.acs.org/doi/10.1021/acsnano.2c02709.

Additional XPS spectra, ToF-SIMS data, topographic AFM images, optical absorption data, information on the electron yield from the Au and CuO layers, and an illustration of the spin-canted magnetic order within the oxide layers (PDF).

4.5.2 Acknowledgements

We gratefully thank Dr. B. Tyler from the Münster Nanofabrication Facility for taking the ToF-SIMS spectra, and we thank Dr. B.P. Bloom for helpful discussions. Partial financial support through the Volkswagen Stiftung (HZ, grant no. 96451) and the NSF – DFG project "Echem: Spin-polarized electrons for spin selective electrocatalysis", grant nos. Za 110/30 – 1 (HZ), and by the US NSF through CHE-1900078 and CHE-2140249 (DHW) is gratefully acknowledged. Partial financial support by the German Research Foundation (DFG) via the CRC/TRR 247 (ID 388390466, Project B02) (HW) is gratefully acknowledged.

4.6 Reference

1.Fujishima, A.; Honda, K., Electrochemical Photolysis of Water at a Semiconductor Electrode. *Nature* **1972,** *238* (5358), 37-38.

2.Grätzel, M., Photoelectrochemical cells. *Nature* **2001,** *414* (6861), 338-344.

3.Hisatomi, T.; Kubota, J.; Domen, K., Recent advances in semiconductors for photocatalytic and photoelectrochemical water splitting. *Chemical Society Reviews* **2014,** *43* (22), 7520-7535.

4.Voiry, D.; Shin, H. S.; Loh, K. P.; Chhowalla, M., Low-dimensional catalysts for hydrogen evolution and CO2 reduction. *Nature Reviews Chemistry* **2018,** *2* (1), 0105.

5.Dau, H.; Limberg, C.; Reier, T.; Risch, M.; Roggan, S.; Strasser, P., The Mechanism of Water Oxidation: From Electrolysis via Homogeneous to Biological Catalysis. *ChemCatChem* **2010,** *2* (7), 724-761.

6.Mtangi, W.; Kiran, V.; Fontanesi, C.; Naaman, R., Role of the Electron Spin Polarization in Water Splitting. *J Phys Chem Lett* **2015,** *6* (24), 4916-4922.

7.Mtangi, W.; Tassinari, F.; Vankayala, K.; Vargas Jentzsch, A.; Adelizzi, B.; Palmans, A. R. A.; Fontanesi, C.; Meijer, E. W.; Naaman, R., Control of Electrons' Spin Eliminates Hydrogen Peroxide Formation During Water Splitting. *J Am Chem Soc* **2017,** *139* (7), 2794-2798.

8.Zhang, W.; Banerjee-Ghosh, K.; Tassinari, F.; Naaman, R., Enhanced Electrochemical Water Splitting with Chiral Molecule-Coated Fe3O4 Nanoparticles. *ACS Energy Letters* **2018,** *3* (10), 2308-2313.

9.Ghosh, K. B.; Zhang, W.; Tassinari, F.; Mastai, Y.; Lidor-Shalev, O.; Naaman, R.; Möllers, P.; Nürenberg, D.; Zacharias, H.; Wei, J.; Wierzbinski, E.; Waldeck, D. H., Controlling Chemical Selectivity in Electrocatalysis with Chiral CuO-Coated Electrodes. *The Journal of Physical Chemistry C* **2019,** *123* (5), 3024-3031.

10.Ghosh, S.; Bloom, B. P.; Lu, Y.; Lamont, D.; Waldeck, D. H., Increasing the Efficiency of Water Splitting through Spin Polarization Using Cobalt Oxide Thin Film Catalysts. *The Journal of Physical Chemistry C* **2020,** *124* (41), 22610-22618.

11.Naaman, R.; Paltiel, Y.; Waldeck, D. H., Chiral molecules and the electron spin. *Nature Reviews Chemistry* **2019,** *3* (4), 250-260.

12.Göhler, B.; Hamelbeck, V.; Markus, T. Z.; Kettner, M.; Hanne, G. F.; Vager, Z.; Naaman, R.; Zacharias, H., Spin Selectivity in Electron Transmission Through Self-Assembled Monolayers of Double-Stranded DNA. *Science* **2011,** *331* (6019), 894-897.

13.Kettner, M.; Bhowmick, D. K.; Bartsch, M.; Göhler, B.; Zacharias, H., A Silicon-Based Room Temperature Spin Source without Magnetic Layers. *Advanced Materials Interfaces* **2016,** *3* (20), 1600595.

14.Möllers, P. V.; Ulku, S.; Jayarathna, D.; Tassinari, F.; Nürenberg, D.; Naaman, R.; Achim, C.; Zacharias, H., Spin-selective electron transmission through self-assembled monolayers of double-stranded peptide nucleic acid. *Chirality* **2021,** *33* (2), 93-102.

15.Kettner, M.; Göhler, B.; Zacharias, H.; Mishra, D.; Kiran, V.; Naaman, R.; Waldeck, D. H.; Sęk, S.; Pawłowski, J.; Juhaniewicz, J., Spin Filtering in Electron Transport Through Chiral Oligopeptides. *The Journal of Physical Chemistry C* **2015,** *119* (26), 14542-14547.

16.Kettner, M.; Maslyuk, V. V.; Nürenberg, D.; Seibel, J.; Gutierrez, R.; Cuniberti, G.; Ernst, K.-H.; Zacharias, H., Chirality-Dependent Electron Spin Filtering by Molecular Monolayers of Helicenes. *J Phys Chem Lett* **2018,** *9* (8), 2025-2030.

17.Switzer, J. A.; Kothari, H. M.; Poizot, P.; Nakanishi, S.; Bohannan, E. W., Enantiospecific electrodeposition of a chiral catalyst. *Nature* **2003,** *425* (6957), 490-493.

18.Kothari, H. M.; Kulp, E. A.; Boonsalee, S.; Nikiforov, M. P.; Bohannan, E. W.; Poizot, P.; Nakanishi, S.; Switzer, J. A., Enantiospecific Electrodeposition of Chiral CuO Films from Copper(II) Complexes of Tartaric and Amino Acids on Single-Crystal Au(001). *Chem. Mater.* **2004,** *16* (22), 4232-4244.

19.Poizot, P.; Hung, C.-J.; Nikiforov, M. P.; Bohannan, E. W.; Switzer, J. A., An Electrochemical Method for CuO Thin Film Deposition from Aqueous Solution. *Electrochemical and Solid-State Letters* **2003,** *6* (2), C21.

20.Dzyaloshinsky, I., A thermodynamic theory of "weak" ferromagnetism of antiferromagnetics. *Journal of Physics and Chemistry of Solids* **1958,** *4* (4), 241-255.

21.Moriya, T., Anisotropic Superexchange Interaction and Weak Ferromagnetism. *Physical Review* **1960,** *120* (1), 91-98.

22.Widmer, R.; Haug, F.-J.; Ruffieux, P.; Gröning, O.; Bielmann, M.; Gröning, P.; Fasel, R., Surface Chirality of CuO Thin Films. *J. Am. Chem. Soc.* **2006,** *128* (43), 14103-14108.

23.Tahir, D.; Tougaard, S., Electronic and optical properties of Cu, CuO and Cu₂O studied by electron spectroscopy. *Journal of Physics: Condensed Matter* **2012,** *24* (17), 175002.

24.Pauly, N.; Tougaard, S.; Yubero, F., Determination of the Cu 2p primary excitation spectra for Cu, Cu2O and CuO. *Surface Science* **2014,** *620*, 17-22.

25.Gellman, A. J., Chiral Surfaces: Accomplishments and Challenges. *ACS Nano* **2010,** *4* (1), 5-10.

26.Chen, Q.; Richardson, N. V., 9 Physical studies of chiral surfaces. *Annual Reports Section "C" (Physical Chemistry)* **2004,** *100* (0), 313-347.

27.Bohannan, E. W.; Nicic, I. M.; Kothari, H. M.; Switzer, J. A., Enantiospecific electrodeposition of chiral CuO films on Cu(110) from aqueous Cu(II) tartrate and amino acid complexes. *Electrochimica Acta* **2007,** *53* (1), 155-160.

28.Bai, T.; Ai, J.; Liao, L.; Luo, J.; Song, C.; Duan, Y.; Han, L.; Che, S., Chiral Mesostructured NiO Films with Spin Polarisation. *Angewandte Chemie International Edition* **2021,** *60* (17), 9421-9426.

29.Bai, T.; Ai, J.; Duan, Y.; Han, L.; Che, S., Spin Selectivity of Chiral Mesostructured Iron Oxides with Different Magnetisms. *Small* **2022,** *18* (12), 2104509.

30.Ghijsen, J.; Tjeng, L. H.; van Elp, J.; Eskes, H.; Westerink, J.; Sawatzky, G. A.; Czyzyk, M. T., Electronic structure of Cu2O and CuO. *Phys Rev B Condens Matter* **1988,** *38* (16), 11322-11330.

31.Ching, W. Y.; Xu, Y. N.; Wong, K. W., Ground-state and optical properties of Cu2O and CuO crystals. *Physical review. B, Condensed matter* **1989,** *40* (11), 7684-7695.

32.Morasch, J.; Wardenga, H. F.; Jaegermann, W.; Klein, A., Influence of grain boundaries and interfaces on the electronic structure of polycrystalline CuO thin films. *physica status solidi (a)* **2016,** *213* (6), 1615-1624.

33.Benndorf, C.; Caus, H.; Egert, B.; Seidel, H.; Thieme, F., Identification of Cu(I) and Cu(II) oxides by electron spectroscopic methods: AES, ELS and UPS investigations. *Journal of Electron Spectroscopy and Related Phenomena* **1980,** *19* (1), 77-90.

34.Scudiero, L.; Barlow, D. E.; Hipps, K. W., Scanning Tunneling Microscopy, Orbital-Mediated Tunneling Spectroscopy, and Ultraviolet Photoelectron Spectroscopy of Nickel(II) Octaethylporphyrin Deposited from Vapor. *Journal of Physical Chemistry B* **2002,** *106*, 996-1003.

35.Wu, D.; Zhang, Q.; Tao, M., LSDA+U study of cupric oxide: Electronic structure and native point defects. *Phys. Rev. B* **2006,** *73*.

36.Koffyberg, F. P.; Benko, F. A., A photoelectrochemical determination of the position of the conduction and valence band edges of p ‐ type CuO. *Journal of Applied Physics* **1982,** *53* (2), 1173-1177.

37.Seah, M. P.; Dench, W. A., Quantitative electron spectroscopy of surfaces: A standard data base for electron inelastic mean free paths in solids. *Surface and Interface Analysis* **1979,** *1* (1), 2-11.

38.Borstel, G.; Wöhlecke, M., Spin polarization of photoelectrons emitted from nonmagnetic solids. *Physical Review B* **1982,** *26*, 1148-1155.

39.Wöhlecke, M.; Borstel, G., On the Role of Spin-Orbit Coupling and Crystal Symmetry on the Spin-Polarization of Photoelectrons in Nonmagnetic Crystals. *Physica Scripta* **1983,** *T4*, 162-164.

40.Vasilyev, D.; Medjanik, K.; Babenkov, S.; Ellguth, M.; Schoenhense, G.; Elmers, H. J., Relation between spin-orbit induced spin polarization, Fano-effect and circular dichroism in soft X-ray photoemission. *Journal of physics. Condensed matter : an Institute of Physics journal* **2019**.

41.Inui, A.; Aoki, R.; Nishiue, Y.; Shiota, K.; Kousaka, Y.; Shishido, H.; Hirobe, D.; Suda, M.; Ohe, J.-i.; Kishine, J.; Yamamoto, H.; Togawa, Y., Chirality-Induced Spin-Polarized State of a Chiral Crystal $CrNb_3S_6$. *Physical Review Letters* **2020,** *124*.

42.Nabei, Y.; Hirobe, D.; Shimamoto, Y.; Shiota, K.; Inui, A.; Kousaka, Y.; Togawa, Y.; Yamamoto, H. M., Current-induced bulk magnetization of a chiral crystal $CrNb_3S_6$. *Applied Physics Letters* **2020,** *117* (5), 052408.

43.Shiota, K.; Inui, A.; Hosaka, Y.; Amano, R.; Ōnuki, Y.; Hedo, M.; Nakama, T.; Hirobe, D.; Ohe, J.-i.; Kishine, J.-i.; Yamamoto, H. M.; Shishido, H.; Togawa, Y., Chirality-Induced

Spin Polarization over Macroscopic Distances in Chiral Disilicide Crystals. *Physical Review Letters* **2021,** *127* (12), 126602.

44.Gutierrez, R.; Díaz, E.; Gaul, C.; Brumme, T.; Domínguez-Adame, F.; Cuniberti, G., Modeling Spin Transport in Helical Fields: Derivation of an Effective Low-Dimensional Hamiltonian. *The Journal of Physical Chemistry C* **2013,** *117* (43), 22276-22284.

45.Michaeli, K., Origin of Spin-Dependent Tunneling Through Chiral Molecules. *The Journal of Physical Chemistry C* **2015,** *123*.

46.Geyer, M.; Gutierrez, R.; Cuniberti, G., Effective Hamiltonian model for helically constrained quantum systems within adiabatic perturbation theory: Application to the chirality-induced spin selectivity (CISS) effect. *The Journal of Chemical Physics* **2020,** *152* (21), 214105.

47.Liu, Y.; Xiao, J.; Koo, J.; Yan, B., Chirality-driven topological electronic structure of DNA-like materials. *Nature Materials* **2021,** *20* (5), 638-644.

48.Filippetti, A.; Fiorentini, V., Magnetic ordering in CuO from first principles: a cuprate antiferromagnet with fully three-dimensional exchange interactions. *Physical review letters* **2005,** *95 8*, 086405.

49.Yang, B. X.; Thurston, T. R.; Tranquada, J. M.; Shirane, G., Magnetic neutron scattering study of single-crystal cupric oxide. *Physical Review B* **1989,** *39* (7), 4343-4349.

50.Koo, H.-J.; Whangbo, M. H., Magnetic Superstructures of Cupric Oxide CuO as Ordered Arrangements of One-Dimensional Antiferromagnetic Chains. *Inorganic chemistry* **2003,** *42*, 1187-92.

51.Sundaresan, A.; Bhargavi, R.; Rangarajan, N.; Siddesh, U.; Rao, C. N. R., Ferromagnetism as a universal feature of nanoparticles of the otherwise nonmagnetic oxides. *Physical Review B* **2006,** *74* (16), 161306.

52.Rehman, S.; Mumtaz, A.; Hasanain, S. K., Size effects on the magnetic and optical properties of CuO nanoparticles. *Journal of Nanoparticle Research* **2011,** *13* (6), 2497-2507.

53.Punnoose, A.; Magnone, H.; Seehra, M. S.; Bonevich, J., Bulk to nanoscale magnetism and exchange bias in CuO nanoparticles. *Physical Review B* **2001,** *64* (17), 174420.

54.Mishra, S. R.; Losby, J.; Dubenko, I.; Roy, S.; Ali, N.; Marasinghe, K., Magnetic properties of mechanically milled nanosized cupric oxide. *Journal of Magnetism and Magnetic Materials* **2004,** *279* (1), 111-117.

55.Osorio-Guillén, J.; Lany, S.; Barabash, S. V.; Zunger, A., Nonstoichiometry as a source of magnetism in otherwise nonmagnetic oxides: Magnetically interacting cation vacancies and their percolation. *Physical Review B* **2007,** *75* (18), 184421.

56.Hou, X.; Liu, H.; Sun, H.; Liu, L.; Jia, X., Significant room-temperature ferromagnetism in porous ZnO films: The role of oxygen vacancies. *Materials Science and Engineering: B* **2015,** *200*, 22-27.

57.Xie, J.; Cheng, B.; Liu, L.; Liu, W.; Ren, S.; Miao, T.; Gao, C.; Zhou, G.; Qin, H.; Hu, J., The mechanism of photo-regulated magnetization in copper oxide films on Pt substrate. *Solid State Communications* **2019,** *303-304*, 113732.

58.Arbuzova, T. I.; Naumov, S. V.; Arbuzov, V. L.; Druzhkov, A. P., Anomalous magnetic properties of electron-irradiated antiferromagnetic copper monoxide. *Physics of the Solid State* **2009,** *51* (5), 953-960.

59.Dmitrienko, V. E.; Ovchinnikova, E. N.; Collins, S. P.; Nisbet, G.; Beutier, G.; Kvashnin, Y. O.; Mazurenko, V. V.; Lichtenstein, A. I.; Katsnelson, M. I., Measuring the Dzyaloshinskii–Moriya interaction in a weak ferromagnet. *Nature Physics* **2014,** *10* (3), 202-206.

60.Ben Dor, O.; Yochelis, S.; Radko, A.; Vankayala, K.; Capua, E.; Capua, A.; Yang, S.-H.; Baczewski, L. T.; Parkin, S. S. P.; Naaman, R.; Paltiel, Y., Magnetization switching in ferromagnets by adsorbed chiral molecules without current or external magnetic field. *Nature Communications* **2017,** *8* (1), 14567.

61.Meirzada, I.; Sukenik, N.; Haim, G.; Yochelis, S.; Baczewski, L. T.; Paltiel, Y.; Bar-Gill, N., Long-Time-Scale Magnetization Ordering Induced by an Adsorbed Chiral Monolayer on Ferromagnets. *ACS Nano* **2021,** *15* (3), 5574-5579.

62.Naaman, R.; Paltiel, Y.; Waldeck, D. H., Chiral Molecules and the Spin Selectivity Effect. *J. Phys. Chem. Lett.* **2020,** *11* (9), 3660-3666.

5.0 Atomic layer deposition of chiral metal oxide

5.1 Introduction

The findings in Chapters 3 and 4 show that electrodeposition is a fairly reliable method to grow chiral metal oxides; however, the method does have weaknesses. Specifically, the film roughness and overall quality are very difficult to control when making ultrathin CuO films (<10 nm), and it seems to be challenging to improve. While a very rough surface is good for some applications such as electrocatalytic water splitting, other applications such as semiconductor manufacturing would require a smooth surface and a uniform thickness. Therefore, for potential applications that need ultrathin metal oxide films, a different technique is required.

Apart from using chiral ligands to impart chirality into metal oxide films during electrodeposition, Mastai *et al.* has proposed growing chiral metal oxides from achiral sources onto chiral self-assembled monolayers (SAM) as a template, such as cysteine[1-3]. In order to avoid SAM degradation which may occur under electrooxidation conditions, they used atomic layer deposition (ALD) to deposit thin metal oxide films onto a SAM coated electrode. ALD is a sequential chemical vapor deposition method and it involves two precursors to form the final metal oxide. The first precursor is usually an organometallic species and it is very reactive, thus it binds to many different surfaces such as SiO_2 or Au. Also, the first precursor determines what kind of metal oxide will be formed in the end. For example, if tetrakis(dimethylamino) titanium is used as the first precursor, the final metal oxide will be TiO_2. The second precursor is used to remove the organic group attached to the metal and oxidize the metal into its final oxide form. The second

precursor (usually water) is always introduced into the reaction chamber after the first precursor has adhered to the substrate.

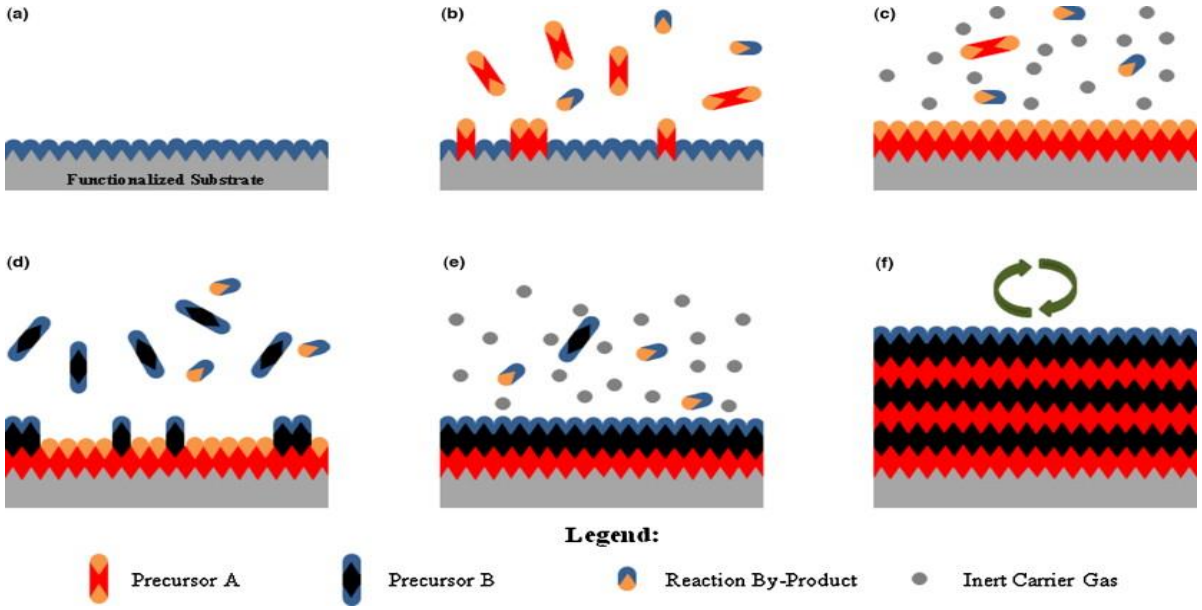

Figure 5-1. Representation of an ALD film growth process: Precursor A is pulsed into the reaction chamber and binds to the substrate, and then Precursor B is introduced to react with precursor A in order to form one layer of metal oxide. This cycle can be repeated many times to reach the desired thickness. Reprinted with permission from ref 4.

Figure 1 shows a typical cycle of ALD: The process starts with the functionalized substrates that allows the ALD precursor reagent to bind to the surface (panel 1a), then precursor A is injected into the reaction chamber and adheres to the substrate (panel 1b). For example, during the ALD of TiO_2 films, most recipes use water as the first precursor, thus it is important for the substrate to be hydrophilic. Once precursor A has finished binding to the substrate surface, the residual precursor A gas is purged from the reaction chamber (panel 1c), leaving only one atomic layer of precursor A on the substrate surface. Then, precursor B is introduced to react with precursor A on the surface (panel 1d)[4], and in the case of TiO_2 deposition, precursor B consists of tetrakis(dimethylamino) titanium which will react with water to form TiO_2. Because there is only one atomic layer of precursor A, only one atomic layer of precursor B will be allowed to react and bind to the substrate. Once the two precursors have finished reacting with each other, the remaining

precursor B will also be purged from the chamber, leaving just one atomic layer of metal oxide (panel 1e). By repeating this cycle from panel 1a to 1e, multiple layers of the metal oxide can be deposited (panel 1f) to increase and control the metal oxide film thickness. However, it should be noted that the ALD cycle is a time-consuming process, so it is inadvisable to make films that are more than 10 nm thick, where other methods such as chemical vapor deposition will be more suitable.

The substrates Mastai *et al.* used are Au films with cysteine (Cys) SAM on the surface, and Cys molecules are hydrophilic enough to allow the water to bind to it. The biggest concern is that the Cys SAM can become unstable at 150^{o}C, while most ALD processes require a high temperature to work. Fortunately, TiO_2 films can be formed at 100^{o}C, so the integrity of the SAM layer can be maintained throughout the process. After the ALD process is finished, the chirality and spin selectivity of these films can be tested with the same methods as mentioned in previous chapters, such as cyclic voltammetry (CV) and circular dichroism (CD) spectroscopy. If the films deposited by using ALD are also chiral, ALD would be a much more efficient way of making thinner and smoother chiral metal oxide films than electrodeposition, because multiple metal oxide films can be made in one ALD process, and the thickness can be easily controlled by limiting the number of ALD cycles.

5.2 Experimental

The substrates for SAM assembly consist of 5 nm of Ti and 100 nm of Au on top of microscope glass slides, and the metal films were made using the AJA UHV hybrid sputtering and e-beam evaporation system. The cysteine SAM was made by immersing the Au film substrates in

1 mM of L-cysteine (≥ 98%, Sigma Aldrich) or D-cysteine (≥ 99%, Sigma Aldrich) solution dissolved in ethanol (200 proof, Fisher) for 24 hours. The substrates were then taken out of the solution and dried with argon.

The TiO_2 films were deposited on top of the Cys SAM by thermal ALD using the Cambridge Nanotech Fiji ALD System at Carnegie Mellon University, and the deposition temperatures was 100^{o}C. The recipe used for TiO_2 deposition has a rate of 0.3 Å/cycle. The spectroscopic ellipsometry of the TiO_2 films was conducted using a Jobin Yvon Unisel Ellipsometer with an incidence angle of 45^{o}. The data fitting was performed using the DeltaPsi software.

The cyclic voltammetry was collected using a CH Instruments 750c potentiostat. The working electrodes are the L-Cys or D-Cys TiO_2 films, the reference electrode is an Ag/AgCl electrode in 3M KCl, and the counter electrode is a Pt mesh. The tartrate redox reactions were preformed in 5mM of L- or D-tartrate (Sigma Aldrich) dissolved in 0.1M NaOH (Fisher) solution, and the chiral ferrocene experiments were done in 0.8mM of (R)-(+)- or (S)-(-)-N,N-Dimethyl-1-ferrocenylethylamine (Sigma Aldrich) in pH = 7 phosphate buffer solution.

The circular dichroism (CD) spectra were collected using an Olis 17 circular dichroism spectrophotometer. The TiO_2 films for CD measurements were prepared in the same way as mentioned above, but the underlying Au substrate was changed to 3 nm of Ti and 10 nm of Au on fused silica slides. These small thicknesses were used to make sure that the substrates are transparent enough for the CD measurements.

5.3 Results and Discussion

Mastai *et al.* have published several works about depositing metal oxide on chiral SAMs using ALD, and different techniques were used to confirm the chirality of the metal oxide films. However, we discovered that some of the data in these reports may require further review and optimization. Figure 2 is a reprint of the second-harmonic generation-circular dichroism (SHG-CD) results from Mastai et al[1]. In the original literature, the authors mentioned that SHG-CD of two materials that possess opposite chirality should look like mirror images, similar to a conventional CD spectrum, and the top two panels of Figure 2 show that L-Cys and D-Cys SAM have opposite SHG intensity for different polarizations of the light (quarter wave rotation angle). However, the chiral SAM/TiO_2 films obtained by ALD, lose much of the mirror symmetry quality in the SHG intensity. While the authors do comment on the different SHG intensity of Cys SAM and TiO_2 covered Cys SAM, more explanation about why the SHG intensity of L-Cys/TiO_2 and D-Cys/TiO_2 lose their mirror image symmetry can help the readers to understand the data better.

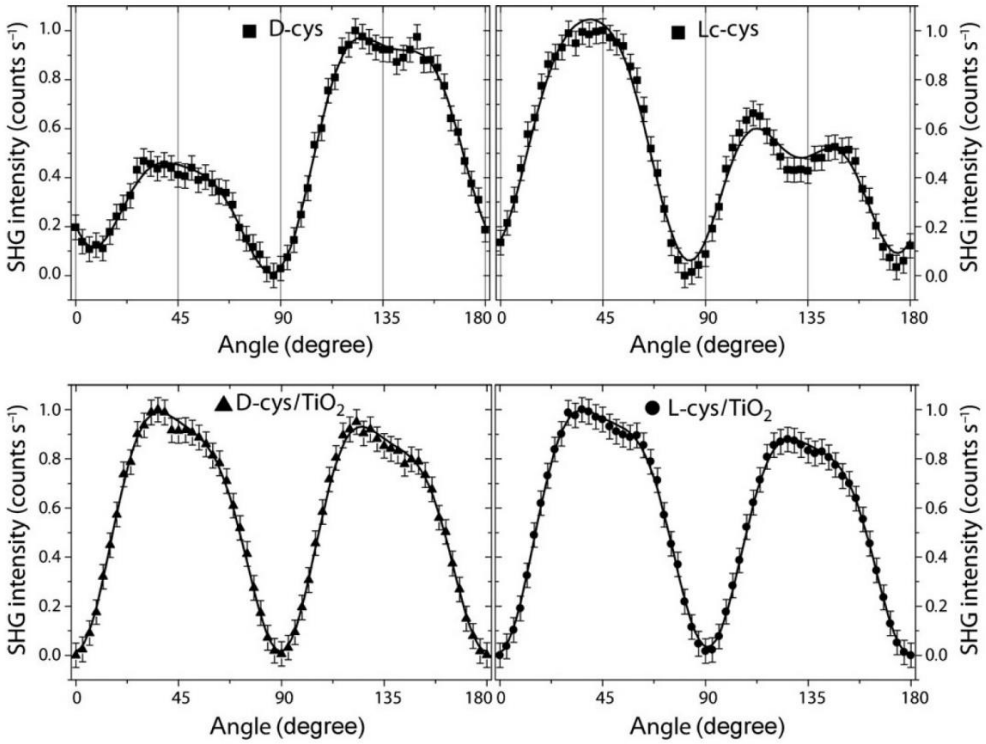

Figure 5-2. SHG intensity versus quarter wave plate rotation angle. Top: D and L-cysteine on gold; bottom: D- and L-cysteine on gold covered with TiO_2. Reprinted from ref 1.

In addition, Mastai *et al.* used a quartz crystal microbalance to test if TiO_2 films show any chiral bias towards L- and D-valine. Specifically, the authors proposed that if the TiO_2 films are chiral, one might expect that the L-Cys/TiO_2 film to display enantiospecificity during the adsorption of valine and that the D-Cys/TiO_2 might display an opposite enantiospecificity. Figure 3 shows a reprint of the valine absorption/desorption results from Mastai et al.[1]. While the data

show that the L-Cys/TiO_2 film adsorbs more valine than the D-Cys/TiO_2, the enantiospecificity in the films for the L- and D-valine is very small.

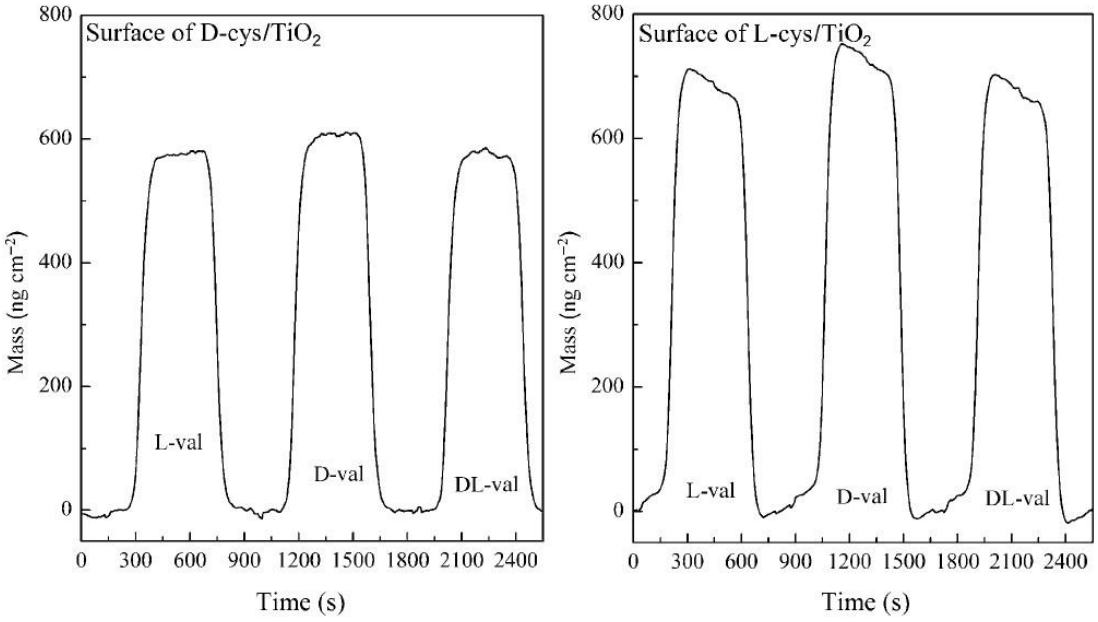

Figure 5-3. Quartz microbalance (QCM) adsorption/desorption profile of L- and D-valine onto TiO_2 L- and D-cysteine nanofilms. Reprinted from ref 1.

The idea of using chiral SAM to imprint chirality into the metal oxide films could prove very useful if it could be shown to be viable. Given the electrooxidation studies shown in Chapters 2 and 3, adding a chiral precursor to incorporate chirality into a metal oxide has been proven to be viable. Thus, we developed a series of experiments to follow up on Mastai's work to examine the chirality of ALD deposited metal oxides further.

Before testing the chirality of the TiO_2 films, we used spectroscopic ellipsometry and cyclic voltammetry to confirm that TiO_2 was present on the Cys SAM after the ALD cycles. Figure 4a shows the fitted ellipsometric data of a TiO_2 film. The collected Ψ and Δ angles of TiO_2 was fitted to the reference TiO_2 data in the software, and the best fit gives a thickness of 1.23 nm, which indicates the presence of TiO_2 (more detail of ellipsometry can be found in the appendix). Furthermore, the same TiO_2 film was used as a working electrode to collect cyclic voltammograms in a 0.1 M K_2SO_4 solution (Figure 4b), and the extremely low current levels found in the

voltammetry confirms that there is an insulating layer on the Au substrate, which is what one would expect from a TiO_2 film.

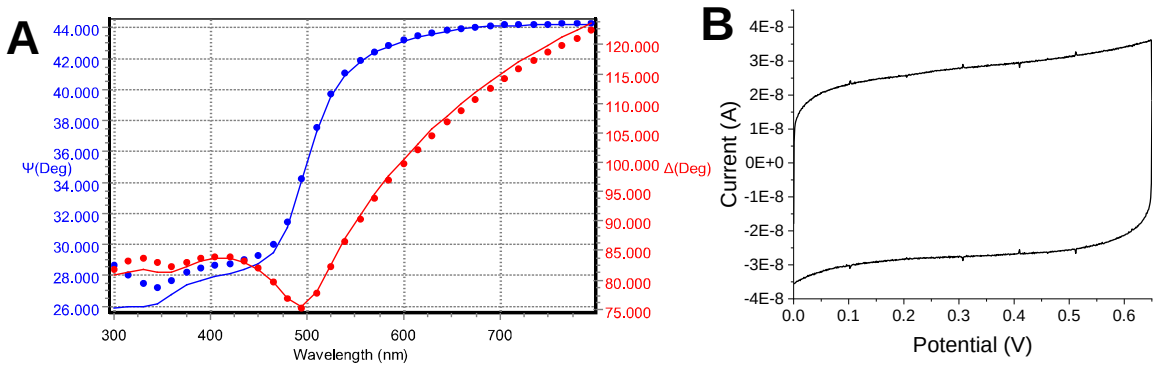

Figure 5-4. (A) Ellipsometry of a TiO_2 film deposited using ALD on an Au substrate with L-Cys SAM. (B) Cyclic voltammogram of 0.1M K_2SO_4 solution with a TiO_2 film as the working electrode. The reference electrode is an Ag/AgCl electrode immersed in 1M KCl, and the counter electrode is a Pt mesh.

In order to test whether the metal oxide films from ALD are chiral, the electrochemical method used by Switzer et al. was used. Specifically, the metal oxide films were used as working electrodes in a cyclic voltammetry experiment with chiral molecules that are redox active, with the expectation that chiral metal oxide films will show an enantiospecificity. The expectation that the response is enantioselective can be seen from earlier studies[5, 6] where a chiral metal oxide would selectively oxidize one of the two enantiomers with higher peak currents. If the TiO_2 films are indeed chiral, then we expect that the L-enantiomorph will select for the L-enantiomer of the redox couple and the D-enantiomorph will select for the D-enantiomer.

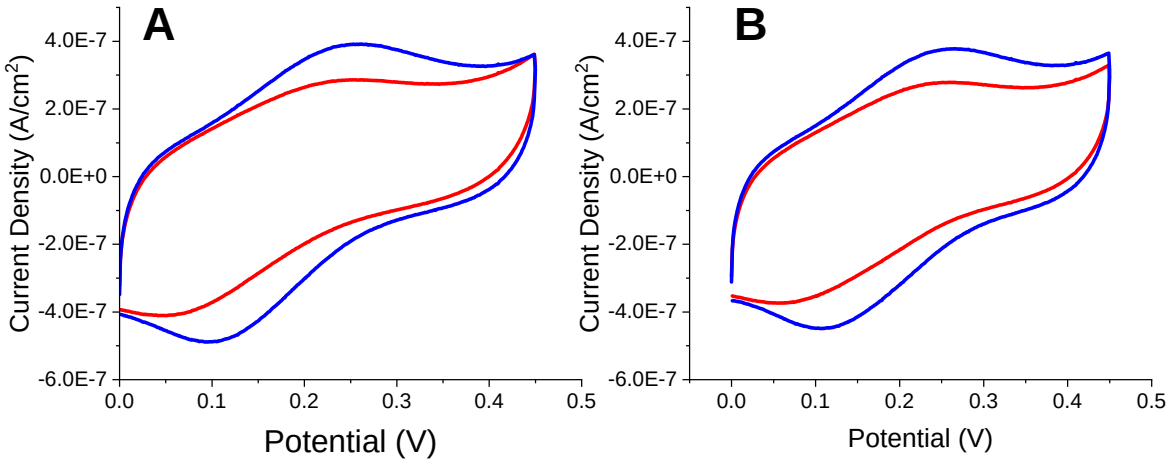

Figure 5-5. Cyclic voltammograms of L-tartrate (red) and D-tartrate (blue) in 0.1M Na_2SO_4 on 1.5 nm thick TiO_2 electrodes. (A) Working electrode consists of TiO_2 deposited on L-Cys SAM using ALD. (B) Working electrode consists of TiO_2 deposited on D-Cys SAM using ALD.

Figure 5 shows the voltammograms of 5mM L-tartrate and D-tartrate solution in 0.1M K_2SO_4 as the supporting electrolyte, and the working electrodes are ~1.5 nm thick TiO_2 films deposited on an L-Cys and D-Cys SAM. While both L- and D-tartrate ions show a semi-reversible behavior, both panel A and panel B show that the D-tartrate have more positive peaks potential and higher current densities than those of the L-tartrate. Thus, the TiO_2 films shows no chiral selectivity during the tartrate redox reaction. Also, we tried to collect the tartrate voltammograms under higher pH by using 0.1M NaOH as the supporting electrolyte (Figure 6). Similarly, the D-tartrate voltammograms in Figure 6 have higher current densities than those of the L-tartrate, and both the L-Cys SAM/TiO_2 and D-Cys SAM TiO_2 again behave in the same way; namely, the TiO_2

films with L-Cys and D-Cys SAM underneath do not selectively oxidize one of the two tartrate enantiomers.

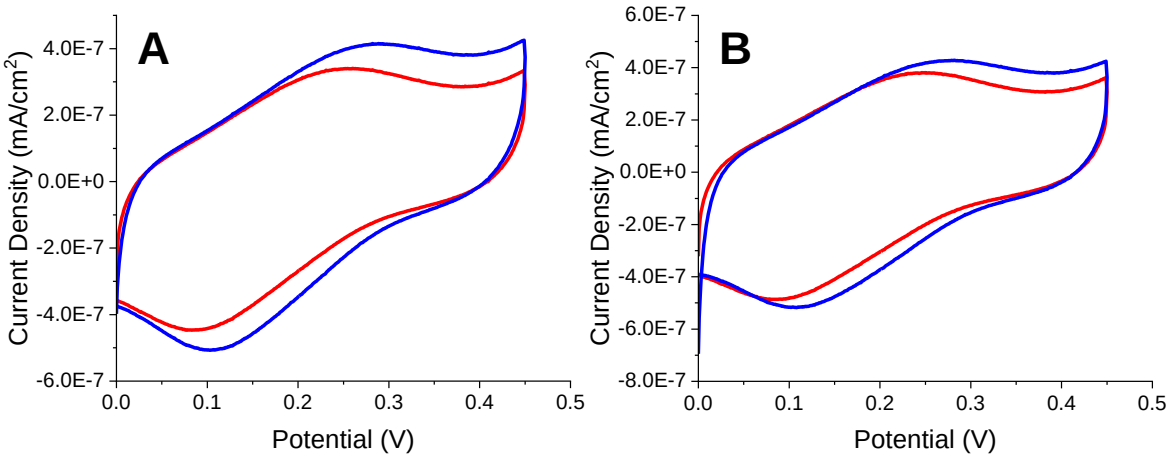

Figure 5-6. CV of L-tartrate (red) and D-tartrate (blue) in 0.1M NaOH on 1.5nm thick TiO_2 electrodes. (A) Working electrode consists of TiO_2 deposited on L-Cys SAM using ALD. (B) Working electrode consists of TiO_2 deposited on D-Cys SAM using ALD.

In addition, we examined the redox couples (R)-(+)-N,N-Dimethyl-1-ferrocenylethylamine and (S)-(-)-N,N-Dimethyl-1-ferrocenylethylamine (R-Fc and S-Fc) which were used in previous literature as chiral redox species[3] that can differentiate the chirality of the TiO_2 films. Figure 7 shows the voltammograms of R-Fc and S-Fc collected using the same TiO_2 covered working electrodes, similar to the tartrate experiments. The R-Fc always has a higher peak

current density than the S-Fc even though the chirality of the Cys SAM underneath the TiO_2 was different.

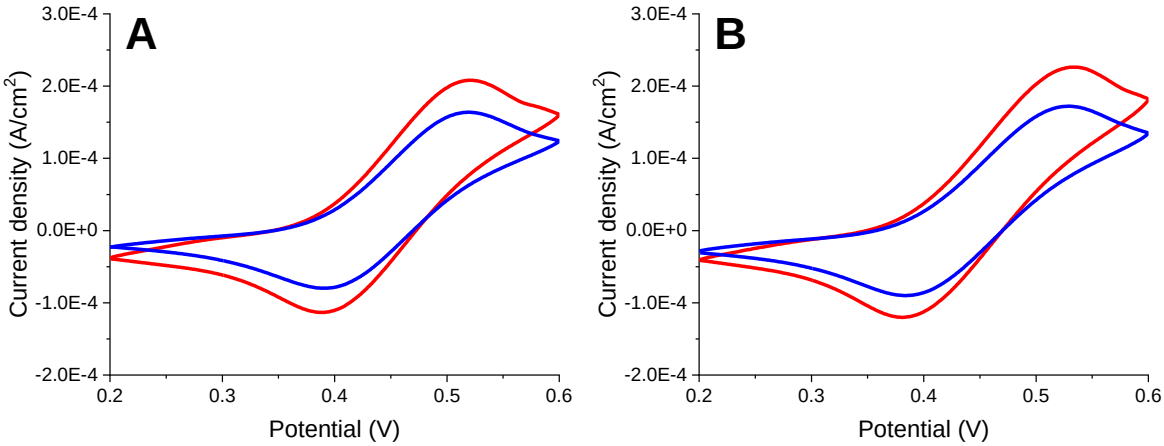

Figure 5-7. CV of 400µM R-Fc (red) and S-Fc (blue) in 10mM Na_2SO_4 on 1.5nm thick TiO_2 electrodes. (A) Working electrode consists of TiO_2 deposited on L-Cys SAM using ALD. (B) Working electrode consists of TiO_2 deposited on D-Cys SAM using ALD.

Despite the fact that there is no chiral bias is present in Figures 5 to 7, the method of using tartrate oxidation to identify the chirality of a metal oxide was demonstrated for chiral CuO films (see Figure 8), which were electrodeposited using tartaric acid, so it is possible that there is a lack of affinity between the TiO_2 films and the chiral molecules we have tested. Furthermore, Figure 9A shows the voltammetry of R-Fc and S-Fc on a bare Au film electrode, and the higher current density of R-Fc can also be seen even though the working electrode is achiral; thus it was discovered that the higher current density of the R-Fc was either inherent to the molecule itself, or

the Au substrate could also have an inherent chirality. Further investigation is needed to identify the real cause.

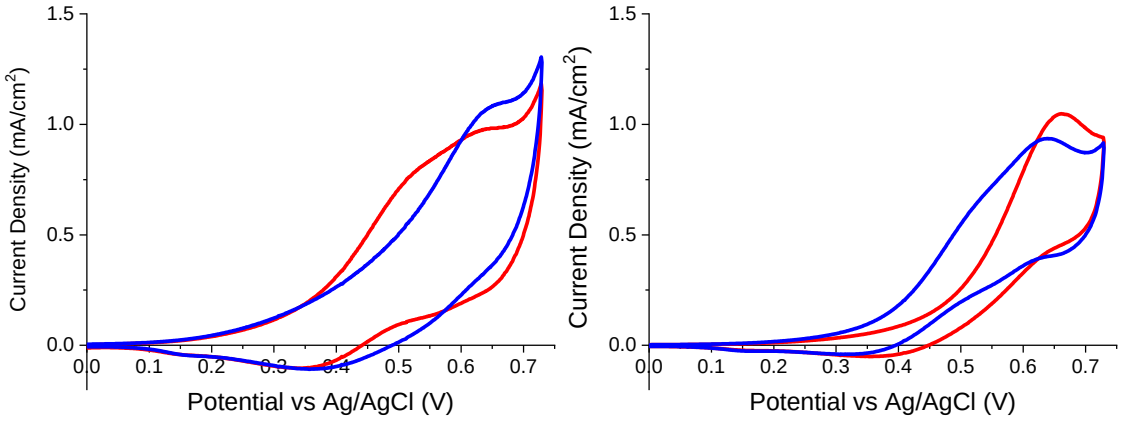

Figure 5-8. CV of L-tartrate (red) and D-tartrate (blue) in 0.1M NaOH on 100nm thick CuO electrodes. (A) Working electrode consists of CuO deposited using L-tartaric acid. (B) Working electrode consists of CuO deposited using D-tartaric acid.

Despite the negative results using electrochemical methods, it is still possible that the TiO_2 is just simply not stable enough under aqueous conditions, and the chirality of the film is difficult to detect using voltammetry. Thus, CD spectra were collected for the TiO_2 films. Figure 9B shows CD spectra of 3nm of TiO_2 films deposited on L- and D-Cys SAM using ALD, and unlike the CD spectra of CuO in previous chapters, the CD spectra of thin TiO_2 films show no noticeable peak. While it is possible that the TiO_2 films are too thin to be detected with CD, ALD is not designed to deposit metal oxide films that are more than 10nm thick, thus making thicker films for CD experiments is not viable.

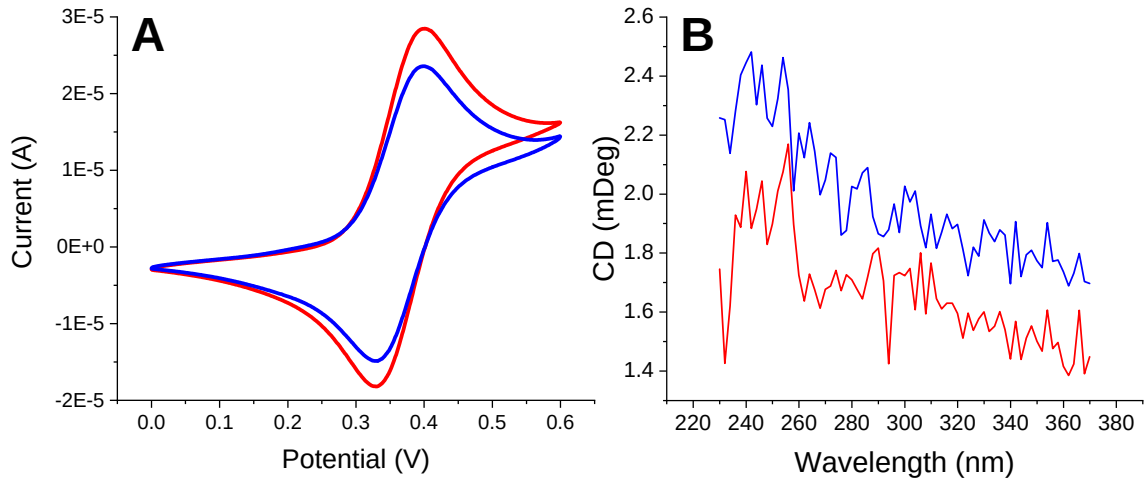

Figure 5-9. (A) CV of 400µM R-Fc (red) and S-Fc (blue) in 10mM Na_2SO_4 on a bare Au film electrode. (B) Circular dichroism spectra of L-Cys TiO_2 film (red) and D-Cys TiO_2 (blue) on a 3nm Ti and 10nm Au film on fused silica substrates. Both the L- and D-TiO_2 are 3nm thick.

5.4 Conclusion

The deposition of TiO_2 thin film on Cys SAM using ALD was successful, but neither cyclic voltammetry nor CD show any indication that the TiO_2 layer is chiral. In order to elucidate the chirality of thin metal oxide films, a SAM made with longer and more stable molecules could serve as the next step, because the longer molecule could imprint chirality into the metal oxide more readily, and the increased stability should enable a higher temperature for the ALD cycles and the resulting metal oxide should also become more stable.

5.5 Reference

1.Moshe, H.; Vanbel, M.; Valev, V. K.; Verbiest, T.; Dressler, D.; Mastai, Y., Chiral Thin Films of Metal Oxide. *Chemistry – A European Journal* **2013,** *19* (31), 10295-10301.

2.Moshe, H.; Levi, G.; Sharon, D.; Mastai, Y., Atomic layer deposition of enantioselective thin film of alumina on chiral self-assembled-monolayer. *Surface Science* **2014,** *629*, 88-93.

3.Mathew, S. P.; Mondal, P. C.; Moshe, H.; Mastai, Y.; Naaman, R., Non-magnetic organic/inorganic spin injector at room temperature. *Appl. Phys. Lett.* **2014,** *105* (24), 242408.

4.Johnson, R. W.; Hultqvist, A.; Bent, S. F., A brief review of atomic layer deposition: from fundamentals to applications. *Mater. Today* **2014,** *17* (5), 236-246.

5.Kothari, H. M.; Kulp, E. A.; Boonsalee, S.; Nikiforov, M. P.; Bohannan, E. W.; Poizot, P.; Nakanishi, S.; Switzer, J. A., Enantiospecific Electrodeposition of Chiral CuO Films from Copper(II) Complexes of Tartaric and Amino Acids on Single-Crystal Au(001). *Chemistry of Materials* **2004,** *16*, 4232-4244.

6.Bohannan, E. W.; Nicic, I. M.; Kothari, H. M.; Switzer, J. A., Enantiospecific electrodeposition of chiral CuO films on Cu(110) from aqueous Cu(II) tartrate and amino acid complexes. *Electrochimica Acta* **2007,** *53* (1), 155-160.

6.0 Conclusion

The focus of our research was to show how the CISS effect works and using different approaches to demonstrate the CISS effect. In Chapter 2, we have shown how the CISS effect can be used to explain why spin polarization exists in biological systems and how they could affect the electron transfer process. Specifically, the spin polarized electrons selectively transmit through molecules with one chirality over the other, and this could serve as an alternative explanation for the homochirality of all biological systems on earth.

The other approach we have studied is to develop methods to make chiral metal oxide films. In Chapters 3 and 4, we have used CD spectroscopy and photoemission spectroscopy to show the chirality of the CuO films that are electrodeposited using either L- and D-tartaric acid, and we have shown how these chiral CuO films could be used to enhance the efficiency of water splitting by prohibiting the formatting of singlet state oxygen and lower the overpotential of the reaction. Chapter 5 describes a different method of making chiral metal oxide, which is using ALD to deposit thin metal oxide on a chiral SAM. It is possible for the SAM to imprint its own chirality into the metal oxide, however it seems that he chiral imprint in these cases are very weak. Thus, further studies are necessary, and the tripeptide used in Chapter 2 could be a better choice as a SAM compared to Cys SAM.

7.0 Appendix

7.1 Spectroscopic ellipsometry

Ellipsometry is a technique that can be used to measure the thickness and optical properties of thin films. The basic principles of ellipsometry are shown in Figure 1[1], where light reflects off the surface of a material at a certain angle of incidence, and the polarization state of the reflected and transmitted light are affected by the properties of the film.

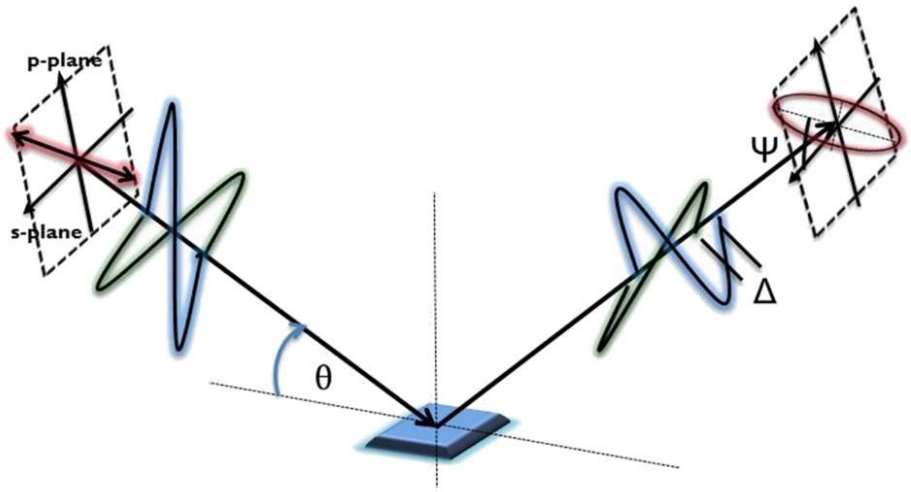

Figure 7-1. The ellipsometry measurement is shown. Here, light polarized at 45◦ from the plane of incidence is shown scattering from a sample. The angle θ that the light makes with surface is shown in the main figure. Adapted from ref 1.

The two most important properties that are collected with an ellipsometer are Δ and Ψ. Δ is the phase difference between the incident light and the reflected light and it can be any value between 0^o and 360^o; Ψ is the arctangent of wave magnitudes of the incoming wave and the outgoing wave, and the value of Ψ is between 0^o and 90^o. Δ and Ψ together are used to define the

complex reflectance ratio (ρ) in Equation 1[2], where R^p and R^s are the reflectance of polarized waves that are in the plane of incidence (p-wave) and perpendicular to the plane of incidence (s-wave).

$$\rho = \tan\Psi e^{i\Delta} = \frac{R^p}{R^s} \quad (1)$$

Assuming a single interface model, the theoretical values of R^p and R^s can be calculated using Equation 2[2], which are known as the Fresnel equations. $\widetilde{N}_1$ and $\widetilde{N}_2$ are the complex refractive indices of the two materials, ϕ_1 and ϕ_2 are the angles of incidence and diffraction respectively. All the values in Equation 2 are also illustrated in Figure 2[2].

$$R^p = \left|\frac{\widetilde{N}_2\cos\phi_1 - \widetilde{N}_1\cos\phi_2}{\widetilde{N}_2\cos\phi_1 + \widetilde{N}_1\cos\phi_2}\right|^2 \qquad R^s = \left|\frac{\widetilde{N}_1\cos\phi_1 - \widetilde{N}_2\cos\phi_2}{\widetilde{N}_1\cos\phi_1 + \widetilde{N}_2\cos\phi_2}\right|^2 \quad (2)$$

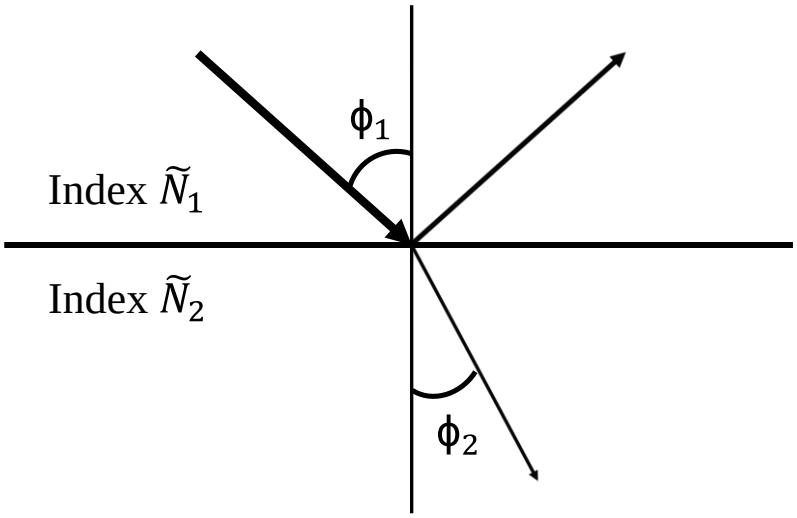

Figure 7-2. Illustration of reflection and transmission at a single interface. Adapted from ref 2.

The theoretical values of R^p and R^s can be used to calculate the theoretical values of Δ and Ψ. Moreover, spectroscopic ellipsometers have the ability to collect Δ and Ψ at different wavelengths (hence the name spectroscopic ellipsometry) and fit them to a model to calculate the thickness of a thin film. In order to do this, some optical parameter of the thin film material must

be known, such as the refractive index (n), wavelength of the incident light (λ) and angle of incidence (ϕ). The theoretical thickness (d) can be calculated using Equation 3[3].

$$d = \frac{\lambda}{2\sqrt{n_2^2 - \sin^2 \phi_2}} \quad (3)$$

By fitting the experimental and theoretical values of Δ and Ψ, the thickness of the thin films can be estimated. The ellipsometry technique was used to measure the thickness of TiO_2 and Al_2O_3 films in Chapter 5.

7.2 Reference

1.Diebold, A. C.; Antonelli, A.; Keller, N., Perspective: Optical measurement of feature dimensions and shapes by scatterometry. *APL Materials* **2018,** *6* (5), 058201.

2.Tompkins, H. G., Chapter 1 - Theoretical Aspects. In *A User's Guide to Ellipsometry*, Tompkins, H. G., Ed. Academic Press: San Diego, 1993; pp 1-18.

3.Tompkins, H. G., Chapter 3 - Using Optical Parameters to Determine Material Properties. In *A User's Guide to Ellipsometry*, Tompkins, H. G., Ed. Academic Press: San Diego, 1993; pp 35-50.